AFRL-RV-PS-
TR-2022-0026

AFRL-RV-PS-
TR-2022-0026

THREE-DIMENSIONAL MODELING OF NUCLEAR EXPLOSIONS USING A MICRO-MECHANICAL DAMAGE MODEL

Jeffry L. Stevens, et al.

Leidos
10260 Campus Point Drive
San Diego, CA 92121

15 June 2021

Final Report

APPROVED FOR PUBLIC RELEASE; DISTRIBUTION IS UNLIMITED.

AIR FORCE RESEARCH LABORATORY
Space Vehicles Directorate
3550 Aberdeen Ave SE
AIR FORCE MATERIEL COMMAND
KIRTLAND AIR FORCE BASE, NM 87117-5776

DTIC COPY

NOTICE AND SIGNATURE PAGE

Using Government drawings, specifications, or other data included in this document for any purpose other than Government procurement does not in any way obligate the U.S. Government. The fact that the Government formulated or supplied the drawings, specifications, or other data does not license the holder or any other person or corporation; or convey any rights or permission to manufacture, use, or sell any patented invention that may relate to them.

This report was cleared for public release by AFMC/PA and is available to the general public, including foreign nationals. Copies may be obtained from the Defense Technical Information Center (DTIC) (http://www.dtic.mil).

AFRL-RV-PS-TR-2022-0026 HAS BEEN REVIEWED AND IS APPROVED FOR PUBLICATION IN ACCORDANCE WITH ASSIGNED DISTRIBUTION STATEMENT.

//SIGNED//	//SIGNED//
_____	_____
2d Lt Simone M. Smith	For: Erin N. Pettyjohn, Chief
Program Manager/AFRL/RVB	AFRL Geospace Technologies Division

This report is published in the interest of scientific and technical information exchange, and its publication does not constitute the Government's approval or disapproval of its ideas or findings.

REPORT DOCUMENTATION PAGE

Form Approved
OMB No. 0704-0188

Public reporting burden for this collection of information is estimated to average 1 hour per response, including the time for reviewing instructions, searching existing data sources, gathering and maintaining the data needed, and completing and reviewing this collection of information. Send comments regarding this burden estimate or any other aspect of this collection of information, including suggestions for reducing this burden to Department of Defense, Washington Headquarters Services, Directorate for Information Operations and Reports (0704-0188), 1215 Jefferson Davis Highway, Suite 1204, Arlington, VA 22202-4302. Respondents should be aware that notwithstanding any other provision of law, no person shall be subject to any penalty for failing to comply with a collection of information if it does not display a currently valid OMB control number. **PLEASE DO NOT RETURN YOUR FORM TO THE ABOVE ADDRESS.**

1. REPORT DATE *(DD-MM-YYYY)*	**2. REPORT TYPE**	**3. DATES COVERED** *(From - To)*
15-06-2021	Final Report	26 Apr 2019 – 15 Jun 2021

4. TITLE AND SUBTITLE
Three-dimensional Modeling of Nuclear Explosions Using a Micro-mechanical Damage Model

5a. CONTRACT NUMBER
FA9453-19-C-0059

5b. GRANT NUMBER

5c. PROGRAM ELEMENT NUMBER
C6601F

6. AUTHOR(S)
Jeffry L. Stevens, Charles G. Sammis, and Michael O'Brien

5d. PROJECT NUMBER
1010

5e. TASK NUMBER
EF133209

5f. WORK UNIT NUMBER
V1BG

7. PERFORMING ORGANIZATION NAME(S) AND ADDRESS(ES)
Leidos
10260 Campus Point Drive
San Diego, CA 92121

8. PERFORMING ORGANIZATION REPORT NUMBER
AFRL/RVBN

9. SPONSORING / MONITORING AGENCY NAME(S) AND ADDRESS(ES)
Air Force Research Laboratory
Space Vehicles Directorate
3550 Aberdeen Avenue SE
Kirtland AFB, NM 87117-5776

10. SPONSOR/MONITOR'S ACRONYM(S)

11. SPONSOR/MONITOR'S REPORT NUMBER(S)
AFRL-RV-PS-TR-2022-0026

12. DISTRIBUTION / AVAILABILITY STATEMENT
Approved for public release; distribution is unlimited (AFMC-2022-1075 dtd 04 Mar 2022).

13. SUPPLEMENTARY NOTES

14. ABSTRACT
We have implemented the latest version of the micro-mechanical damage model developed by Dr. Charles Sammis and associates in a Fortran 90 module that can be incorporated into a 1D, 2D or 3D code. We have added the module to our 1D spherically symmetric nonlinear finite difference code SKIPPER and our 3D finite element code CRAM3D. We performed an extensive set of calculations using the 1D code, and compared the results with near-field data from US and former Soviet Union underground nuclear explosions. The new model gives a better data fit to the Degelen data than the quasistatic damage model used in Stevens et al (2003), and also gives a fairly good data fit to the Piledriver data without changing any parameters. The results of the calculations were used to define the physical models and parameters used in the 3D code. We performed a large number of three-dimensional nonlinear calculations of explosions with the micromechanical damage model in regions with flat surfaces and with strong topography. We find that the initial P-wave is insensitive to micromechanical damage, but the later part of the P-wave and SV and SH waves can be affected substantially by damage, particularly in the presence of topography. Surface waves are affected by damage in complex ways, particularly in regions of topography. In brief, micromechanical damage in a flat topography reduces surface waves while micromechanical damage in a region with topography may either enhance or reduce surface waves depending on the location of the explosion relative to the surface.

15. SUBJECT TERMS
micromechanical damage model, nonlinear finite element and finite difference calculations, nuclear explosion monitoring

16. SECURITY CLASSIFICATION OF:			**17. LIMITATION OF ABSTRACT**	**18. NUMBER OF PAGES**	**19a. NAME OF RESPONSIBLE PERSON**
a. REPORT	**b. ABSTRACT**	**c. THIS PAGE**			2d Lt Simone M. Smith
Unclassified	Unclassified	Unclassified	Unlimited	96	**19b. TELEPHONE NUMBER** *(include area code)*

This page is intentionally left blank.

Approved for public release; distribution is unlimited.

Table of Contents

Section **Page**

1. SUMMARY **1**

2. INTRODUCTION **2**

3. TECHNICAL APPROACH **3**

3.1 THE MICROMECHANICAL DAMAGE MODEL 3
3.1.1 Development of the Constitutive Model *5*
3.1.2 Evaluation of the Stress Intensity Factors *5*
3.1.3 Constitutive Relationship and Damage Evolution *6*
3.2 IMPLEMENTATION IN SKIPPER AND CRAM3D 8
3.2.1 Equation of State *8*
3.2.2 Shear Strength *9*
3.2.3 Tensile cracking *9*
3.2.4 Shear strength reduction *9*
3.2.5 Shear modulus reduction *10*
3.2.6 Options and Order of Application *10*

4. RESULTS AND DISCUSSION **11**

4.1 COMPARISON OF SPHERICALLY SYMMETRIC GRANITE RUNS WITH AND WITHOUT THE SAMMIS MICROMECHANICAL DAMAGE MODEL 11
4.1.1 Micromechanical Test Cases *11*
4.1.2 Comparison with Shoal *15*
4.1.3 Calculated Damage *21*
4.2 COMPARISON WITH DEGELEN MOUNTAIN NEAR-FIELD DATA 24
4.3 COMPARISON WITH PILEDRIVER DATA 28
4.4 CONCLUSIONS FROM ONE-DIMENSIONAL ANALYSIS 29

5. RESULTS FROM 3D CALCULATIONS **30**

5.1 COMPARISON OF 1D AND 3D RESULTS FOR NINE MATERIAL MODELS 30
5.2 SELECTION OF OPTIMUM MATERIAL MODEL 35
5.3 THE EFFECT OF MICROCRACK SIZE 40
5.4 BODY AND SURFACE WAVES USING THE MICROMECHANICAL DAMAGE MODEL 42
5.4.1 Body and Surface Waves from Shoal *42*
5.4.2 Body and Surface Waves from Degelen Mountain *45*
5.4.3 Body and Surface Waves from the Slope Calculations *49*
5.5 THE EFFECT OF MICROMECHANICAL DAMAGE ON BODY AND SURFACE WAVES 58

REFERENCES **59**

APPENDIX A. MICROMECHANICAL CONSTITUTIVE EQUATIONS **61**

APPENDIX B. DIAGNOSTIC DATA FROM THE 1D SHOAL CALCULATIONS List of Figures **66**

B.1 COMPARISON OF K1R, CRACK GROWTH, DAMAGE AND STRESS/STRAIN AT 99M FOR CASE9 WITH A=1MM TO 1M. 67
B.2 RDP AND RVP FOR CASE 9 76
B.3 DAMAGE VS. LOCATION AND TIME FOR CASE 9 77
B.4 CALCULATED MATERIAL PROPERTIES 83

LIST OF SYMBOLS, ABBREVIATIONS, AND ACRONYMS **85**

List of Figures

Figure **Page**

Figure 1. Geometry in the micromechanical damage mechanics model. 3

Figure 2. CRAM3D and SKIPPER Computational Cycle..... 8

Figure 3. Failure surface in principal deviatoric stress space for τ=1. S1, S2 and S3 are the principal deviatoric stresses 9

Figure 4. Granite strength model. 9

Figure 5. Location of the Shoal explosion and the three nearfield shot level recording stations and the direction of the local stress state..... 15

Figure 6. Left: radial velocity and displacement recorded at the three stations. Right: calculation at zero and 90 degrees. 15

Figure 7. Comparison of SKIPPER calculations of Shoal at 590 meters (red) with recorded data (blue). 16

Figure 8. Calculated (red) and observed (blue) waveforms from the 62 kt explosion Piledriver using the SA-SS model 17

Figure 9. Calculated (red) and observed (blue) waveforms from the 78 kt 1987/07/17 Degelen Mountain explosion using the SA-SS model 16

Figure 10. Case 7 with a=1 cm 18

Figure 11. Calculated velocity waveforms (red) compared with Shoal data (blue) for case 9. Top row a=1mm, middle row a=10cm, bottom row a=1m 18

Figure 12. From top to bottom cases 1,2,3,4,5,6,7,8,9, velocity waveforms. 19

Figure 13. Final damage for case #8. Top left: a=1mm, top right a=1cm, bottom left a=10cm, bottom right a=1m. 21

Figure 14. Final damage for case #9. Top left: a=1mm, top right a=1cm, bottom left a=10cm, bottom right a=1m.. 22

Figure 15. Final damage for all cases, a=10 cm. Top: case 1 (left), case 2 (right); row 2: case 3 (left), case 4 (right), row 3: case 5 (left), case 6 (right), row 4: case 7 (left), case 8 (right); bottom: case 9. 22

Figure 16. Shot level data from Degelen Mountain explosions compared to Shoal calculation #9 with a=10cm. 24

List of Figures (continued)

Figure **Page**

Figure 17. Comparison Piledriver near-field data with Calculation #9 and a=10cm..... 28

Figure 18. Comparison of 1D and 3D waveforms at a distance of 100m from the source for each set of material models used in the 1D study described earlier, with *a*=10cm. Case number is in the title. 30

Figure 19. Radial (outward from source center) waveforms at 5 locations..... 32

Figure 20. Waveforms in two directions at 590 meters from the source, out to 0.2 seconds, for cases 7, 8 and 9.. 34

Figure 21. Cavity shape at the end of the calculation for the nine material models 35

Figure 22. Surface velocity and displacement for case 9..... 37

Figure 23. Evolution of microdamage (left) and microdamage regime (right) for case 9..... 38

Figure 24. Damage region from Shoal calculation with 1mm microcracks. 40

Figure 25. Damage region from Shoal calculation with 1cm microcracks..... 40

Figure 26. Damage region from Shoal calculation with 10cm microcracks..... 41

Figure 27. Damage region from Shoal calculation with 1m microcracks..... 41

Figure 28. Far-field P-waves low-pass filtered at 5 Hz from four calculations with different microcrack sizes. Left: without tectonic release; right: with tectonic release..... 42

Figure 29. Far-field SV-waves low-pass filtered at 5 Hz from four calculations with different microcrack sizes. Left: without tectonic release; right: with tectonic release..... 42

Figure 30. Long period surface waves low-pass filtered at 0.1 Hz from four calculations with different microcrack sizes. Left: without tectonic release; right: with tectonic release..... 43

Figure 31. Ms as a function of initial crack size, with and without compressive tectonic release, compared to Shoal.. 43

Figure 32. Surface waves with and without compressive tectonic release for 1m microcracks... 44

Figure 33. Left: Calculation #8, 78 kt explosion with topography. Right: calculation with microdamage added. Top: final cavity shape; middle: plastic work; bottom: microdamage fraction 45

List of Figures (continued)

Figure **Page**

Figure 34. Left: Calculation #8, 78 kt explosion with topography. Right: calculation with microdamage added. Top: P, SV and SH waves at zero degrees (direction of the negative X axis). Bottom: vertical, radial and tangential surface wave components 46

Figure 35. Left: Calculation #8, 78 kt explosion with topography and tectonic stresses. Right: calculation with tectonic stresses and with microdamage added. Top: P, SV and SH waves at zero degrees (direction of the negative X axis). Bottom: vertical, radial and tangential surface wave components 47

Figure 36. Surface wave spectral amplitudes at zero degrees. Top: topography, no tectonic stresses. Bottom, with compressive tectonic stresses. Left: without micromechanical damage model; Right: with micromechanical damage model 48

Figure 37. Elevation in map view and cross section for the slope calculation. 49

Figure 38. Damaged regions for the Slope1 calculations. 49

Figure 39. Damaged regions for the Slope2 calculations 50

Figure 40. Plastic work (left) and tensile crack strains (right) for the Slope1 calculations. Top: no microdamage; Second: 1 mm, Third: 1 cm, Fourth: 10 cm; lower right: 1 m, Bottom: 10 cm 50

Figure 41. Plastic work (left) and tensile crack strains (right) for the Slope2 calculations. Top: no microdamage; Second: 1 mm, Third: 1 cm, Fourth: 10 cm; lower right: 1 m, Bottom: 10 cm 51

Figure 42. Body waves at three different azimuths for the Slope1 calculations. Top: no microdamage; Second: 1 mm, Third: 1 cm, Fourth: 10 cm; lower right: 1 m, Bottom: 10 cm 52

Figure 43. Body waves at three different azimuths for the Slope2 calculations. Top: no microdamage; Second: 1 mm, Third: 1 cm, Fourth: 10 cm; lower right: 1 m, Bottom: 10 cm 53

Figure 44. Surface waves at 2000 km distance for three different azimuths for the Slope1 calculations. Top: no microdamage; Second: 1 mm, Third: 1 cm, Fourth: 10 cm; lower right: 1 m, Bottom: 10 cm 54

Figure 45. Surface waves at 2000 km distance for three different azimuths for the Slope2 calculations. Top: no microdamage; Second: 1 mm, Third: 1 cm, Fourth: 10 cm; lower right: 1 m, Bottom: 10 cm 55

Figure 46. Surface wave amplitudes for Slope1, Slope2 and Shoal as a function of initial crack size. 57

List of Tables

Table **Page**

Table 1. Properties of granite used in SKIPPER calculations. Numbers below are in SI and CGS units. CGS units are used in SKIPPER, SI in CRAM3D 11

Table 2. Sammis model properties for granite 11

Table 3. Nonlinear options used in test runs 12

Table 4. Calculated final cavity radii (meters) 13

Table 5. Calculated reduced displacement potential (m^3) 13

Table 6. Radius of plastic yielding (m) 13

Table 7. Radius of full damage (m) 14

Table 8. Radius of partial damage (m) 14

Table 9. Minimum P velocity 14

Table 10. Slope and Shoal calculations 49

This page is intentionally left blank.

1. SUMMARY

We have implemented the latest version of the micro-mechanical damage model developed by Dr. Charles Sammis and associates in a Fortran 90 module that can be incorporated into a 1D, 2D or 3D code. We have added the module to our 1D spherically symmetric nonlinear finite difference code SKIPPER and our 3D finite element code CRAM3D. We performed an extensive set of calculations using the 1D code, and compared the results with near-field data from US and former Soviet Union underground nuclear explosions. The new model gives a better data fit to the Degelen data than the quasistatic damage model used in Stevens et al (2003), and also gives a fairly good data fit to the Piledriver data without changing any parameters. The results of the calculations were used to define the physical models and parameters used in the 3D code. We performed a large number of three-dimensional nonlinear calculations of explosions with the micromechanical damage model in regions with flat surfaces and with strong topography. We find that the initial P-wave is insensitive to micromechanical damage, but the later part of the P-wave and SV and SH waves can be affected substantially by damage, particularly in the presence of topography. Surface waves are affected by damage in complex ways, particularly in regions of topography. In brief, micromechanical damage in a flat topography reduces surface waves while micromechanical damage in a region with topography may either enhance or reduce surface waves depending on the location of the explosion relative to the surface.

Approved for public release; distribution is unlimited.

2. INTRODUCTION

For many years, we have modeled seismic waves from underground nuclear explosions using numerical calculations in one, two and three dimensions. Under AFRL support, we developed CRAM3D, a finite element code specifically designed for calculating underground nuclear explosions. CRAM3D genearally uses a continuum model for material strength and damage. For the past two decades, Dr. Charles Sammis and associates at USC have been developing a micromechanical damage model, also developed under AFRL support, which explicitly takes into account damage due to microcracks and failure due to crack coalescence (Ashby and Sammis (1990); Deshpande and Evans (2008); Bhat, Rosakis, and Sammis (2012); Thomas et al, (2017)). We previously implemented an early version of this model in our one-dimensional spherically symmetric code SKIPPER (Rimer et al, 1998,1999; Stevens et al, 2002, 2003). Here we implement the latest version of the micromechanical damage model first in SKIPPER and then in CRAM3D, and use it to model the damage caused by the explosion and the effect of this damage on seismic waves.

In the following sections of the report, we:

1. Describe the current version of the micromechanical damage model and the equations that are incorporated into the numerical codes
2. Describe the other nonlinear mechanisms that are included in our codes and how they interact with the micromechanical damage model
3. Give the results of an extensive set of spherically symmetric calculations; compare the results of the calculations to near-field data from the former Nevada Test Site, Fallon, Nevada and Degelen Mountain in the former Soviet Union.
4. Describe how the micromechanical damage model is incorporated into the SKIPPER and CRAM3D codes.
5. Perform 3D calculations with the micromechanical damage model for Shoal and Degelen Mountain.
6. Calculate seismic waves from the 3D calculations.
7. Analyze differences in seismic waves with the micromechanical damage model included.

3. TECHNICAL APPROACH

3.1 The micromechanical damage model

We use the micromechanical damage mechanics originally formulated by Ashby and Sammis (1990) for compressive loading and generalized by Deshpande and Evans (2008) to also allow tensile stress states. As illustrated in Figure 1, frictional sliding on optimally oriented initial flaws nucleates tensile wing-cracks, which, at high stress, coalesce to pulverize the rock. If the initial fracture distribution is isotropic then there will always be optimally oriented starter flaws at any azimuth and the resultant damage pattern will have spherical symmetry.

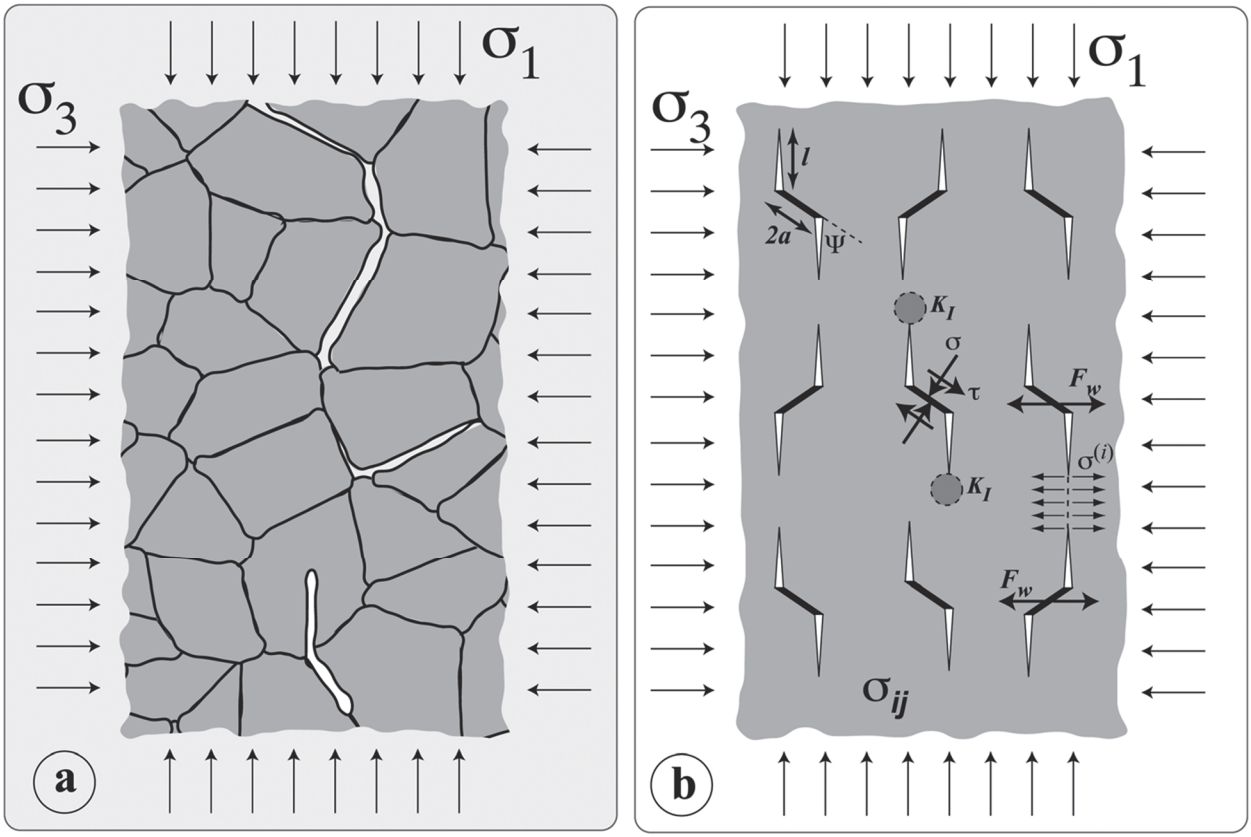

Figure 1. Geometry in the micromechanical damage mechanics model. Sliding on an array of penny-shaped cracks having volume density of N_V and radius a produces a wedging force F_w that drives tensile wing cracks to open in the direction of the smallest principal stress σ_3 and propagate parallel to the largest principal stress σ_1. Growth of wing cracks is enhanced by σ_1, retarded by σ_3, and enhanced by a global interaction that produces a mean tensile stress $\boldsymbol{\sigma}^{i}$. The positive feedback provided by this tensile interaction stress leads to a run-away growth of the wing cracks and ultimate macroscopic failure.

The micromechanical damage mechanics formulated by Ashby and Sammis (1990) models the nucleation, growth, and interaction of a mono-sized distribution of cracks having a fixed orientation. Bhat et al. (2012) used this model as a template to develop their dynamic damage model, which we use in this study. The main features/assumptions of the Ashby/Sammis formulation were:

(1) The starter cracks all have the same radius *a* and are all oriented at the same angle Ψ relative to the axis of principal compression σ_1. If the orientation of σ_1 changes with time so does the

populations of activated cracks. There are N_V such optimally oriented starter flaws per unit volume for any orientation of σ_1. Sliding on the starter cracks is inhibited by Coulomb friction characterized by coefficient *f*.

(2) All additional crack damage is in the form of tensile "wing cracks" that nucleate at the tips of the starter flaws and grow parallel to the σ_1 axis. They open in the direction of the least compressive principal stress σ_3.

(3) The stress at which the wing cracks nucleate is taken from results in the literature and may be expressed as

$$\sigma_{1c} = \left(\frac{\sqrt{1+f^2}+f}{\sqrt{1+f^2}-f}\right)\sigma_3 - \left(\frac{\sqrt{3}}{\sqrt{1+f^2}-f}\right)\frac{K_{IC}}{\sqrt{\pi a}} \quad (1)$$

where K_{IC} is the critical stress intensity factor (fracture toughness), which is a material property.

(4) The stress intensity factor K_I at the tips of the growing wing cracks (of length *l*) is approximated as that at the tip of a tensile crack of radius $l + \alpha a$ that is loaded by a point force at its center. The point force is taken as the σ_3 component of force generated by frictional sliding on the starter flaw. The geometrical factor α is the projection of the starter flaw on the σ_1 axis. This approximation was tested against the numerical solution and found to be poor for small *l* but asymptotically better as *l* increases. An adjustable parameter β was introduced to improve the fit of the approximate K_I to the numerical calculations of K_I at small values of *l*.

(5) The failure stress $\sigma_1^*(\sigma_3)$ is defined as the maximum value of the σ_1 versus *l* curve at constant σ_3.

There are thus four crack related parameters in the model:

(1) $\alpha = cos\Psi$ where Ψ is the angle between an optimally oriented starter crack and the σ_1 axis.

(2) β adjusted to make the approximate expression for K_I agree with the full numerical simulation when the wing cracks are short.

(3) *a* = radius of the starter flaws. It is found by fitting the nucleation equation above to the observed onset of nonlinearity in the stress strain curve or the onset of acoustic emissions.

(4) N_V = number of favorably oriented (active) starter flaws per unit volume. It is found by fitting the uniaxial strength.

Despite these apparently crude approximations, Ashby and Sammis (1990) found that this approximate model gave a very good fit to the failure surfaces, $\sigma_1^*(\sigma_3)$, of a wide range of rocks for reasonable values of *a* (approximately the grain size) and N_V. It was later shown by Bhat et al. (2012) that the inclusion of a size distribution of cracks and allowance for multiple crack orientations did not significantly effect the failure strength predicted by the model.

By approximating the interaction between growing wing cracks Ashby and Sammis (1990) found a positive feedback that led to mechanical instability and failure. They demonstrated that their model gave an adequate description of the failure envelope (σ_1 versus σ_3 at failure) for a wide range of rocks loaded in triaxial compression ($\sigma_1 < \sigma_2 = \sigma_3$, where compression is taken as negative). However since quasi-static crack growth was assumed (the stress intensity factor was always at its critical value) their formulation does not include effects of loading rate. Bhat et al.

(2012) extended the damage mechanics formulation by incorporating theoretical and experimental dynamic crack growth laws that have been shown to be valid over a wide range of loading rates. They compared their model with uniaxial experiments in marble and were able to predict failure stress over a wide range of loading rates ($\dot{\varepsilon}\sim10^{-6}$ to 10^{3} sec^{-1}).

3.1.1 Development of the Constitutive Model

In most brittle materials, micro-crack nucleation, growth and coalescence is driven by local sliding at micro-cracks or grain boundaries as shown schematically in Fig.1. This micro-crack physics produces inelastic dilatancy, modulus reduction, and strain-rate sensitivity of failure strength. Thus any realistic constitutive model of brittle materials should take into account the micromechanics of fracture.

Continuum Constitutive Model From Micro-Scale Deformations

Bhat et al. [2012] used an energy-based approach to determine the constitutive relationship of the damaged solid. If S denotes the current damaged state of the material in the sense that variations in stress at constant S induce a purely elastic response, then the stress-strain relationship and the compliance tensor can be written in terms of a Gibbs free energy function, W, under isothermal conditions as:

$$\varepsilon_{ij} = \frac{\partial W(\boldsymbol{\sigma}, S)}{\partial \sigma_{ij}}$$

$$M_{ijkl} = \frac{\partial^2 [W(\boldsymbol{\sigma},S)]}{\partial \sigma_{ij} \partial \sigma_{kl}} \tag{2}$$

where W is symmetrized in the components of $\boldsymbol{\sigma}$ (notations in bold represent tensor quantities).

Let dW denote the change in the free energy function when the solid undergoes deformation that takes it from the state S to $S + dS$ at constant σ_{ij}. Therefore, the inelastic strain associated with dW is given by

$$d\varepsilon_{ij} = \frac{\partial (dW)}{\partial \sigma_{ij}} \tag{3}$$

The Gibbs free energy is written as the sum of the elastic contribution and an inelastic one due to the presence of micro-cracks, which is written in terms of the stress intensity factors K_I, K_{II}, K_{III}, where subscripts I, II, and III denote the three modes of loading at the crack tip.

$$W(\sigma, S) = W^e(\sigma) + \frac{1-\nu^2}{E} \int_\Gamma \left[K_I^2(\sigma, S) + K_{II}^2(\sigma, S) + \frac{K_{III}^2(\sigma,S)}{(1-\nu)} \right] ds \, d\Gamma \tag{4}$$

In this expression W^e is the elastic strain energy, Γ is the locus of all crack fronts in the damaged solid, and ds is a function of position along Γ describing the amount of local advance of the micro-cracks. The stress-strain relation and the compliance tensor are then given by Eq. 2.

3.1.2 Evaluation of the Stress Intensity Factors

The framework described above was used to evaluate the Gibbs free energy, Eq. 4, and hence the stress-strain relationship and the compliance tensor, for the micro-crack model formulated by

Ashby and Sammis [1990]. As discussed above, this model considers an isotropic elastic solid that contains an array of penny shaped cracks all of radius a (micro-cracks or grain boundaries) all aligned at an angle Ψ to the largest (most negative) remote compressive stress σ_1 (Fig. 1b). Only those cracks that are optimally oriented for sliding are considered. The population of optimal cracks that exist prior to loading has the volume density Nv, which remains fixed during loading - no new sliding cracks appear during loading. The size and density of these initial flaws are characterized by an initial damage defined through the scalar variable

$$D_0 = \frac{4}{3}\pi N_V(\alpha a)^3 \tag{5}$$

where αa is the projection of the crack radius in a vertical plane parallel to the direction of σ_1, $\alpha = cos\Psi$. As the wing cracks extend a distance l in the x_1 direction (see Fig. 1) the damage increases as

$$D = \frac{4}{3}\pi N_V(l + \alpha a)^3 \tag{6}$$

The stress intensity factors are found by calculating the shear and normal stresses on each sliding crack from the remote compressive stress field. Three deformation regimes for the microcracked solid were identified based on the remote loading state. In *Regime I*, the remote loading is compressive and is not large enough to overcome the frictional resistance on the sliding cracks. The solid thus behaves like an isotropic linear elastic solid. In *Regime II* the frictional resistance on the sliding cracks is overcome by the remote compressive load leading to the nucleation and growth of wing-cracks. In *Regime III* the remote loading stress in the x_3 direction turns tensile leading to the opening of both the angled sliding cracks and their wing-crack extensions.

Once the wing cracks nucleate, the Mode-I stress intensity factor, K_I, at the tip of the wing-cracks (of length l) is evaluated. It has three contributions: (1) Sliding on the angle cracks leads to a wedging force, F_w, on the wing-cracks. This wedging force is simply the component of the sliding force resolved in the direction of the minimum principal stress σ_3. (2) The remote confining stress, characterized by σ_3 tends to close the wing-cracks and, (3) opening of the wing cracks creates tension $\sigma^{(i)}$ on the unbroken ligaments between neighboring wing-cracks (see Fig. 1), which is represented as an average global interaction between the wing cracks that enhances their growth.

3.1.3 Constitutive Relationship and Damage Evolution

The Gibbs free energy function in Regimes I, II, and III was evaluated using the stress intensity factors calculated as indicated in the previous section and Eq. 4. The Gibbs free energy function was then differenced as shown in Eq. 2 to obtain the stress-strain relationship and the compliance and modulus tensors. The equations derived using this technique are given in Appendix A.

To complete the constitutive model described above, we need an evolution law for the scalar damage parameter, D. Differentiating D in Eq. 6 with respect to time gives

$$\frac{dD}{dt} = \left(\frac{3D^{2/3}D_0^{1/3}}{\alpha a}\right)\frac{dl}{dt} \tag{7}$$

where $dl/dt = v$ is the instantaneous wing-crack tip speed. This is a geometric relation connecting the wing crack tip speed with the evolution of the damage parameter D. Completing this process requires additional physics relating dl/dt to local stress conditions in the vicinity of the micro-

cracks. This is done by making the stress intensity factor and its critical value (toughness) loading-rate dependent for both the nucleation and growth of the wing cracks.

To solve this problem, we need the state of stress around a crack-tip (both stationary and propagating) under various loading conditions. These values then need to be compared with experimentally determined fracture toughness of the material, under similar conditions, to develop crack initiation and growth criteria. The most common form for such criteria is the requirement that the crack must grow in such a way that some parameter (e.g. the dynamic stress intensity factor, K_I^d) defined as part of the crack-tip field maintains a value that is specific to the material. This value, representing the resistance of the material to the advance of the crack, is called the dynamic fracture toughness (K_{IC}^d) of the material, and it can be determined through experimental measurements only. It can be represented with the following functional form

$$K_{IC}^d = K_{IC}^{SS}\left\{\frac{1+(v/v_m)^5}{\sqrt{1-v/c_p}}\right\} \tag{8}$$

where v_m is the experimentally determined branching speed.

The dynamic stress intensity factor for the growing crack is given by

$$K_I^d(v) = \frac{K_I(1-v/c_R)}{\sqrt{1-v/c_p}} \tag{9}$$

where K_I is the quasi-static stress intensity factor of an equivalent crack of the same length but growing at zero speed. The limiting speed of a mode I crack is thus the Rayleigh speed at which point $K_I^d(c_R) = 0$.

Setting the dynamic stress intensity factor (Eq. 8) equal to the dynamic fracture toughness (Eq. 9) gives the following non-linear equation for the crack speed:

$$\frac{K_I(1-v/c_R)}{\sqrt{1-v/c_p}} = K_{IC}^{SS}\left\{\frac{1+(v/v_m)^5}{\sqrt{1-v/c_p}}\right\} \tag{10}$$

This expression is solved to obtain the crack speed, which is then used in Eq. 7 to complete the damage evolution equation.

The material property that depends on the loading rate is called the Dynamic Initiation Toughness, K_{IC}^D, and its quasi-static limit is K_{IC}^{SS}. This can be represented as $K_{IC}^D = f\left(\dot{K}_1\right)K_{IC}^{SS}$. Bhat et al. (2012) found empirically that:

$$f\left(K_1\right) = 1+\left(\frac{\dot{K}_1}{K_{IC}^{SS}}\right)\left(2x10^{-5}\right) \tag{11}$$

Substituting K_{IC}^D for K_1 in equation 10 gives an equation for the crack tip velocity that can be solved numerically:

$$\frac{1+\left(v/v_m\right)^5}{1-v/c_R} = 1+\left(\frac{\dot{K}_1}{K_{IC}^{SS}}\right)\left(2x10^{-5}\right) \tag{12}$$

3.2 Implementation in SKIPPER and CRAM3D

Rimer et al (1998) implemented an early version of the micromechanical damage model in SKIPPER, the one-dimensional spherically symmetric code. Although implementation in CRAM3D is somewhat more complicated, the procedure is essentially the same. Figure 2 shows a description of a single computational cycle. At the start of each time step, we calculate the accelerations from nodal forces, and update velocities, displacement, strains and strain rates. From this, we calculate new "trial" stresses and stress rates. "Trial" means that the stresses may be adjusted according to nonlinear constitutive models. If the strength of the material is exceeded, then the stresses are reduced according to a plastic flow rule. If a tensile crack opens, then the tensile stress is reduced to zero.

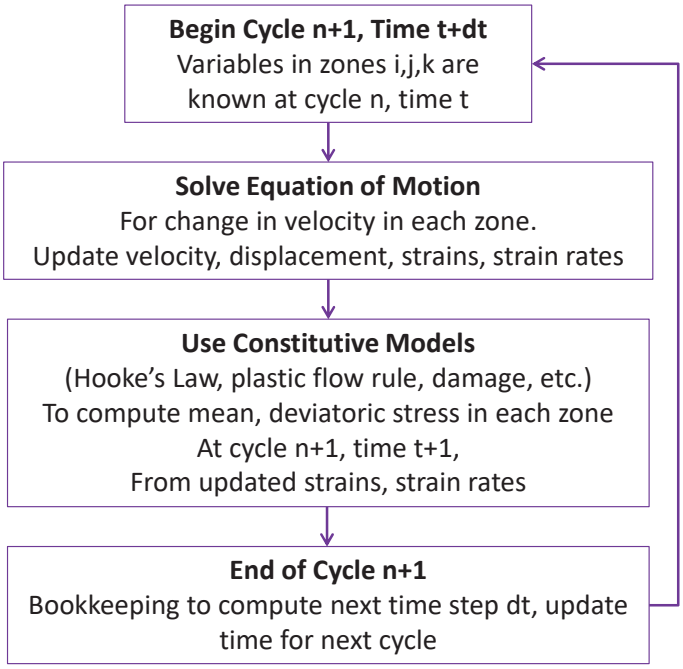

Figure 2. CRAM3D and SKIPPER Computational Cycle

The micromechanical damage model is another type of constitutive model, and it is updated at each time step after the deformation from the previous cycle is calculated. At each time step, and in each element, the code checks to see if the stress state allows cracks to extend, as discussed in the previous section. If it does, then we calculate the speed of crack extension and increase the crack length by the corresponding amount over a time step. If damage increases beyond a critical level failure occurs and we enter a post-failure constitutive model. In the quasistatic model used in the 1998-2003 studies, the code checked to see if an increase in shear stress caused a decrease in crack length, in which case unstable failure occurred. With the new dynamic model, the material does not necessarily fail immediately at the quasistatic failure point because the speed of crack growth is limited by an empirical maximum speed. We use D=1 as the failure condition. The main difference between the 1D and 3D implementations is that in 3D the principal stress directions change and need to be recalculated at each time step, while in 1D the principal stress directions always correspond to the radial and axial directions.

The following sections describe the other components of the numerical calculation.

3.2.1 Equation of State

The equation of state is specified by empirical constants for pressure vs. volume, plus an optional crush curve for porous media. The equation of state is defined by the equation $P = K\mu + B\mu^2$ where P is pressure, K and B define the bulk modulus and μ is the volumetric change defined by $\mu = \rho / \rho_0 - 1$ where ρ and ρ_0 are the current and initial densities, respectively. Granite has a very small porosity and so does not require a crush curve.

3.2.2 Shear Strength

Shear strength is defined by a failure (plastic yielding) condition expressed as a function of deviatoric stress invariants. In its simplest form, shear strength can be stated as a function of shear stress vs. pressure, with the strength increasing with increasing confining pressure. However, the material surrounding the explosion goes through some complicated strain states, initially compressed radially and stretched axially, so a more general relation is needed. We use the formulation developed by Peyton (1983). The failure surface is defined by (Figure 3):

$$\frac{J_2}{\tau^2} - \beta \frac{J_3}{\tau^3} > 1 \qquad (13)$$

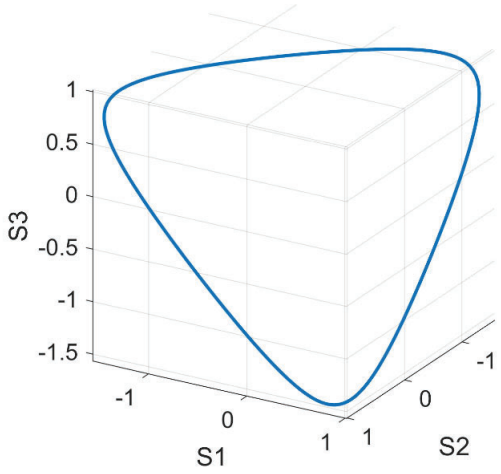

Figure 3. Failure surface in principal deviatoric stress space for τ=1. S1, S2 and S3 are the principal deviatoric stresses.

where J_2 is the second deviatoric stress invariant and J_3 is the third deviatoric stress invariant. τ is defined by an input curve as a function of pressure. β is a shape factor equal to 0.875, and we also require $J_2 < 3\tau^2$. τ is specified as a quadratic function of the form,

$$\tau = \tau_0 + \tau_m \frac{P}{P_m}\left(2 - \frac{P}{P_m}\right), \qquad (14)$$

where $\tau = \tau_0 + \tau_m$ for $P > P_m$.

3.2.3 Tensile cracking

Tensile cracking is based on the formulation of Maenchen and Sack (1964), and can be a very important effect. When the normal stress in any direction becomes tensile, the material strength in that direction is set to zero. Tensile cracks can heal after compression is reapplied. Tensile cracking is turned on in the granite model. Tensile cracking typically occurs soon after failure from the micromechanical damage model.

3.2.4 Shear strength reduction

Several input parameters are required to define the strength reduction model. The first, *cramepw*, is the amount of plastic work accumulated before strength weakening begins. For the Shoal granite model it is 500 Joules/m^3 (5000 erg/cm^3).

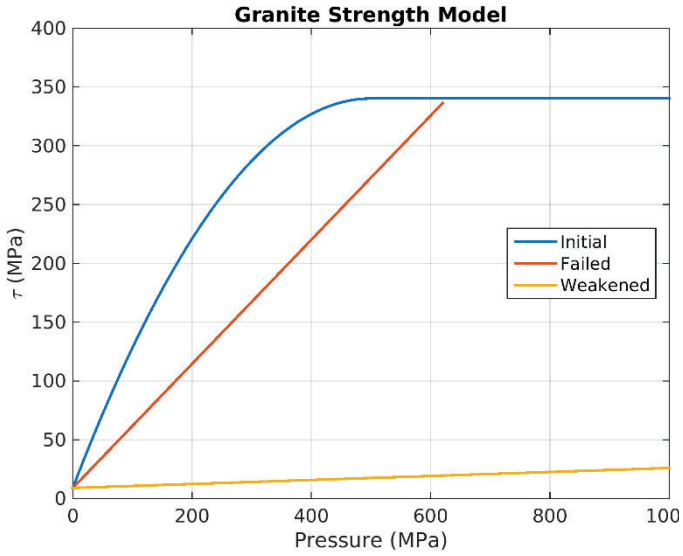

Figure 4. Granite strength model. "Initial" line is the initial granite strength, "Failed" is the strength immediately after failure, "Weakened" is the final shear strength.

The amount of strength reduction is determined by the shear strain, with limits *deinit*=0.001 and *defull*=0.06. The strength is weakened linearly between these values from the "Failed" strength to the "Weakened" strength. The "Failed" and "Weakened" lines can be thought of as corresponding to static and dynamic friction, which in this case have coefficients of friction of 0.6 and 0.02 (equivalent $\tau =$ 0.528 and 0.017), respectively. The minimum failed strength is defined by a cohesive strength *taucoh*, which was set equal to the zero pressure strength of the rock τ_0. The strength states for this model are shown in Figure 4.

3.2.5 Shear modulus reduction

The shear modulus decreases as a function of shear strain, from *epinit* to *epfull*, from its initial value to its reduced value *Gdam*. For the Shoal granite model *epinit*=4×10^{-4}, *epfull*=$1.0 * 10^{-3}$, and *Gdam*=1.0×10^{10} Pa (10×10^{10} dyne/cm^2).

3.2.6 Options and Order of Application

The nonlinear codes SKIPPER and CRAM3D allow for any or all of these constitutive models to be used, but there is a prescribed order to how they are used, as follows:

1. The elastic calculation is done first, generating the trial stresses.
2. The micromechanical damage model is done next, taking the material from its elastic state through unstable crack growth.
3. Shear failure is calculated next, causing at least a small amount of plastic flow to occur before other nonlinear effects are allowed. The amount of shear failure is measured by the plastic work accumulated. There is an option to allow shear failure before failure from the micromechanical damage model. This gives better results near the cavity where stresses are very high and brittle failure is unlikely.
4. Tensile cracking can occur once plastic work is nonzero.
5. Shear modulus reduction can occur once the maximum shear strain in an element has exceeded epinit.
6. Strength reduction can occur once plastic work exceeds cramepw and the maximum shear strain exceeds deinit.

4. 1-D RESULTS AND DISCUSSION

4.1 Comparison of Spherically Symmetric Granite Runs with and without the Sammis Micromechanical Damage Model

We have implemented the Sammis Micromechanical Damage Model in our 1D spherically symmetric nonlinear finite difference code SKIPPER. We compare the results with the strain damage model that has been used for calculations of Shoal, North Korea and other explosions (Stevens and Thompson, 2015). These calculations were all done with the parameters used for Shoal, a 12.5 kt explosion in granite at a depth of 367.4 m. In the following, we start with properties common to all calculations (Table 1), then discuss the nonlinear effects modeled in the original granite Shoal calculation, and then including the Sammis model with a range of variants on modeling parameters.

Table 1. Properties of granite used in SKIPPER calculations. Numbers below are in SI and CGS units. CGS units are used in SKIPPER, SI in CRAM3D

Property	Value (SI)	Value (CGS)	Variable Name
Bulk modulus	37.9×10^9 Pa	379×10^9 dyne/cm^2	K/aks/capa
Shear modulus	23.8×10^9 Pa	238×10^9 dyne/cm^2	G/amu
Density	2600 kg/m^3	2.6 g/cm^3	rho
Melt energy	5.2×10^9 J/m^3	5.2×10^{10} erg/cm^3	em/emlt
τ_0 - Strength at P=0	8.96×10^6 Pa	8.96×10^7 dyne/cm^2	tauz
τ_m - Strength at Pmax	3.313×10^8 Pa	3.313×10^9 dyne/cm^2	taum
Pmax	5.0×10^8 Pa	5.0×10^9 dyne/cm^2	pyld

4.1.1 Micromechanical Test Cases

The Sammis micromechanical damage model has several parameters, some of which can be determined experimentally. P and S velocities are derived from the properties in Table 1.

Table 2. Sammis model properties for granite

Property	Value (SI)	Value (CGS)	Definition
vp	5175 m/s	5.175×10^5 cm/s	P velocity
vs	3026 m/s	3.026×10^5 cm/s	S velocity
vr	2723 m/s	2.723×10^5 cm/s	Rayleigh velocity
vm	1000 m/s	1.000×10^5 cm/s	Max crack speed
K1C	1.0×10^6 Pa-m$^{1/2}$	1.0×10^8 dyne/cm^2-cm$^{1/2}$	Stress intensity factor
a	0.0001 m	0.01 cm	Crack half-width
f	0.6	0.6	Coefficient of friction
D_0	0.1	0.1	Initial damage

Other properties needed for calculations can be derived from these:

$$\Psi = 0.5 * \tan^{-1}\left(1/f\right)$$
$$\alpha = \cos(\Psi) \qquad (15)$$

$$N_v = \frac{3}{4\pi}\frac{D_0}{(a\alpha)^3} \tag{16}$$

N_v is the density of initial cracks that are optimally oriented for sliding – cracks per unit volume. For the parameters above, N_v is 36 cracks/cm^3 (36x10^6/m^3). Ψ is the angle of the optimally oriented crack measured from the direction of the maximum principal stress.

The properties used here are those used in Ashby and Sammis for granite, except that D_0 is increased to 0.1 from 0.01 and a is 1 mm instead of 0.5 mm and the coefficient of friction is 0.60 instead of 0.64.

Of these properties, the two most likely to vary are the crack size a and the initial damage D_0. For the following parameter study we left D_0 fixed. Since the crack size is very likely to scale with problem size, we performed tests with values of one millimeter, one centimeter, 10 centimeters and one meter. Note that any change in *a* also changes the crack density according to the equation above. Changing a from 0.1 mm to 1 m decreases *Nv* by 10^{12} which is one crack per 30,000 m3 (about a 30 meter/side block).

For a spherically symmetric problem, we can take the principal stress σ_1 to be in the radial direction. σ_2 and σ_3 are equal. In an explosion, there is an initial pulse of high pressure, which causes a radial compressive strain and compressive stress. In the axial direction, there is compressive stress, but tensile strain as the material is forced to expand axially.

In addition to varying the initial crack size, we also vary the other nonlinear effects that can occur during the explosion. We ran 9 variations (Table 3); each of these were run four times for the different crack sizes. All cases allowed tensile cracking after, but not before, plastic yielding had occurred. Three of them used the reduced strength model described above. Three of the cases used the elastic moduli throughout and six used the damage dependent moduli calculated using the Sammis microdamage model.

Table 3. Nonlinear options used in test runs.

Case #	Shear modulus reduction	Plastic yielding allowed before microdamage failure	Microdamage moduli instead of elastic moduli	Weakened shear strength
1	Off	Off	Off	Off
2	On	Off	Off	Off
3	On	On	Off	Off
4	Off	Off	On	Off
5	On	Off	On	Off
6	On	On	On	Off
7	Off	Off	On	On
8	On	Off	On	On
9	On	On	On	On

Calculated cavity radii are listed in Table 4. Table 5 shows calculated reduced displacement potential (RDP). Table 6 shows the maximum extent of plastic yielding. Table 7 shows the maximum extent of full damage and Table 8 the maximum extent of partial damage. For the new calculations "partial damage" means that the cracks in the cell have extended according to the

micromechanical damage model. “full damage” means that cracks have reached unstable failure. For the Shoal model, “damage” means that enough plastic work has accumulated to reduce the strength in the cell, “full damage” means that the strength is reduced continuously from the origin, “partial damage” is discontinuous beyond the full damage extent. The measured cavity radius for Shoal was 25.6 meters (Beers, 1964).

Table 4. Calculated final cavity radii (meters)

Case #	N/A	a=1mm	a=1cm	a=10cm	a=1m
Shoal	20.58				
1		15.88	15.73	15.69	15.16
2		15.91	15.72	15.75	15.58
3		16.09	16.17	16.20	16.17
4		15.85	15.63	15.64	15.07
5		15.79	15.76	15.69	15.28
6		16.01	16.13	16.16	16.13
7		22.93	22.91	23.00	22.35
8		22.12	22.15	22.21	21.71
9		20.22	22.49	22.55	22.54

Table 5. Calculated reduced displacement potential (m^3)

Case #	N/A	a=1mm	a=1cm	a=10cm	a=1m
Shoal	1760				
1		717	696	691	623
2		720	697	709	682
3		809	759	773	771
4		713	678	684	616
5		705	696	693	641
6		778	746	757	758
7		2176	2155	2175	2021
8		1952	1945	1967	1844
9		1755	2034	2061	2060

Table 6. Radius of plastic yielding (m)

Case #	N/A	a=1mm	a=1cm	a=10cm	a=1m
Shoal	266.6				
1		156.8	171.2	174.2	165.4
2		156.8	171.2	174.2	171.2
3		183.3	180.2	183.3	183.3
4		156.8	162.5	165.4	145.8
5		154.0	168.3	168.3	151.3
6		180.2	174.2	174.2	162.5
7		219.1	240.3	247.6	219.1
8		222.5	240.3	251.3	219.1
9		278.5	247.6	255.1	236.6

Table 7. Radius of full damage (m)

Case #	N/A	a=1mm	a=1cm	a=10cm	a=1m
Shoal	137.9				
1		156.8	171.2	195.8	174.2
2		156.8	171.2	199.1	180.2
3		115.3	180.2	208.9	192.7
4		156.8	162.5	180.2	151.3
5		154.0	168.3	183.3	156.8
6		127.6	174.2	192.7	168.3
7		219.1	240.3	266.6	226.0
8		222.5	243.9	266.6	229.5
9		132.7	247.6	274.5	243.9

Table 8. Radius of partial damage (m)

Case #	N/A	a=1mm	a=1cm	a=10cm	a=1m
Shoal	148.6				
1		156.8	192.7	233.0	243.9
2		156.8	192.7	236.6	255.1
3		143.1	202.3	247.6	274.5
4		156.8	189.5	233.0	240.2
5		156.8	192.7	236.6	243.9
6		132.7	199.1	247.6	266.6
7		219.1	278.5	338.9	353.0
8		222.5	278.5	343.6	357.8
9		208.9	286.7	353.0	377.4

Table 9. Minimum P velocity

Case #	N/A	a=1mm	a=1cm	a=10cm	a=1m
Shoal	4438				
1		5179	5179	5179	5179
2		4445	4445	4445	4445
3		4447	4445	4445	4445
4		5179	5179	5179	5179
5		4445	4445	4445	4445
6		4446	4445	4445	4445
7		5178	5178	5178	5178
8		4443	4443	4443	4444
9		4445	4443	4443	4443

4.1.2 Comparison with Shoal

Shoal had three shot level stations each located 120 degrees apart (Figure 5) at a distance approximately to 590 meters from the shot. Stevens and Thompson (2015) modeled this explosion using the 3D finite element code CRAM3D, and including tectonic stresses. Stevens and Thompson were able to match the general character of the waveforms including variability from tectonic release, however they were not able to match the waveforms exactly. In particular, although the calculations clearly showed an increase in amplitude in the direction of PM-3, they could not match the very large observed amplitude at that station. The data at these three stations and the results of that calculation are shown in Figure 6.

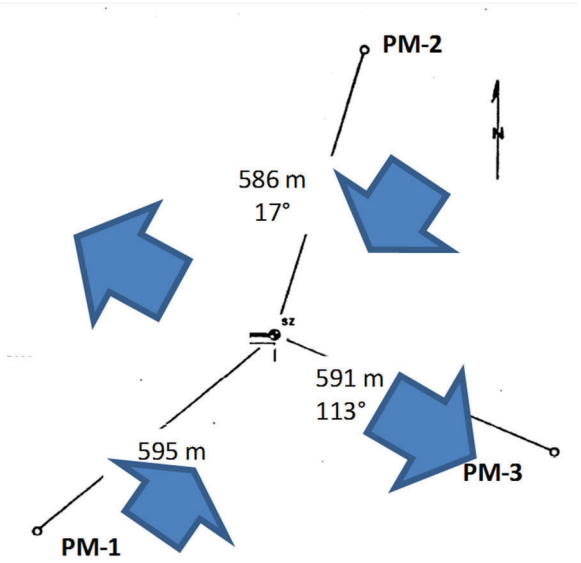

Figure 5. Location of the Shoal explosion and the three nearfield shot level recording stations and the direction of the local stress state.

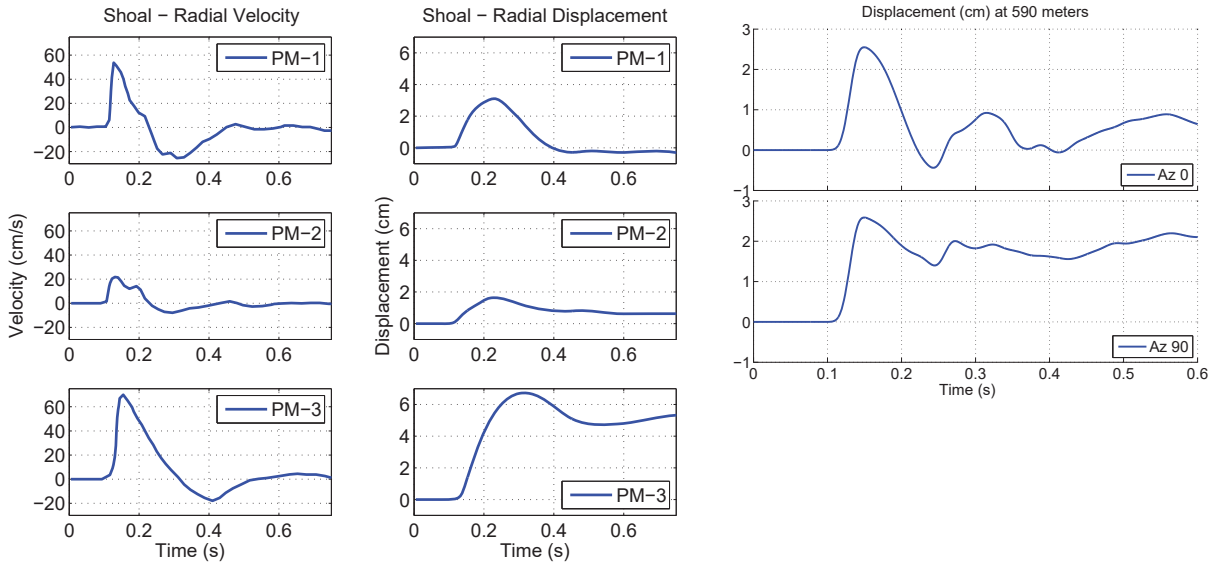

Figure 6. Left: radial velocity and displacement recorded at the three stations. Right: calculation at zero and 90 degrees. Zero degrees is the direction of PM-1. Note the similarity between the PM-1 displacement and the zero degree calculated waveform, and PM-3 and the 90 degree calculated waveform.

In 1D we cannot include tectonic stresses or other 3D effects, but it is still useful to compare with the data. The Shoal calculation in the tables above used identical material properties to the CRAM3D calculation, with a constant pressure corresponding to the overburden pressure at the shot depth. A comparison of the near-field shot-depth waveforms is shown in Figure 7. Excluding the anomalous station 3, which clearly shows the effect of tectonic stresses, the main difference between the calculated and observed data is that the calculated velocity has a sharper initial peak, and both the observed velocity and displacement are spread out over a longer period of time. This most likely means that the Shoal granite is weaker than the granite model.

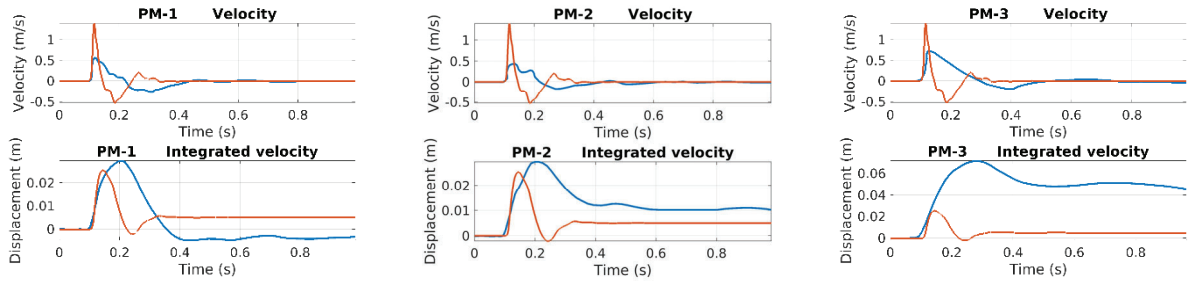

Figure 7. Comparison of SKIPPER calculations of Shoal at 590 meters (red) with recorded data (blue). Observed displacements are all integrated velocity.

The Shoal granite model was derived by combining two granite models, one for Piledriver and one for Degelen Mountain that was developed in an earlier study (Stevens et al, 2003). The Degelen Mountain granite was stronger than the Piledriver granite (NTS Climax Stock Granite). As discussed above, the shear failure model has three parts: an initial strength model corresponding to the laboratory strength of fractured granite, a post-failure model of weakened, crushed granite, and a model based on shear strain that defines how the strength reduction occurs (Figure 4).

In the same report, we studied several other material models. This model was referred to as the Yield/Failure Surface/Shock Damage (YF-SS) model. In the same study, we implemented an early version of the Sammis damage mechanics model. The damage mechanics model was used until unstable crack growth occurred, after which it was replaced by the shock damage model (SA-SS). We also studied acoustic fluidization as a post-failure model. We compared the results with data from Piledriver and Degelen Mountain and found that we achieved the best results with the SA-SS model. Figure 8 shows the comparison with near-field Piledriver waveforms. Although the calculated waveforms are low compared to the data at the closest two stations, the waveforms are quite good at the next two stations. The calculations also have the long negative velocities observed in the data. As shown in Stevens et al (1986), Rimer et al (1987) and earlier reports, an effective stress model was developed that matched the first two stations quite well, but did not do as well farther out. Figure 9 shows calculated and observed waveforms from one Degelen Mountain explosion with a very good data fit at four locations. The main difference between the Degelen and Piledriver models is a weakened coefficient of friction of 0.2 vs. 0.02, respectively.

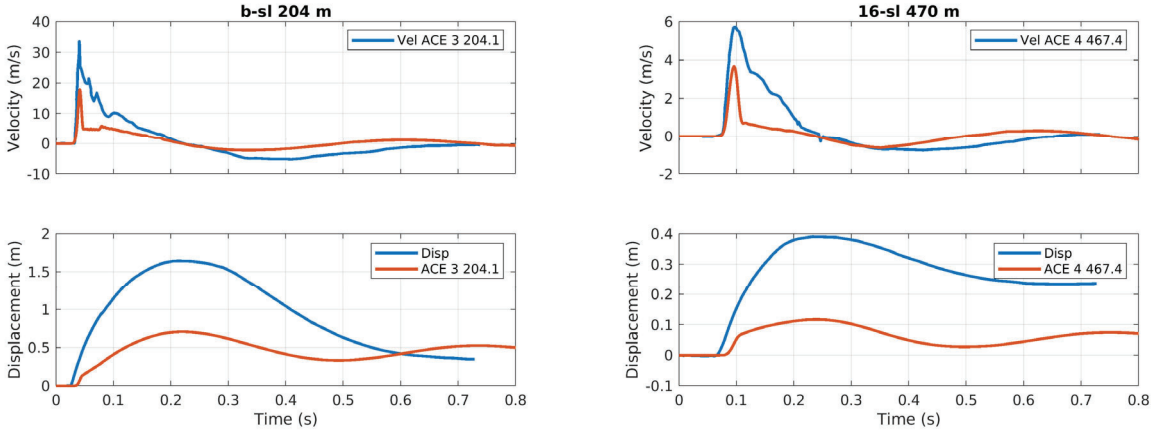

Figure 8. Calculated (red) and observed (blue) waveforms from the 62 kt explosion Piledriver using the SA-SS model.

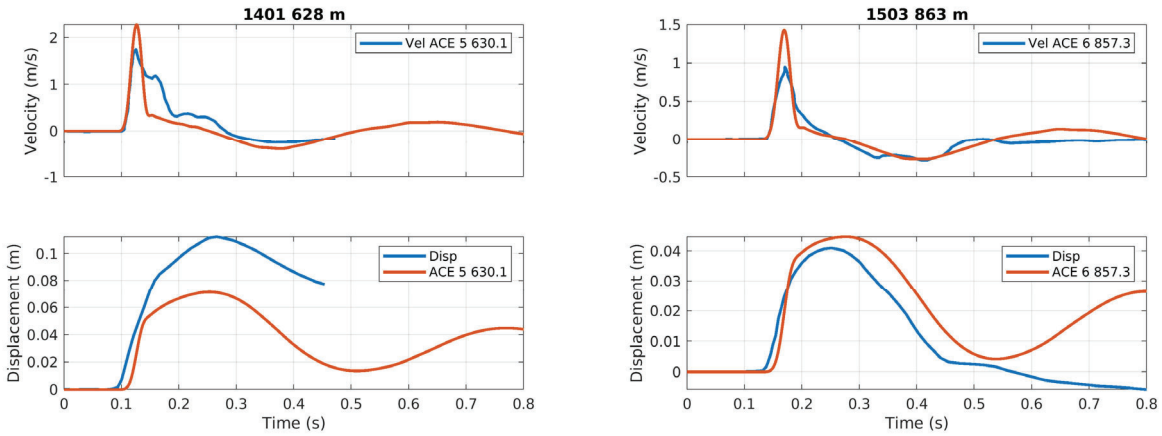

Figure 8 (continued). Calculated (red) and observed (blue) waveforms from the 62 kt explosion Piledriver using the SA-SS model.

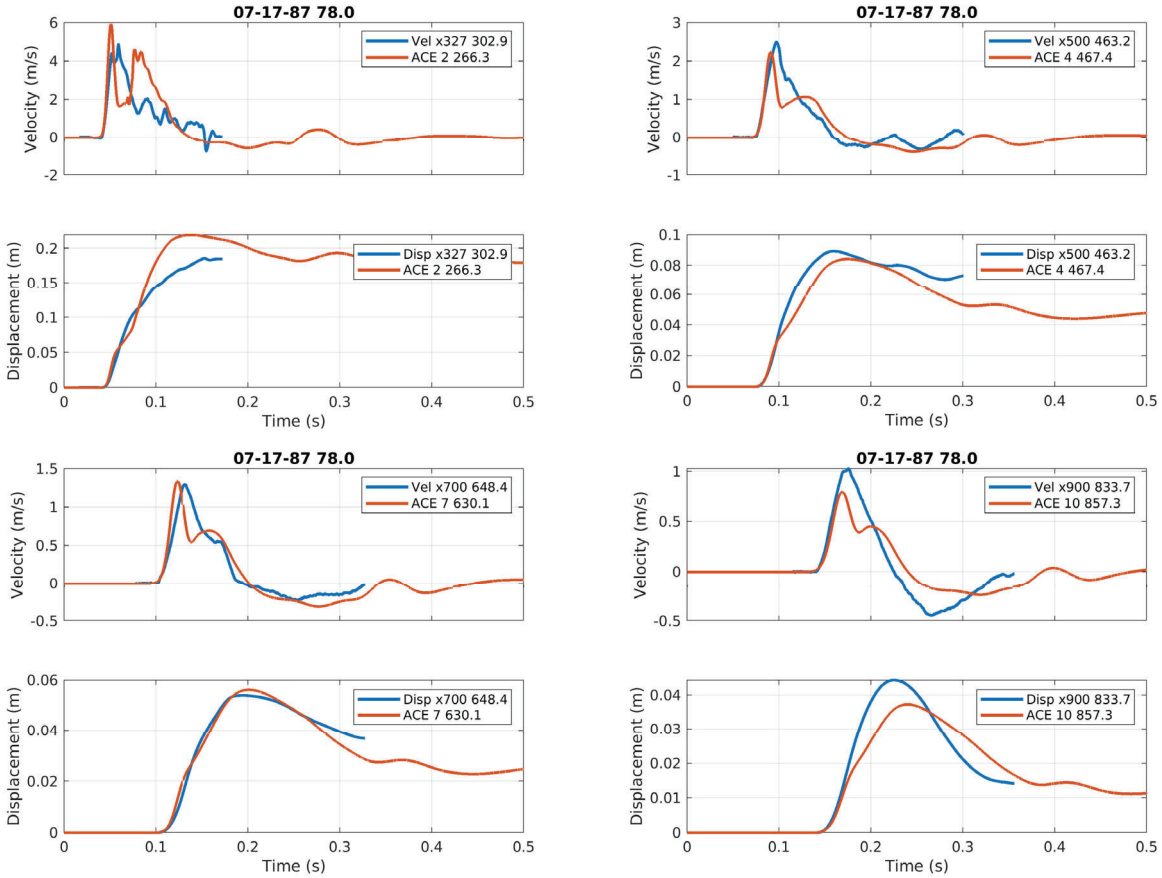

Figure 9. Calculated (red) and observed (blue) waveforms from the 78 kt 1987/07/17 Degelen Mountain explosion using the SA-SS model.

Plots were made for all of the cases above, and we show a subset here. Figure 10 shows all waveforms for case #9 with a=1 cm. The waveforms are very similar to the Shoal calculation. Figure 11 shows a comparison of the Shoal waveforms with the other crack sizes, also for case #9. The 1 cm case has slightly larger amplitudes than the others, with the smallest amplitudes at 1 mm and 1 m.

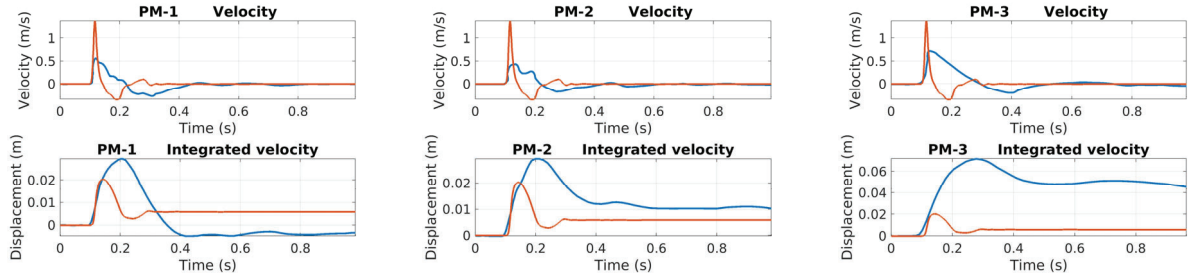

Figure 10. Case 7 with a=1 cm.

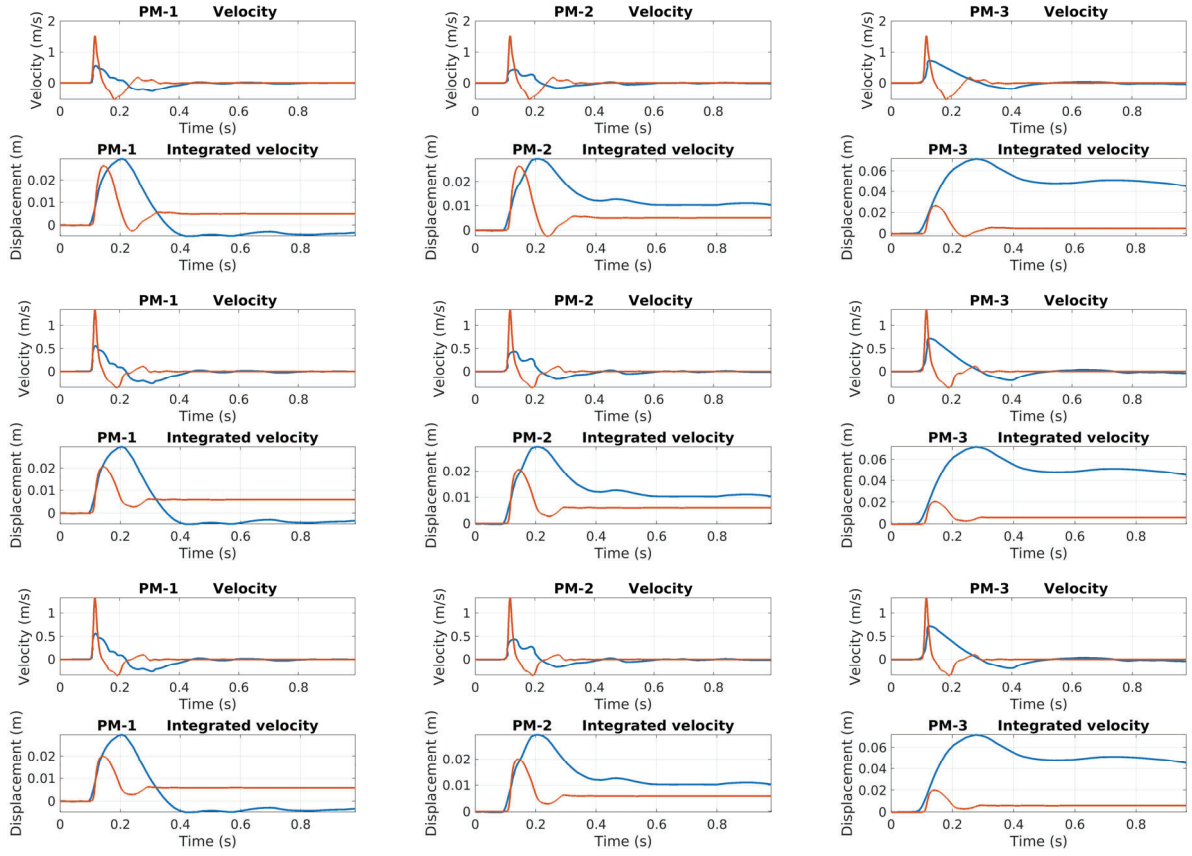

Figure 11. Calculated velocity waveforms (red) compared with Shoal data (blue) for case 9. Top row a=1mm, middle row a=10cm, bottom row a=1m.

One reason calculation #9 is so similar to the Shoal calculations is that case #9 includes most of the same nonlinear effects, particularly strain weakening and shear modulus reduction. The main difference are that case #9 uses the Sammis model and damage-dependent moduli pre-failure. Velocity waveforms for all cases are shown together in Figure 12.

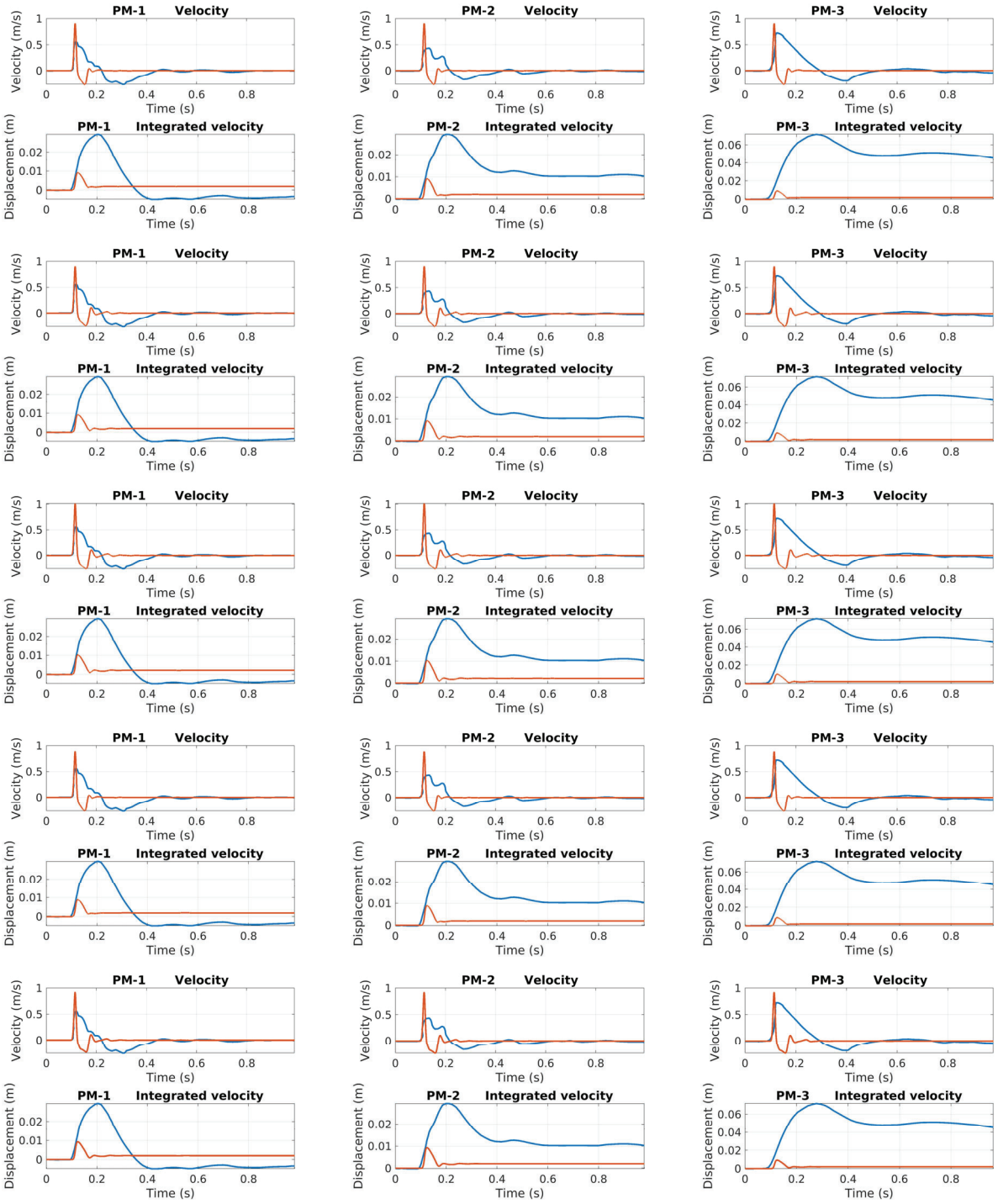

Figure 12. From top to bottom cases 1,2,3,4,5,6,7,8,9, velocity waveforms. All for 1 cm crack size.

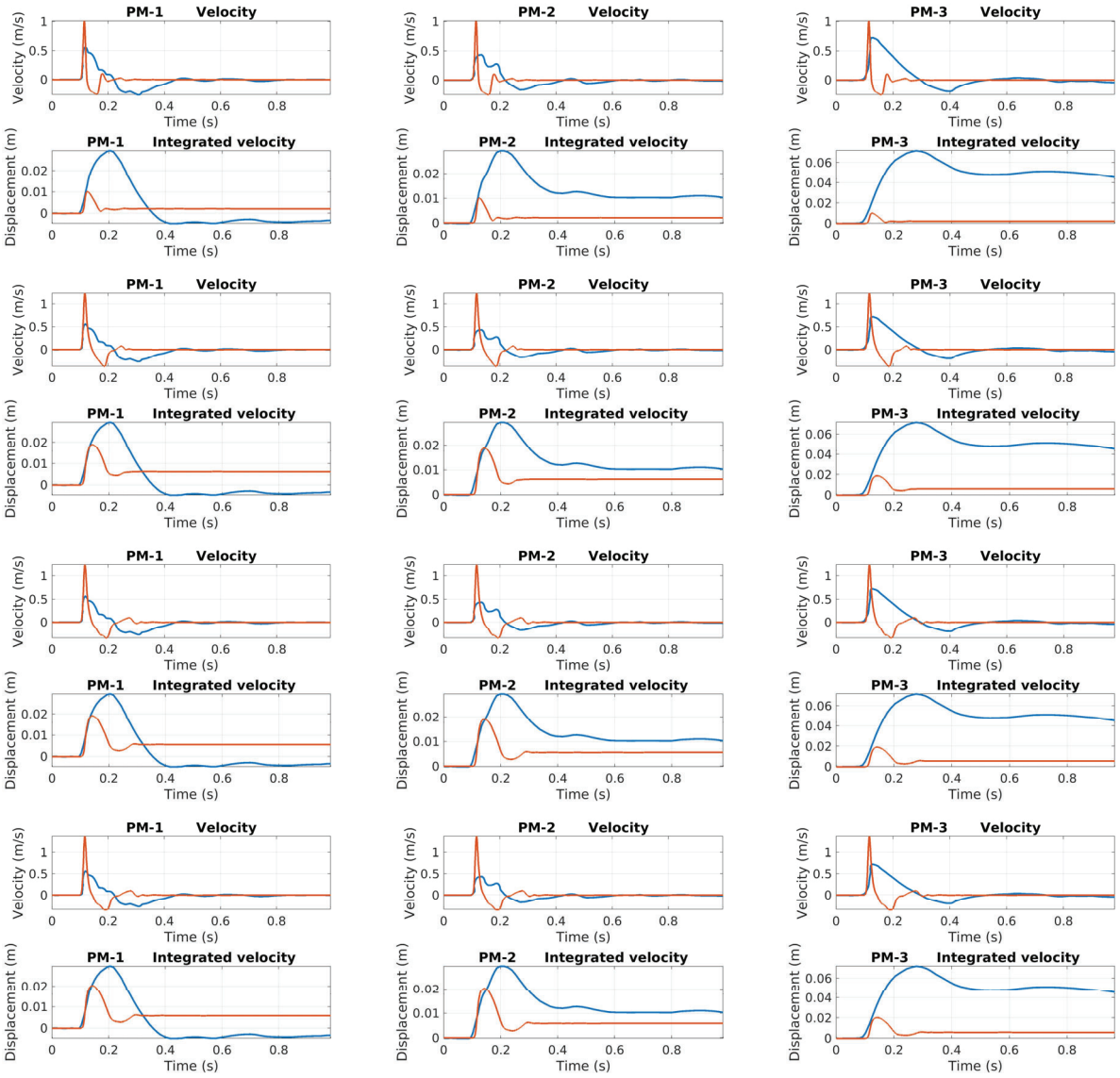

Figure 12 (continued). From top to bottom cases 1,2,3,4,5,6,7,8,9, velocity waveforms. All for 1 cm crack size.

A few conclusions can be drawn from these. First only cases 7, 8 and 9 have the broadening of the waveform and long negative pulse that is observed in the data. Cases 7, 8 and 9 are very similar: case 7 is slightly shorter in duration and case 9 slightly higher in amplitude than the others. The difference between cases 7 and 8 and case 9 is that Case 9 allows shear failure before damage due to cracks is complete. The motivation for including this is that near the cavity where stresses are very high and shear failure is physically reasonable. The difference between cases 7 and 8 is that case 8 has shear modulus reduction after failure (also included in case 9). One of the motivations for this is that compressional velocities were observed to decrease near the cavity in the Degelen explosions, but it makes surprisingly little difference in the waveforms, at least at this distance range.

4.1.4 Calculated Damage

The calculations led to a variety of damage distributions. For the cases where plastic yielding was allowed before microcrack failure (3, 6, 9), yielding dominated close to the source and full damage did not occur in that region, but occurred farther out. There are also significant differences in the range of the damage depending on initial crack size (Figure 13, Figure 14, Figure 15).

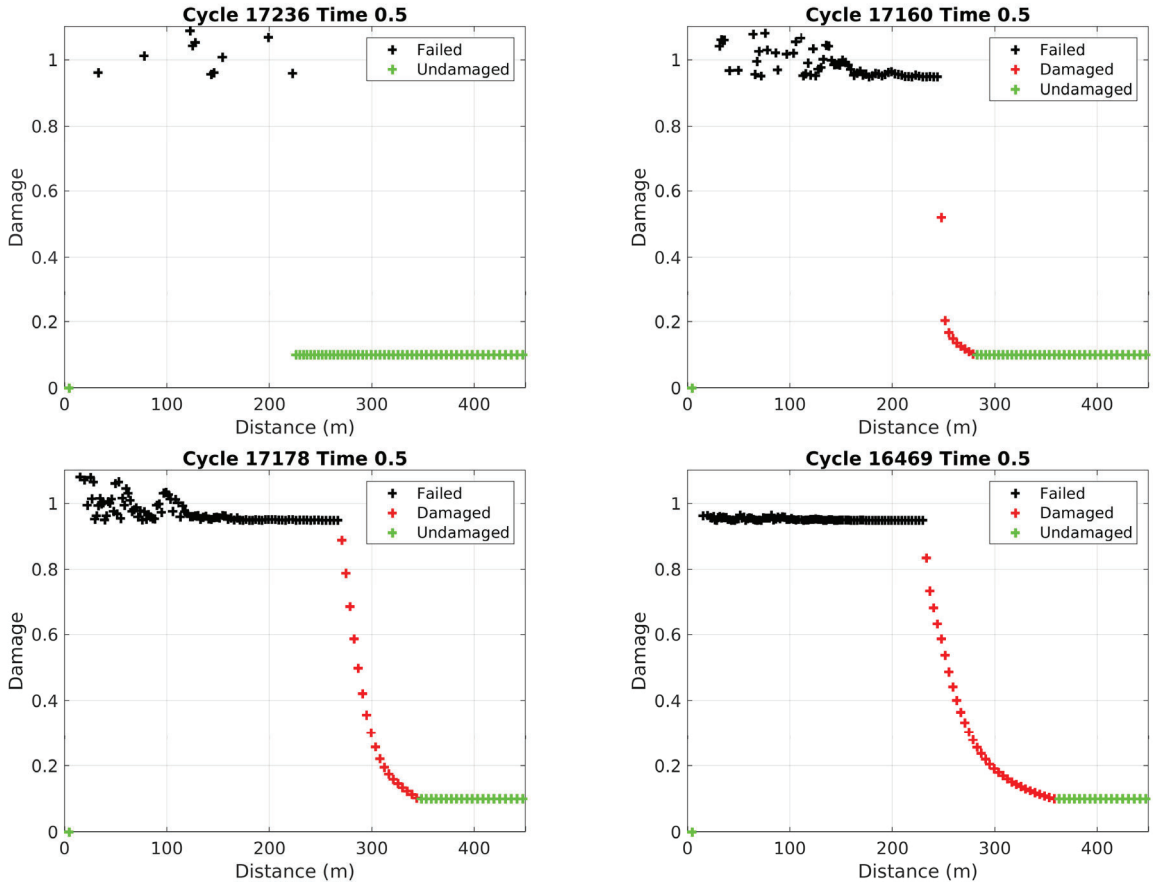

Figure 13. Final damage for case #8. Top left: a=1mm, top right a=1cm, bottom left a=10cm, bottom right a=1m. Microdamage failure is required before yielding can occur.

Microcrack failure is defined to occur when damage exceeds 0.95. From equations 5 and 6, we can relate damage to crack length. Using $D_{\max}$ =0.95 at failure:

$$\frac{D}{D_0}=\left(1+\frac{l}{\alpha a}\right)^3 \; ; \; l=\alpha a\left[\left(\frac{D}{D_0}\right)^{1/3}-1\right] \; ; \; l_{\max}=0.973a \text{ for } D_0=0.1, fric=0.6, \alpha=0.87 . \qquad (16)$$

For the smallest initial crack size, the crack length may extend significantly beyond $l_{\max}$ in a single time step, so D exceeds 1 at failure, while for the larger initial crack sizes, the final damage stays close to D=0.95.

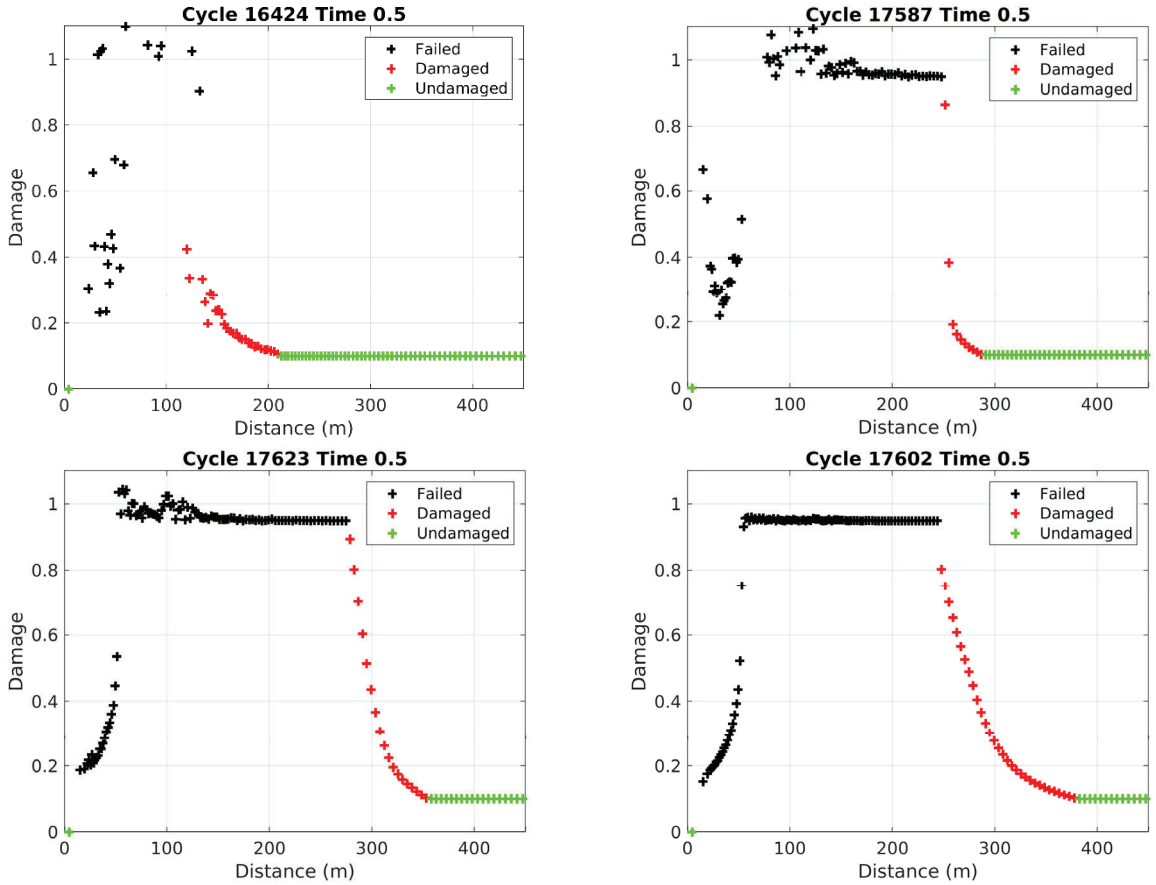

Figure 14. Final damage for case #9. Top left: a=1mm, top right a=1cm, bottom left a=10cm, bottom right a=1m. Yielding can occur before microdamage failure. Close to the cavity where failed points have damage less than 0.95 are locations where failure occurred through yielding instead of microcrack failure.

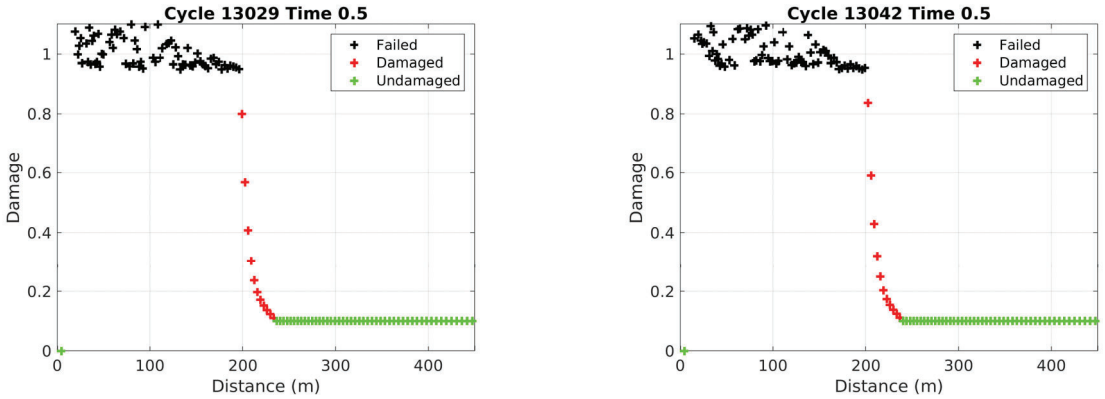

Figure 15. Final damage for all cases, a=10 cm. Top: case 1 (left), case 2 (right); row 2: case 3 (left), case 4 (right), row 3: case 5 (left), case 6 (right), row 4: case 7 (left), case 8 (right); bottom: case 9.

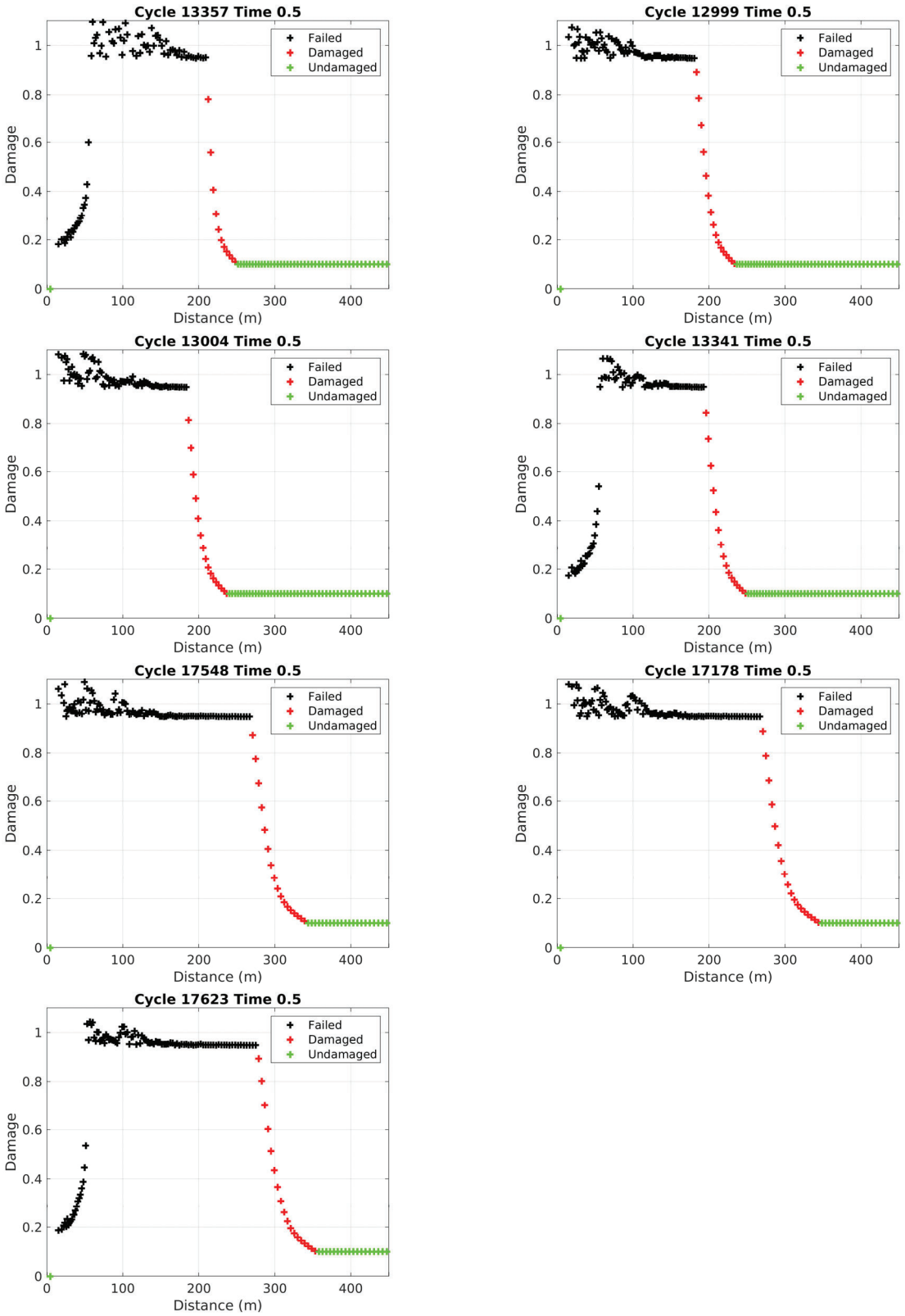

Figure 15 (continued). Final damage for all cases, a=10 cm. Top: case 1 (left), case 2 (right); row 2: case 3 (left), case 4 (right), row 3: case 5 (left), case 6 (right), row 4: case 7 (left), case 8 (right); bottom: case 9.

More results from these calculations are shown in Appendix B.

4.2 Comparison with Degelen Mountain Near-Field Data

In Stevens et al (2003), we compared calculations from an early version of the micromechanical damage model with shot level data from underground nuclear explosions at the former Soviet test site at Degelen Mountain. One example was shown earlier in Figure 9. Here we compare the same data set with the results of Shoal calculation #9 with a=10cm. To make this comparison we scale all of the data, both calculated and observed to a common yield of 12.5 kilotons. The waveforms shown are the closest distance used in the calculation to the scaled distance in the observation. The legend in each figure shows the actual distance (e.g. x90), the distance scaled to 12.5 kt, following that number, and the calculated distance shown as "ACE station# calculated distance". This figure can be compared with figure 29 from Stevens et al (2003), which shows the same data together with calculations using the older quasistatic model. Here we have also integrated the velocity data to get displacement data. The data fit is at least as good as the 2003 report, which is quite remarkable since we were not explicitly trying to fit it. Furthermore it is a better data fit than we got to the Shoal data, which we were trying to model.

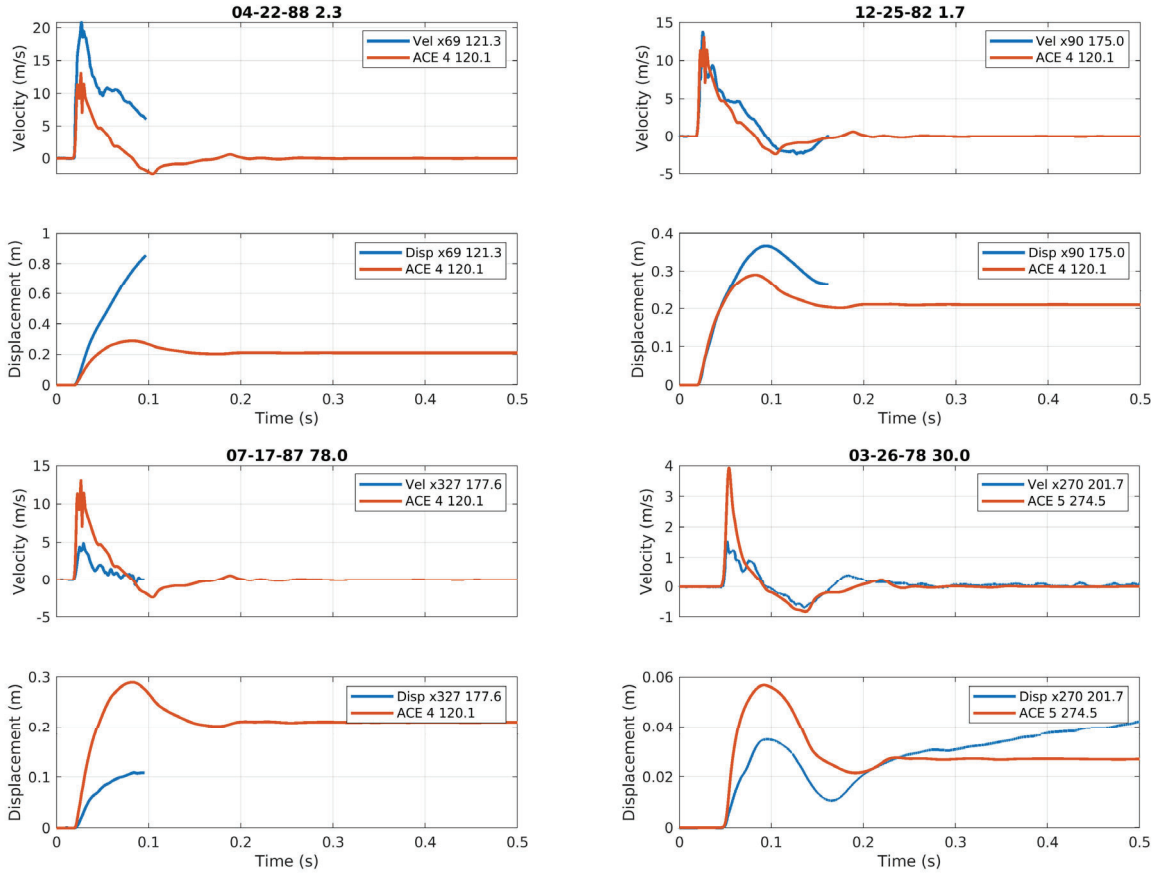

Figure 16. Shot level data from Degelen Mountain explosions compared to Shoal calculation #9 with a=10cm. The original data is the velocity data shown in blue in the upper half of each figure. The displacement data was obtained by integrating the velocity.

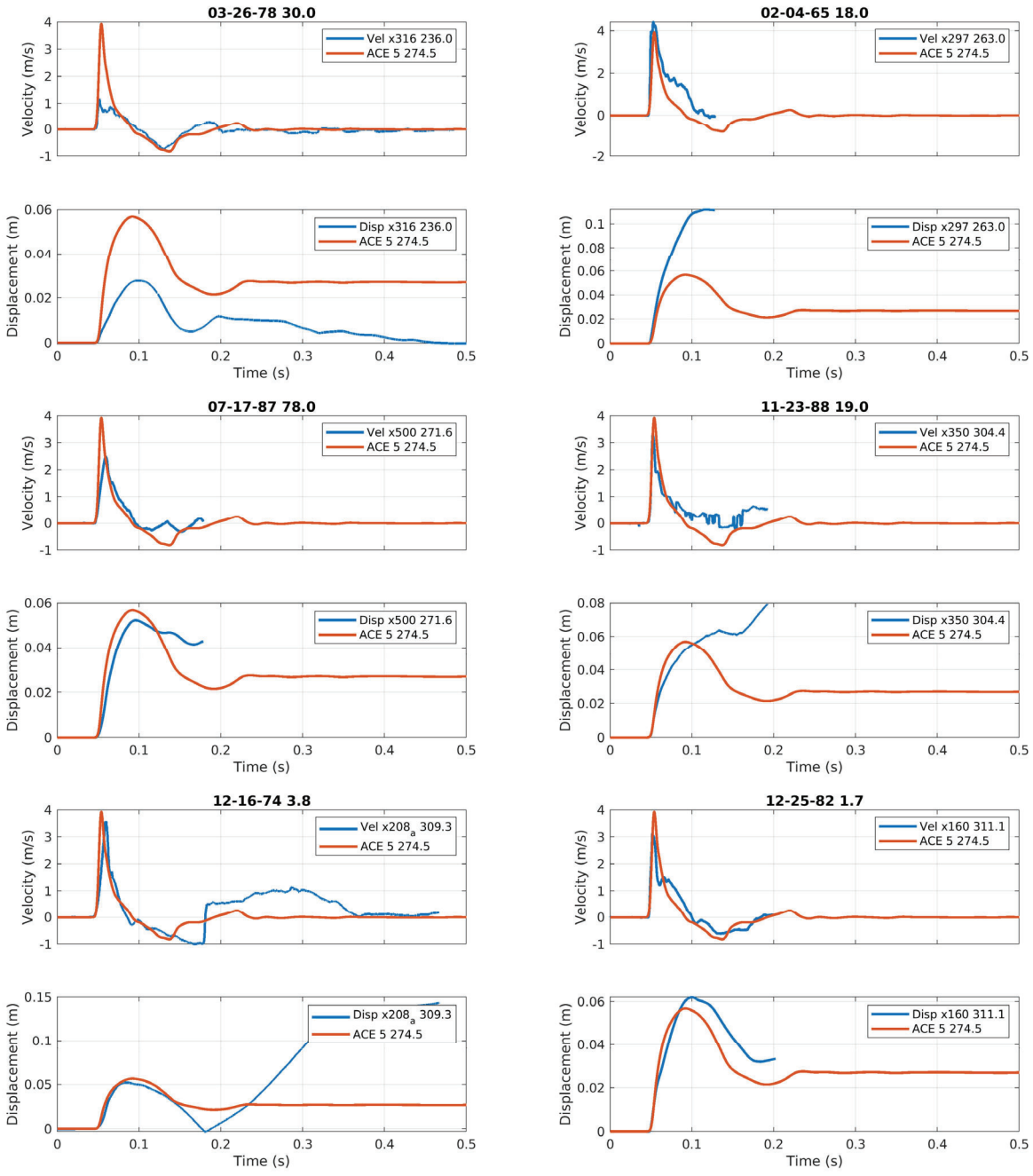

Figure 16 (continued). Shot level data from Degelen Mountain explosions compared to Shoal calculation #9 with a=10cm. The original data is the velocity data shown in blue in the upper half of each figure. The displacement data was obtained by integrating the velocity.

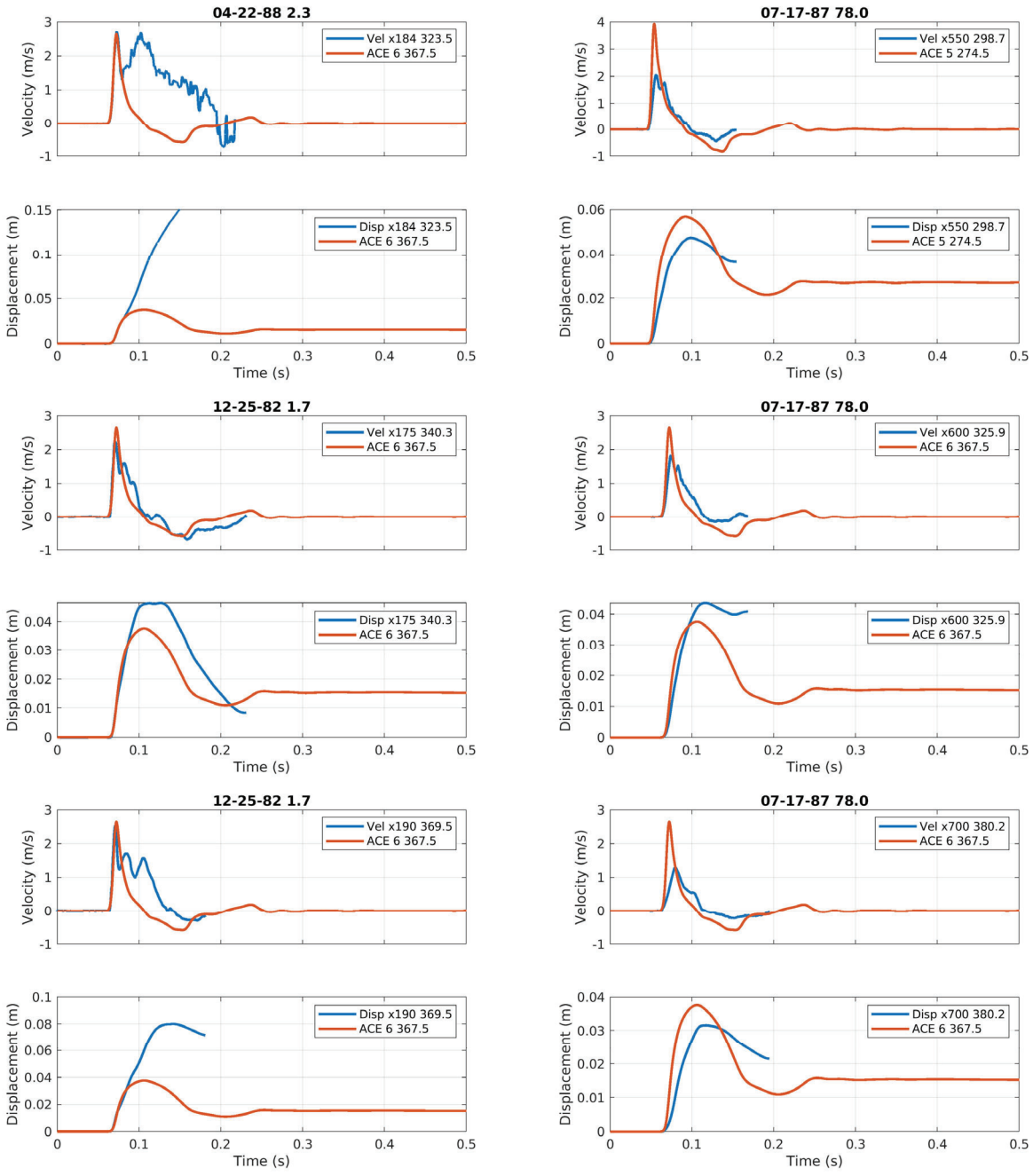

Figure 16 (continued). Shot level data from Degelen Mountain explosions compared to Shoal calculation #9 with a=10cm. The original data is the velocity data shown in blue in the upper half of each figure. The displacement data was obtained by integrating the velocity.

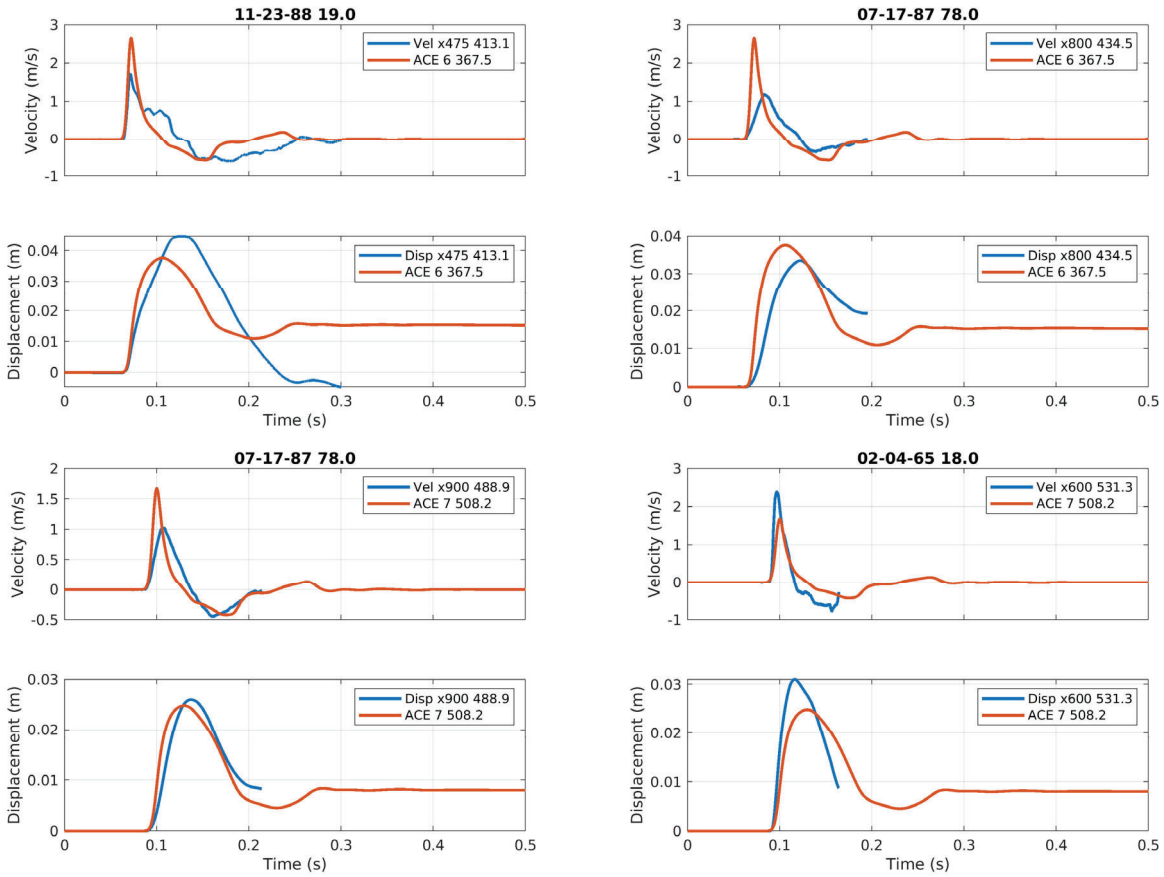

Figure 16 (continued). Shot level data from Degelen Mountain explosions compared to Shoal calculation #9 with a=10cm. The original data is the velocity data shown in blue in the upper half of each figure. The displacement data was obtained by integrating the velocity.

4.3 Comparison with Piledriver Data

In the 2003 study, we also compared our calculations with Piledriver, using a slightly different model. See Figure 24 of the 2003 report and Figure 8 above. As in the earlier study, the amplitudes at the first two stations are low, but the calculation has the same long negative velocity pulse as the data, and the data fit is fairly good at the two more distant stations.

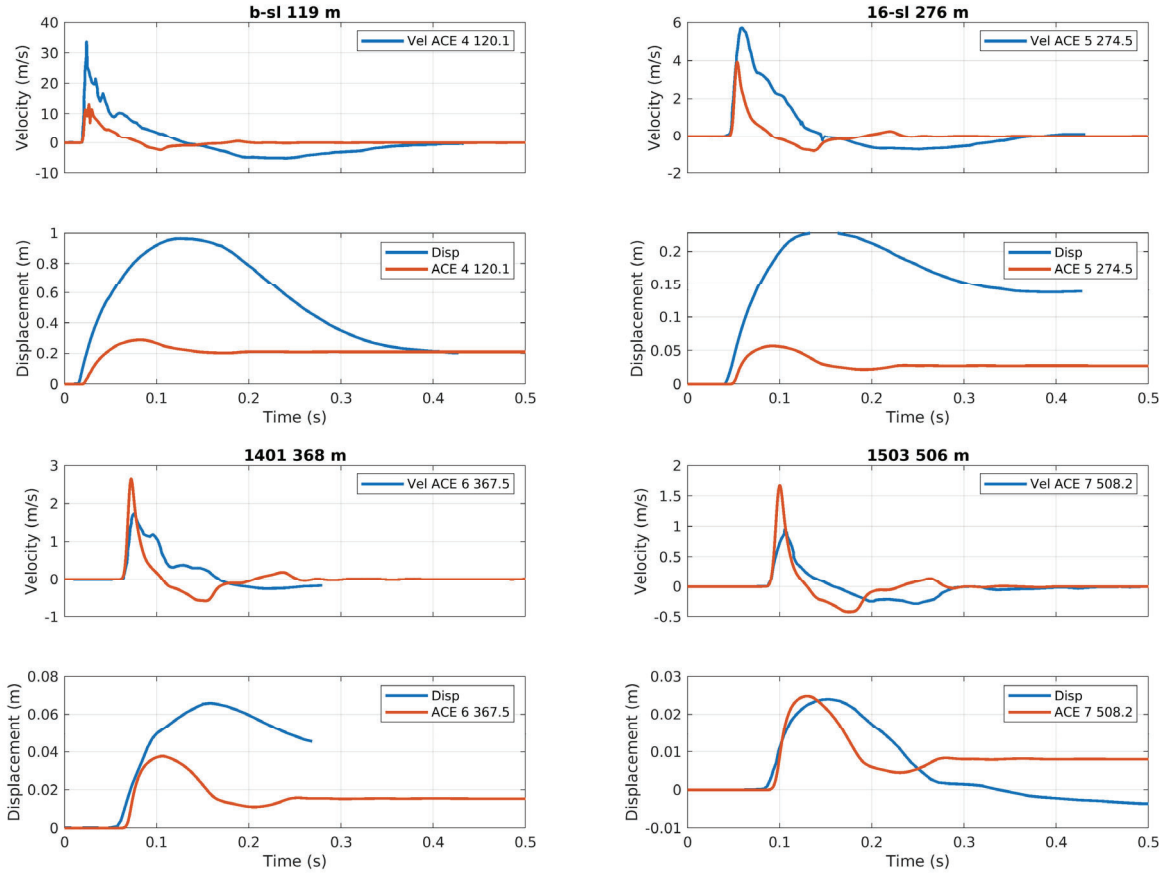

Figure 17. Comparison Piledriver near-field data with Calculation #9 and a=10cm.

4.4 Conclusions from One-dimensional Analysis

We have implemented the latest version of the Sammis micromechanical damage model in our spherically symmetric nonlinear finite difference code SKIPPER, using a Fortran 90 module that can be added unchanged to our CRAM3D nonlinear finite element code. We have run an extensive set of calculations using the spherically symmetric code and compared the results with data from nuclear explosions Shoal and Piledriver as well as a series of explosions at the Degelen Mountain test site. We have used this to determine a baseline case, described as Case #9 above, which is most consistent with all of the data. Remarkably, the new model gives a better data fit to the Degelen data than the 2003 model, and also gives a reasonably good data fit to the Piledriver data without changing any parameters. We use this model as our starting model in the CRAM3D calculations.

5. RESULTS FROM 3D CALCULATIONS

5.1 Comparison of 1D and 3D results for Nine Material Models

We ran a series of calculations corresponding to all of the 1D models described earlier, in a 3D grid modeled after the Shoal calculation (Stevens and Thompson, 2015), but with the new material models. All were done with an initial flaw size of a=10 cm. We did a number of comparisons to see how the 1D and 3D results compared. For the first comparison, we plotted a radial waveform 100 meters horizontally from the source together with the 1D waveform at a distance of 100 meters (Figure 18). There are some small differences for some of the models, but in general they are quite consistent.

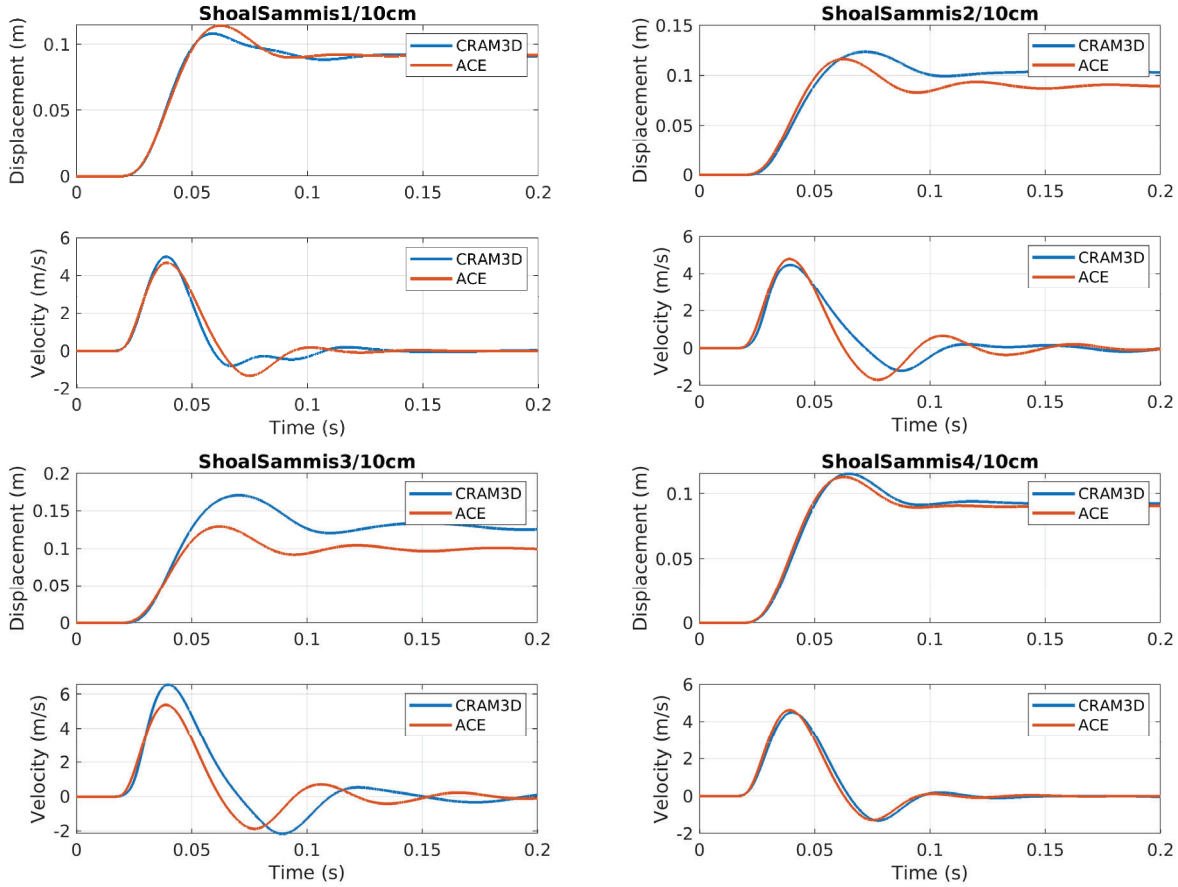

Figure 18. Comparison of 1D and 3D waveforms at a distance of 100m from the source for each set of material models used in the 1D study described earlier, with a=10cm. Case number is in the title. All waveforms were lowpass filtered at 20 Hz.

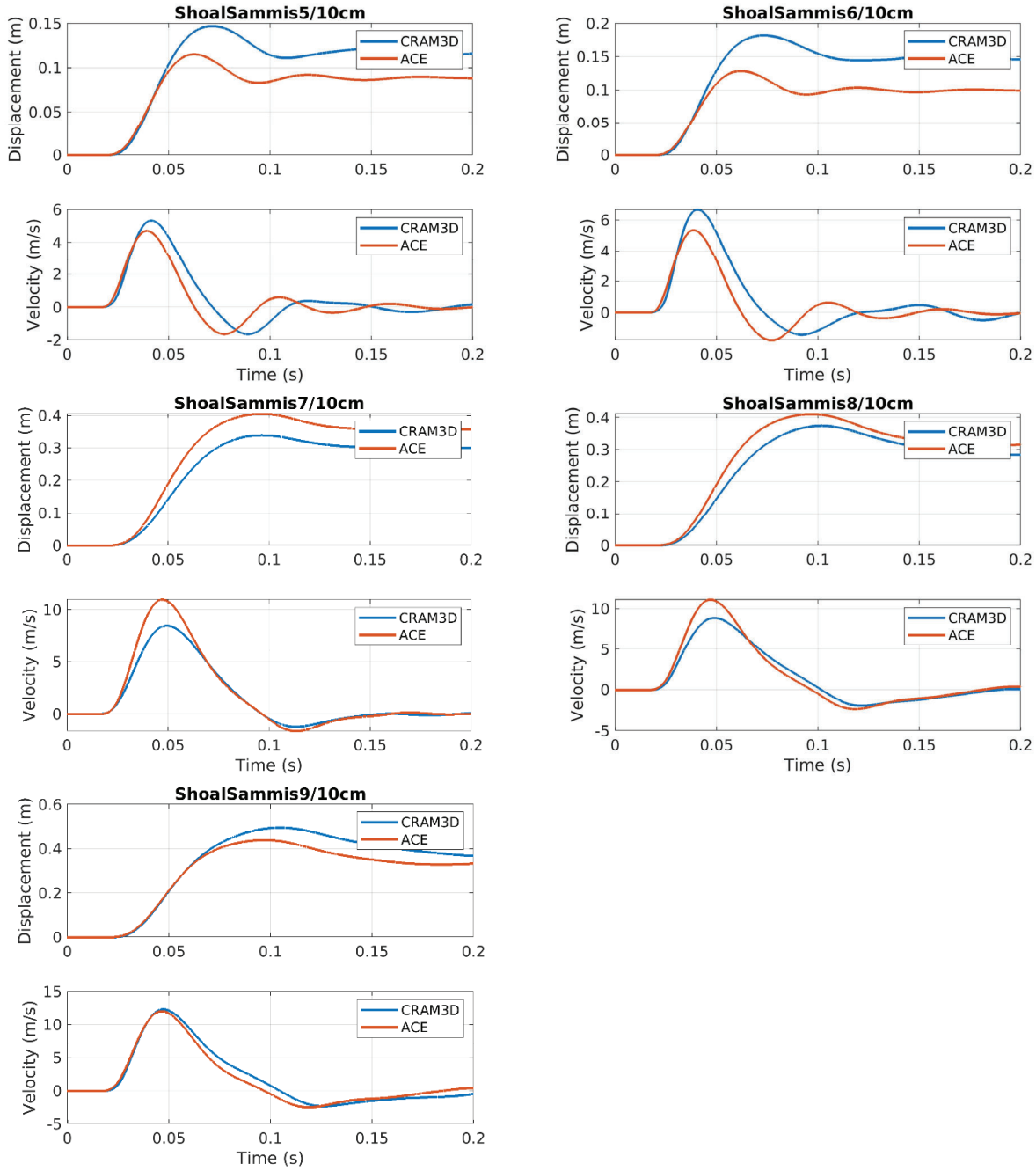

Figure 18 (continued). Comparison of 1D and 3D waveforms at a distance of 100m from the source for each set of material models used in the 1D study described earlier, with *a*=10cm. Case number is in the title. All waveforms were lowpass filtered at 20 Hz.

To assess the variability in different directions, we plotted Cram3D radial waveforms for each model in four horizontal directions and directly below the source all at a distance of 100 meters. The four horizontal waveforms were identical in each case, while the waveform below the source was slightly different in shape and lower in amplitude (Figure 19).

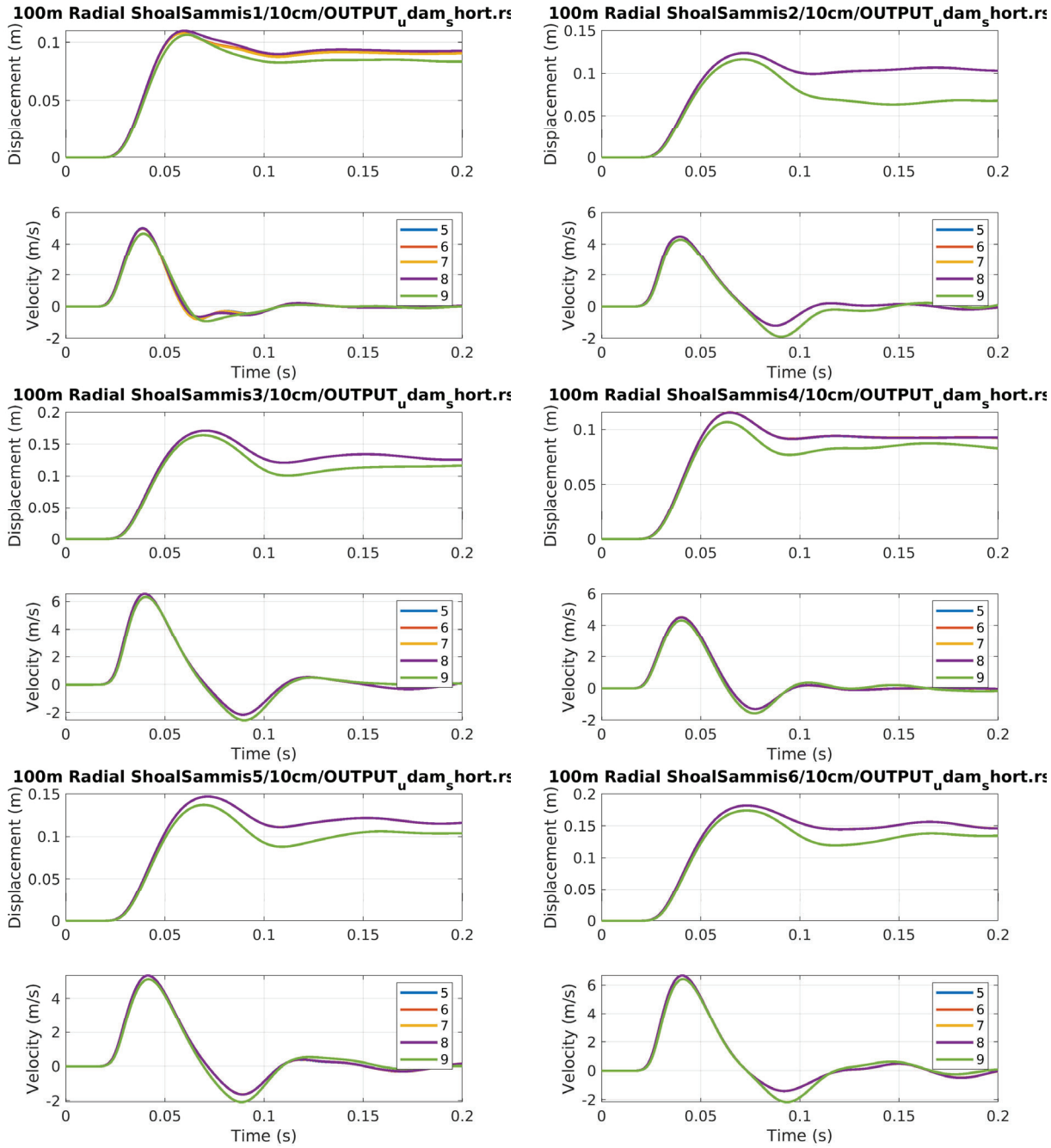

Figure 19. Radial (outward from source center) waveforms at 5 locations. Locations 5-8 are the four horizontal directions along each axis at source depth. Location 9 is directly below the source. All are at a distance of 100 meters from the source center. Case number is in the title. All waveforms were lowpass filtered at 20 Hz.

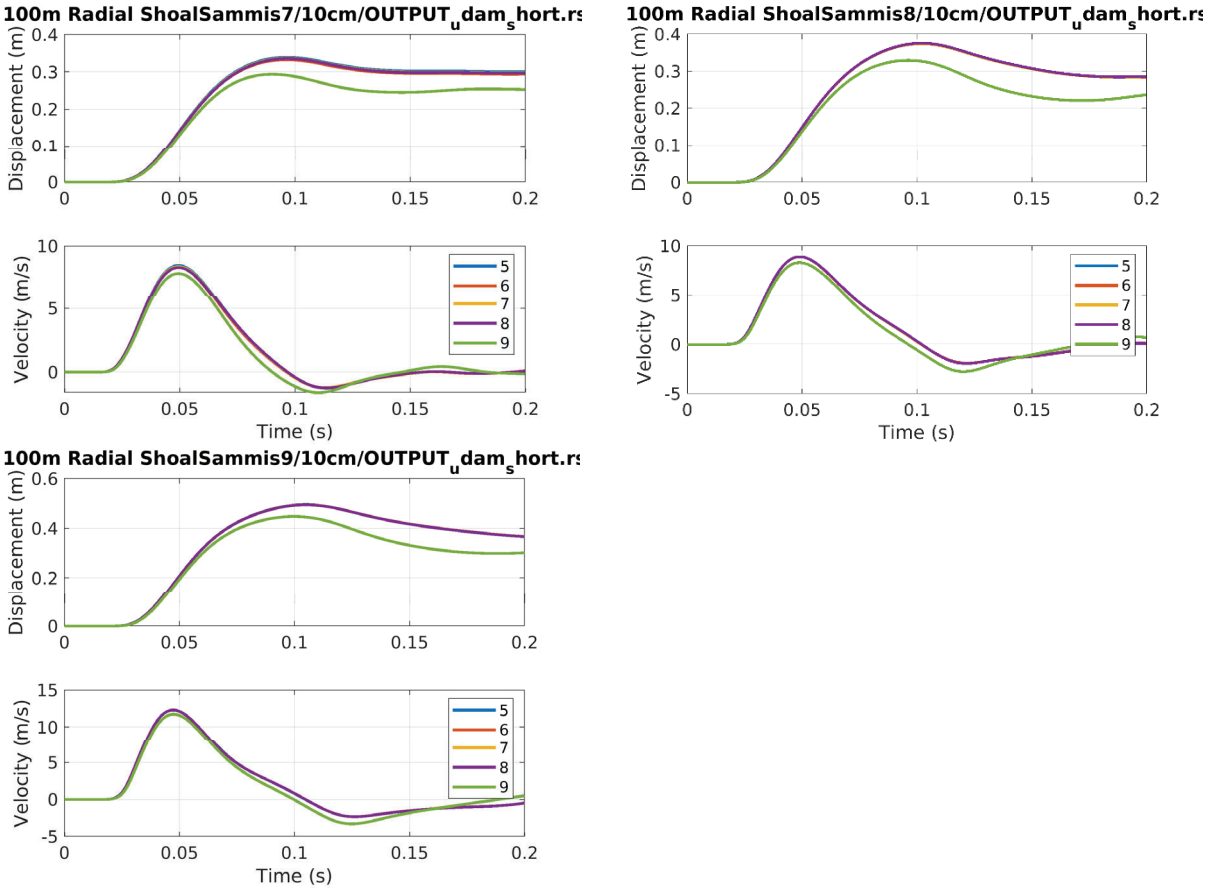

Figure 19 (continued). Radial (outward from source center) waveforms at 5 locations. Locations 5-8 are the four horizontal directions along each axis at source depth. Location 9 is directly below the source. All are at a distance of 100 meters from the source center. Case number is in the title. All waveforms were lowpass filtered at 20 Hz.

We compared waveforms at the distance of the Shoal stations, 590 meters from the source along the X and Y axes for all cases. These were all identical. Three of the cases are shown in Figure 20.

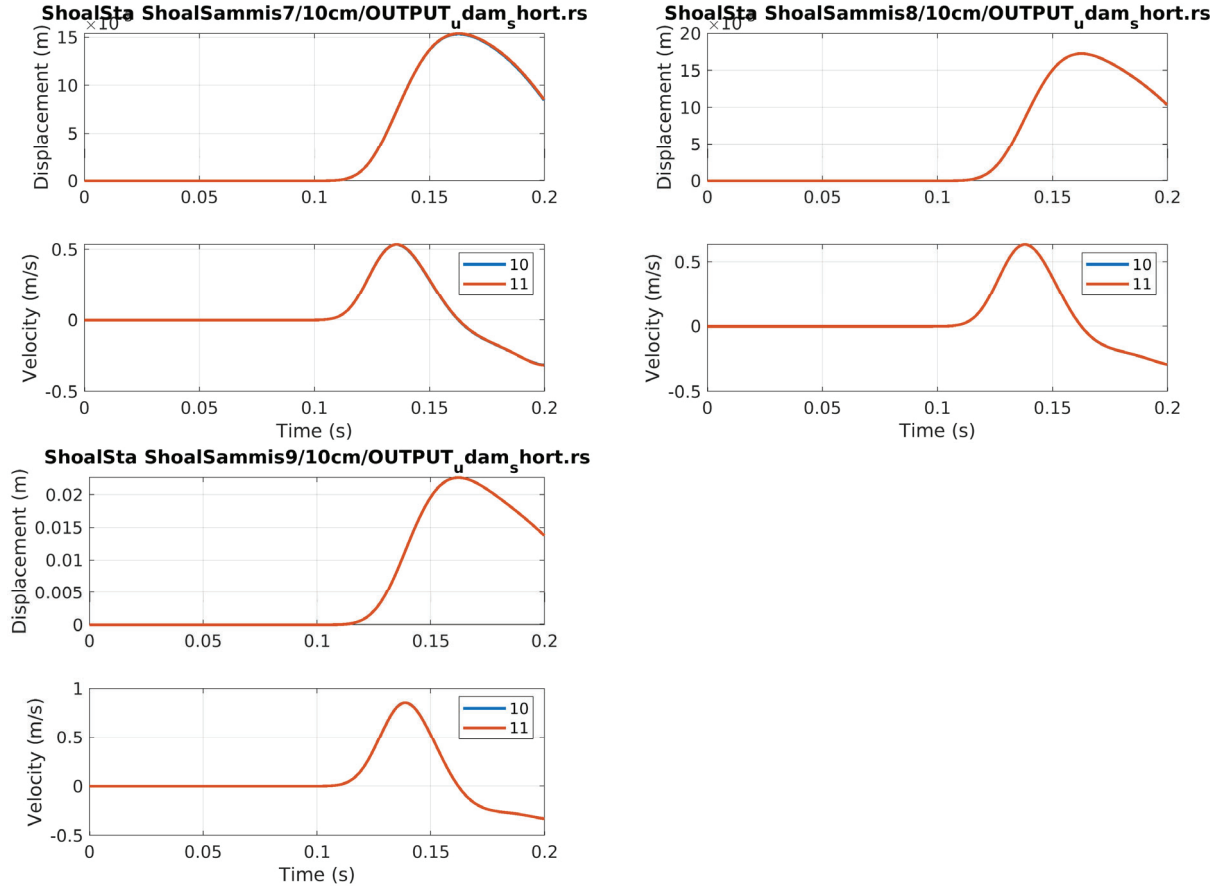

Figure 20. Waveforms in two directions at 590 meters from the source, out to 0.2 seconds, for cases 7, 8 and 9. All lowpass filtered at 20 Hz.

5.2 Selection of Optimum Material Model

We compared the final cavity size and shape for all of the calculations. Some of them, particularly cases 7 and 8, caused highly distorted cavity shapes. These are cases that have strength weakening, but do not allow shear failure before micromechanical failure. Because of this, mixed strong and weak areas can develop near the cavity wall, causing the odd shapes. Case 9, however, which is the same except that shear failure is allowed before cavity failure, does not have this problem. Case 9 is also physically the most reasonable, as shear failure would be expected in the high stress area near the cavity wall. This model differs from the material model used in the Shoal calculation only by including micromechanical damage in addition to plastic failure. In the 1D calculations, Case 9 was also the best match to the Piledriver and Degelen data. For these reasons, we will use Case 9 in our 3D numerical modeling from this point forward.

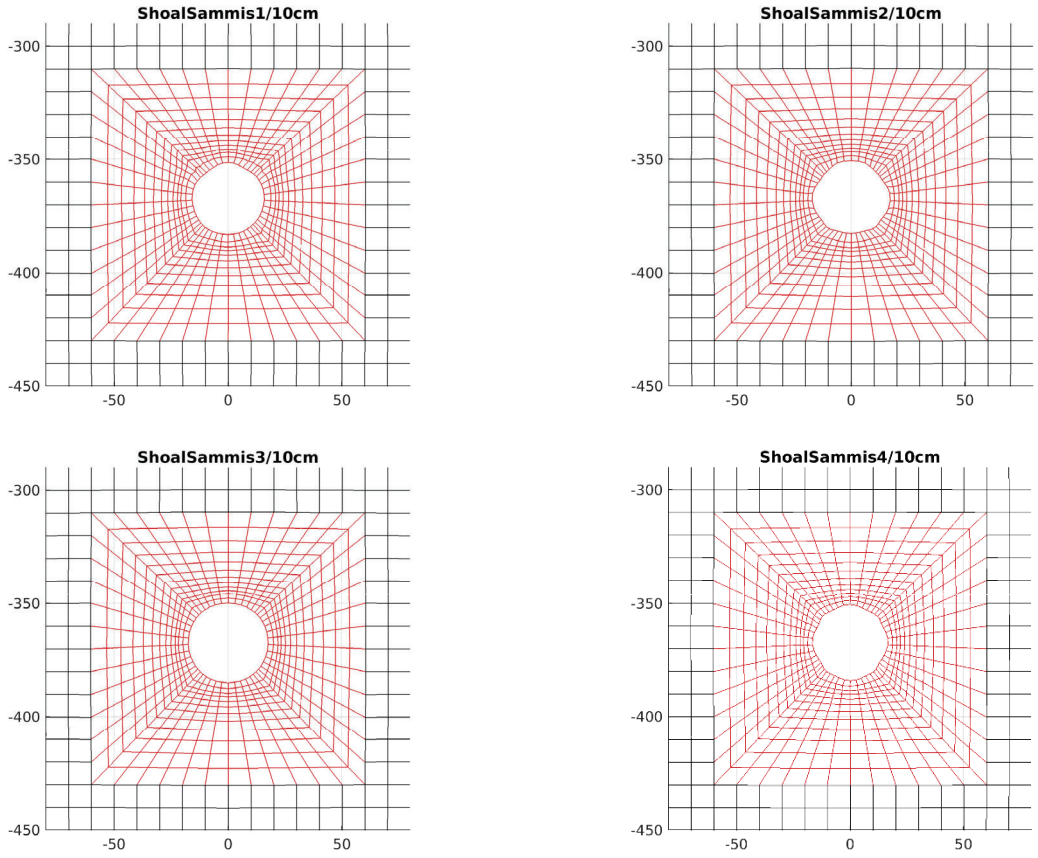

Figure 21. Cavity shape at the end of the calculation for the nine material models.

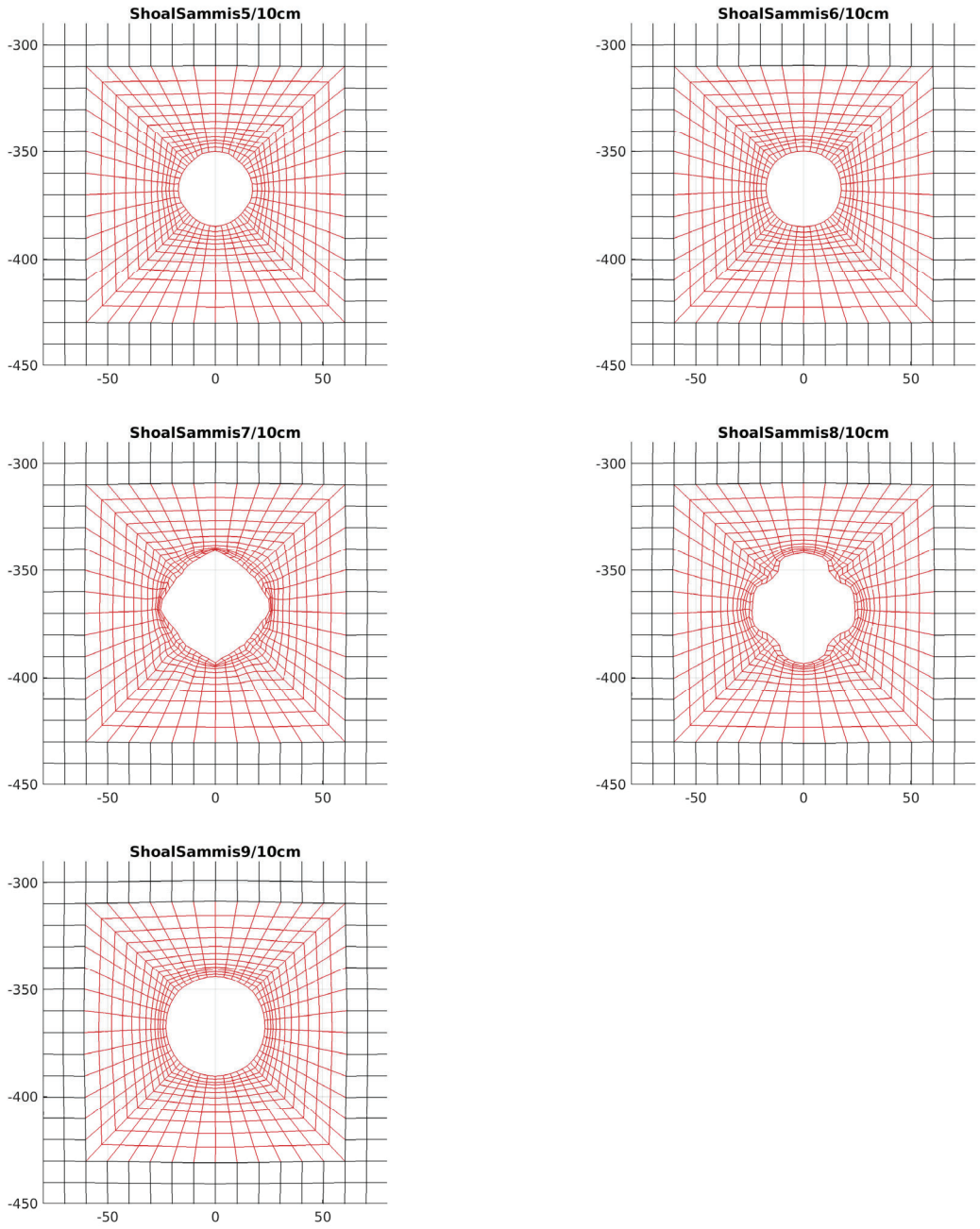

Figure 21 (continued). Cavity shape at the end of the calculation for the nine material models.

We plotted waveforms at several points on the surface for case 9. These are shown in Figure 22. The constant slope in the velocity plots is equal to –g (the acceleration of gravity) and indicates spall.

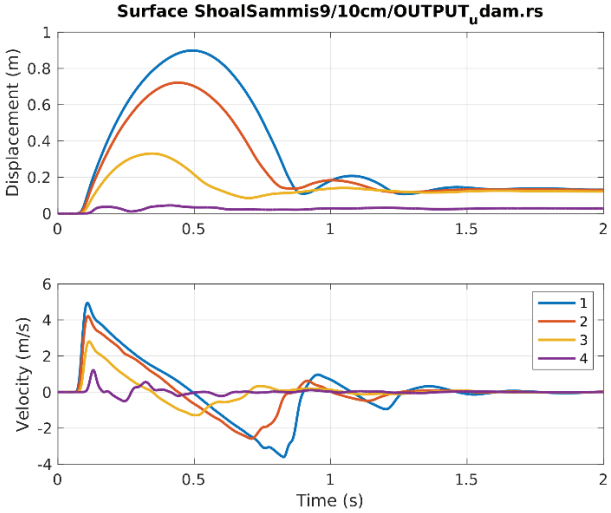

Figure 22. Surface velocity and displacement for case 9. Point 1 is at ground zero on the surface immediately above the explosion. Points 2, 3 and 4 are on the surface 100, 200 and 300 meters from ground zero in the X direction.

Figure 23 shows the evolution of microdamage in material model 9. Note that there is no microdamage for about 50 meters from the explosion center because that region fails by shear failure.

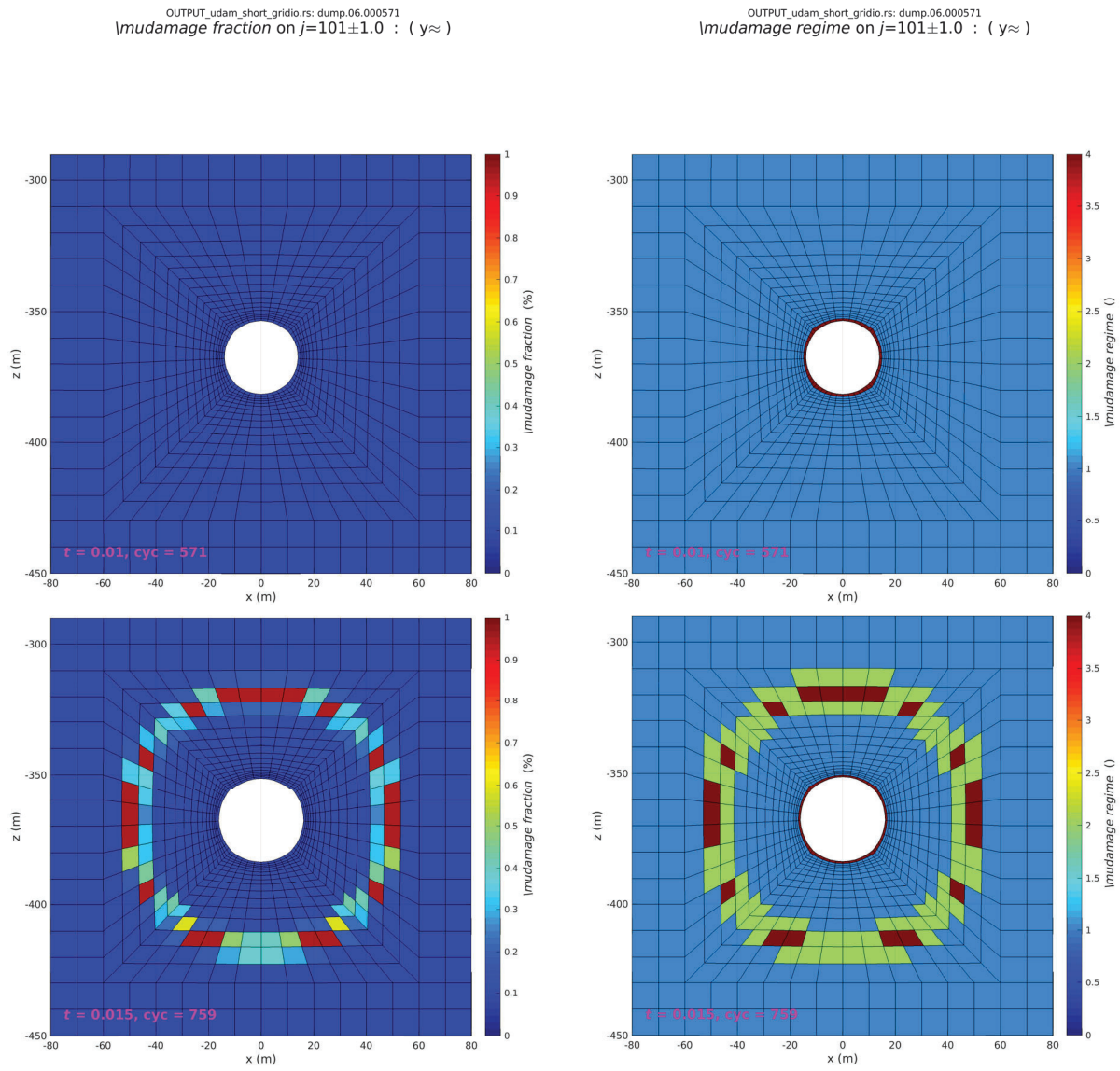

Figure 23. Evolution of microdamage (left) and microdamage regime (right) for case 9. Note that the scale changes in each plot to include the damaged region. From top to bottom, times are 0.01, 0.015, 0.02, 0.05 and 0.1 seconds.

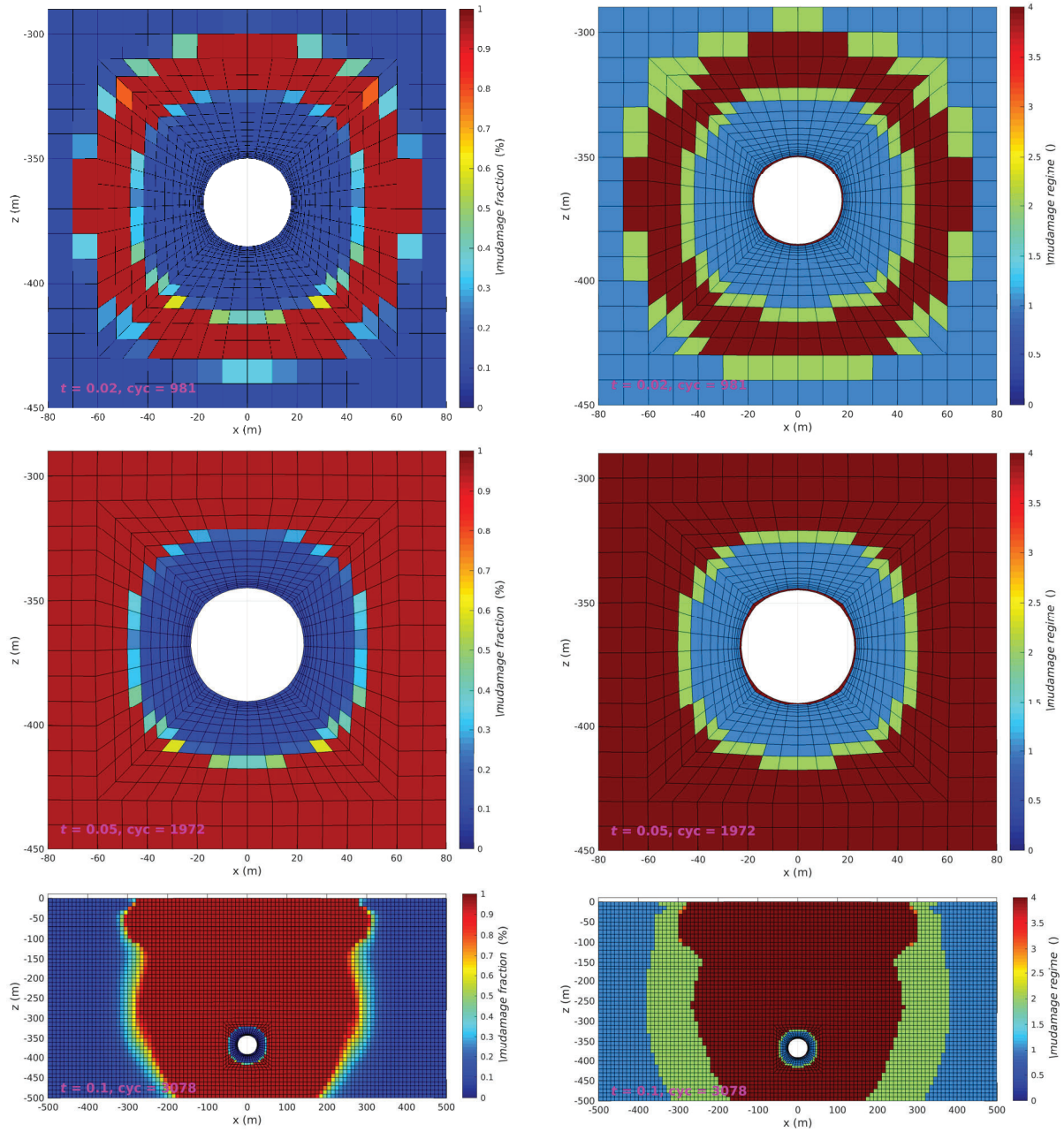

Figure 23 (continued). Evolution of microdamage (left) and microdamage regime (right) for case 9. Note that the scale changes in each plot to include the damaged region. From top to bottom, times are 0.01, 0.015, 0.02, 0.05 and 0.1 seconds.

5.3 The Effect of Microcrack Size

As discussed in Section 3, one of the few free parameters in the microdamage model is the initial microcrack size. This parameter is expected to be scale dependent because the size of the problem limits the size of the largest microcracks. In a laboratory scale experiment, for example, the microcrack size cannot be larger that a centimeter or so, and measurement of microcracks in intact samples have found microcrack sizes in most (intact) materials of one millimeter or less. The region around a typical nuclear explosion test site, however, contains cracked and jointed rock on a scale that may be much larger. It has frequently been observed that the strength of laboratory size rock samples is much larger than the in-situ rock strength around underground explosions. One of the purposes of this study is to understand this size effect. As a first step, we have run variants of the Shoal calculation described in the previous section using material model #9 with microcrack sizes of 1 mm, 1 cm, 10 cm and 1 meter. We compare these also with the original Shoal calculation, which has no microcracks.

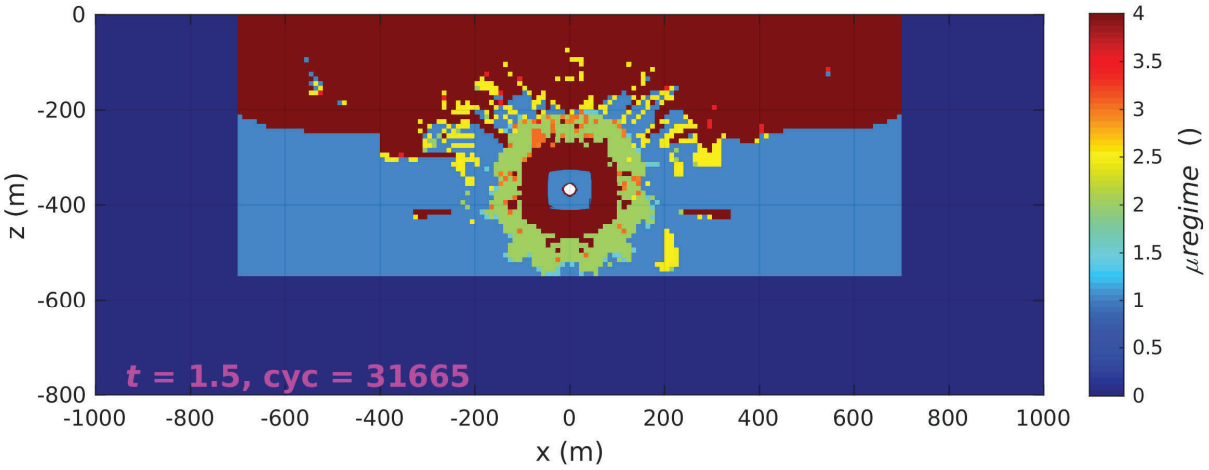

Figure 24. Damage region from Shoal calculation with 1mm microcracks. Damage is cut off in the dark blue region where the regime is shown as zero. Figure is near the end of the calculation at 1.5 seconds.

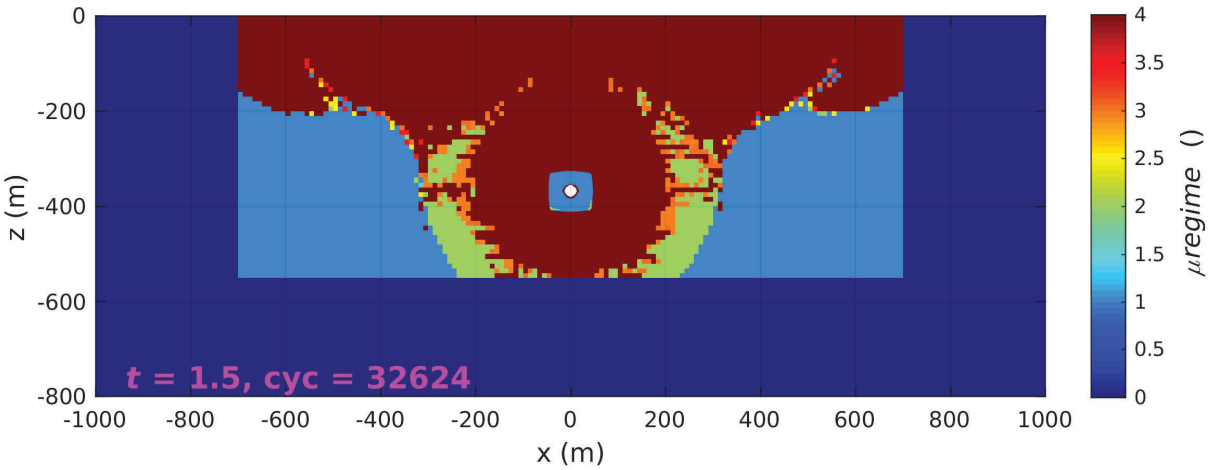

Figure 25. Damage region from Shoal calculation with 1cm microcracks.

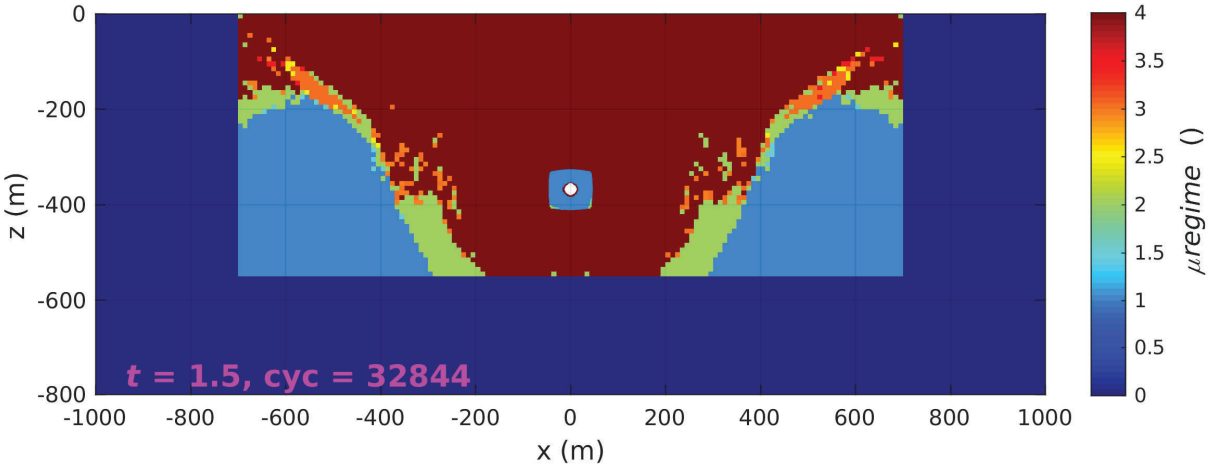

Figure 26. Damage region from Shoal calculation with 10cm microcracks.

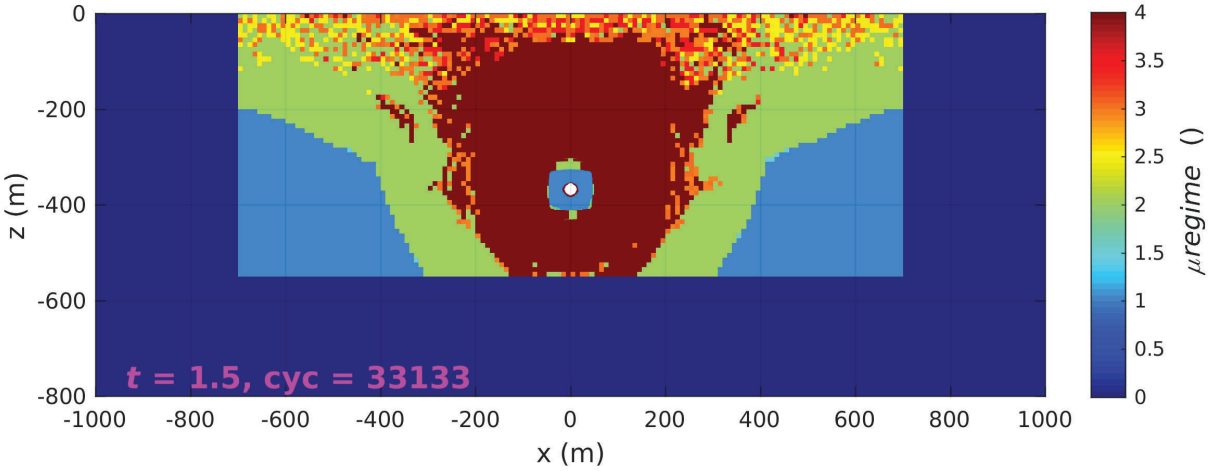

Figure 27. Damage region from Shoal calculation with 1m microcracks.

Figure 24 to Figure 27 show that damage regimes for four initial microcrack sizes. All show extensive microdamage, but with significant differences. In the smaller sizes, from 1 mm to 10 cm, full damage extends all the way to the allowed failure limit. It extends deeper for 1 cm and 10 cm than for 1 mm. For the largest crack size, complete failure does not extend as far out and a large region stays in regime 2, which corresponds to partial damage.

5.4 Body and Surface Waves using the Micromechanical Damage Model

5.4.1 Body and Surface Waves from Shoal

Body waves were calculated for all four of the cases with different initial crack lengths discussed in section 5.3. The far-field P-waves at a 20 degree takeoff angle are shown in Figure 28 for all four cases and with and without tectonic release. There is little difference in the P-wave amplitudes for the four cases with or without tectonic release, but there are differences in the later part of the waveform. The SV-waves at a 20 degree takeoff angle are shown in Figure 29. The SV waves decrease with increasing crack size, and decrease more with the addition of tectonic stresses. Figure 28 through Figure 30 below are all shown at a zero degree takeoff azimuth. Without tectonic release the calculations are axisymmetric so the results are the same at all azimuths, but tectonic stresses break the symmetry.

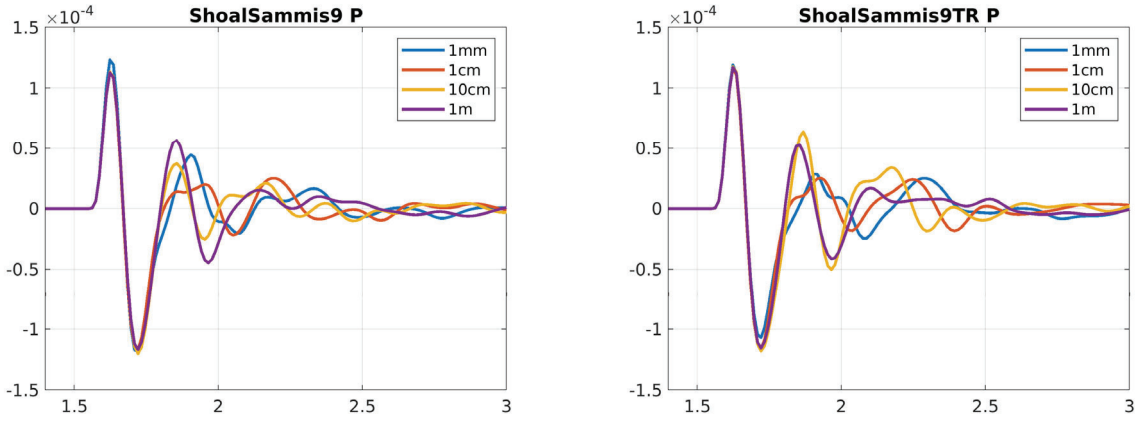

Figure 28. Far-field P-waves low-pass filtered at 5 Hz from four calculations with different microcrack sizes. Left: without tectonic release; right: with tectonic release.

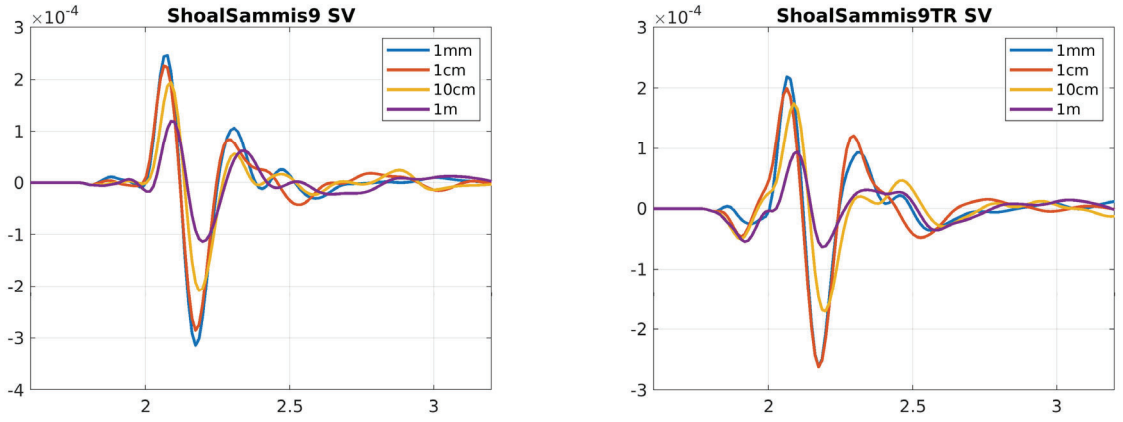

Figure 29. Far-field SV-waves low-pass filtered at 5 Hz from four calculations with different microcrack sizes. Left: without tectonic release; right: with tectonic release.

Surface waves were calculated for all four of the cases with different initial crack lengths discussed in section 5.3, and the four additional cases with compressive tectonic stresses added. The results are shown in Figure 30 and Figure 31. For the Shoal calculations without tectonic stresses,

micromechanical damage decreases Ms, and the decrease is larger with increasing crack size. The effect is amplified with compressive tectonic stresses, and at the largest (1m) size, the surface wave is phase_reversed. Tectonic stresses also cause considerable variation in surface wave amplitude with azimuth as can be seen in Figure 31 and Figure 32.

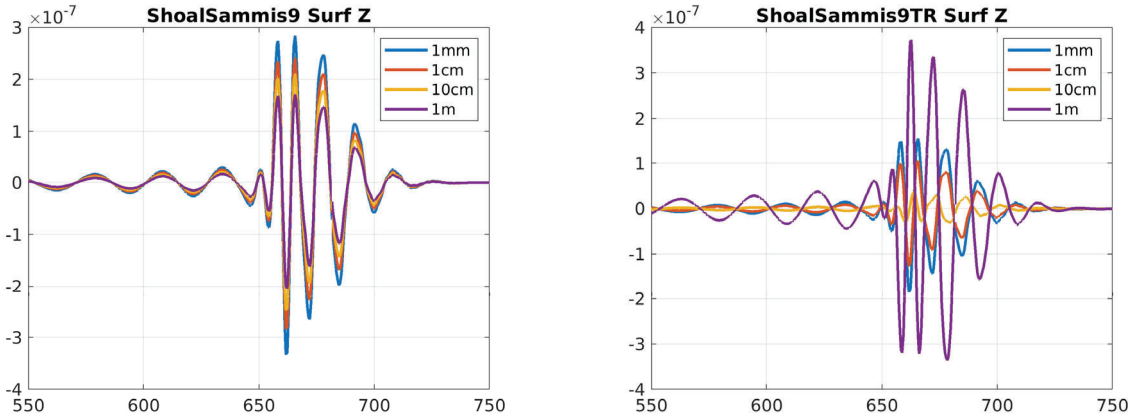

Figure 30. Long period surface waves low-pass filtered at 0.1 Hz from four calculations with different microcrack sizes. Left: without tectonic release; right: with tectonic release. The surface wave from the 1m microcrack calculation with tectonic release is phase-reversed.

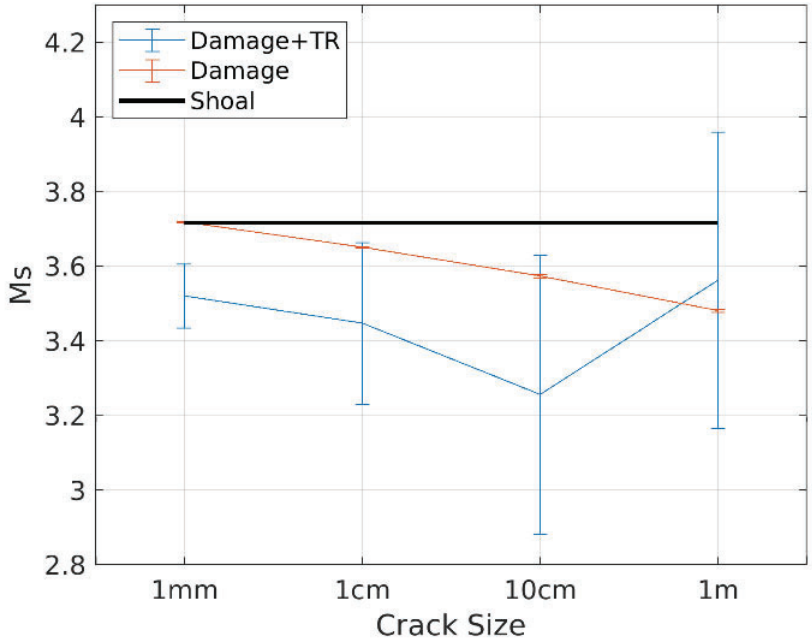

Figure 31. Ms as a function of initial crack size, with and without compressive tectonic release, compared to Shoal. The surface wave from the 1m microcrack calculation with tectonic release is phase-reversed at some azimuths.

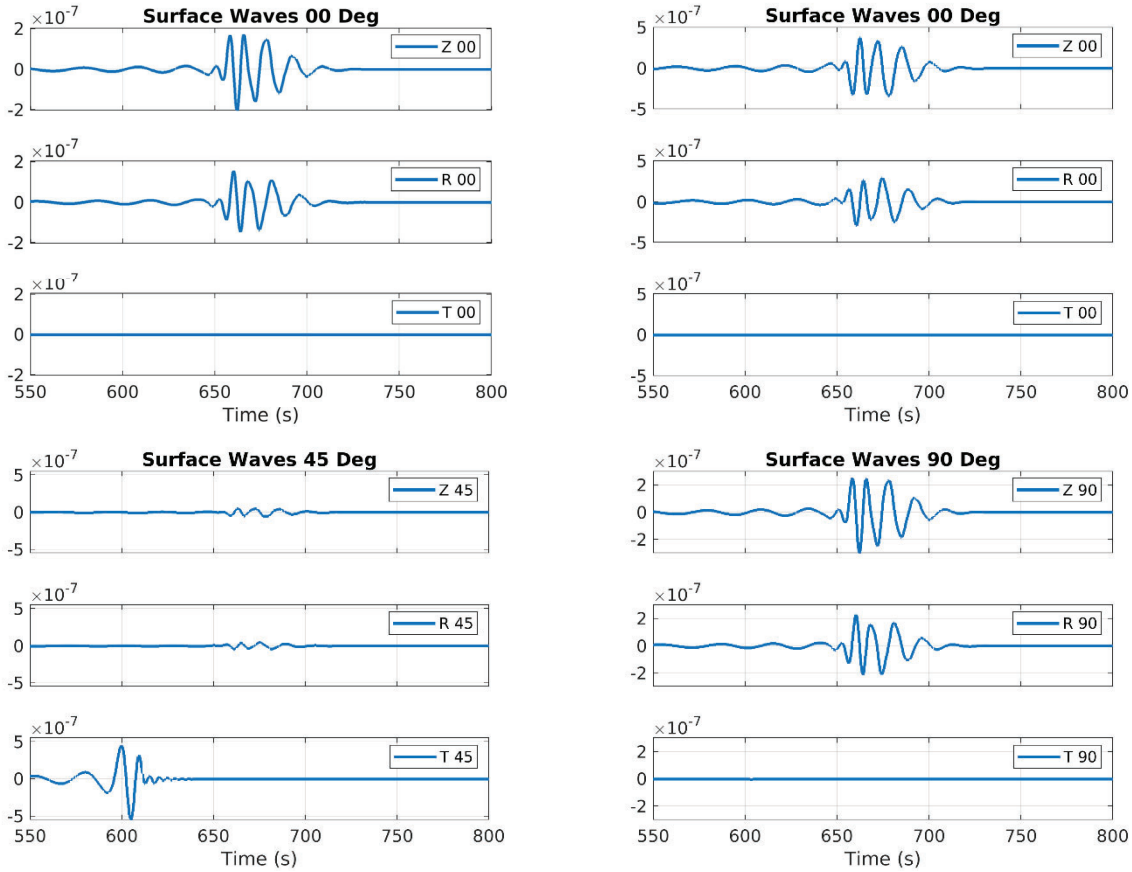

Figure 32. Surface waves with and without compressive tectonic release for 1m microcracks. Compression is in the zero degree azimuth direction. Top left: no tectonic stresses. Other three plots are with tectonic stresses at the angle indicated. At zero degrees the surface wave is both phase reversed and increased in (negative) amplitude. At 45 degrees the Rayleigh waves are reduced in amplitude and there is a large Love wave. At 90 degrees tectonic stresses have little effect on the surface waves.

5.4.2 Body and Surface Waves from Degelen Mountain

Under a previous project[1] we performed a series of calculations of Degelen Mountain explosions. Calculations were performed with and without topography and with and without tectonic stresses. We found that topography alone increased the surface wave amplitudes, while topography with compressive stresses reduced them. The reduced amplitudes were closer to the observations.

We have rerun two of these calculations with the micromechanical damage model included, using a granite model with an initial flaw size of 0.1 m. Figure 33 shows some results from calculation #8, a 78 kiloton explosion in the southern part of the Degelen test site.

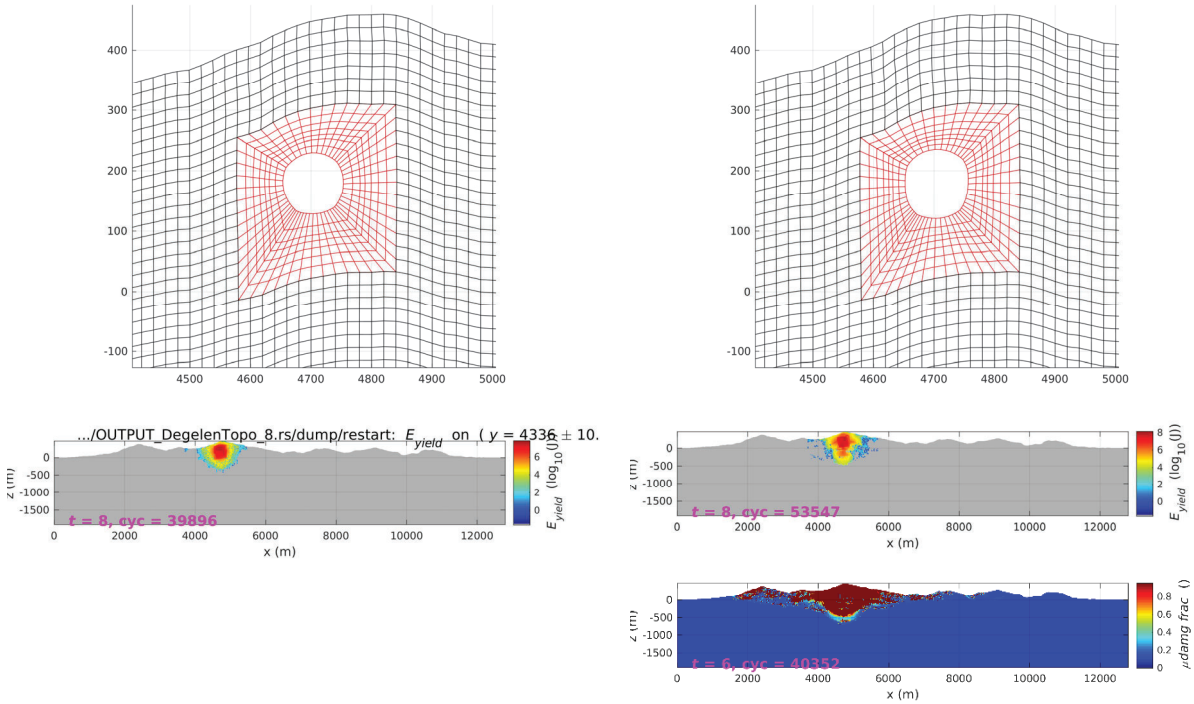

Figure 33. Left: Calculation #8, 78 kt explosion with topography. Right: calculation with microdamage added. Top: final cavity shape; middle: plastic work; bottom: microdamage fraction.

We then used the representation theorem to calculate far field body waves and surface waves. These are shown in Figure 34. The P waves are about the same in both cases, but the SV is larger with the microdamage model. Surface waves are about twice as large with the microdamage model. This is a surprising result, but would happen if the microdamage model is causing more horizontal displacement, perhaps by adding crack volume.

[1] Stevens, J. L., M. O'Brien and J. A. Hanson (2020), "Explosion Depth and Yield Estimation in Mountainous Topography," Leidos Final Report to the Defense Threat Reduction Agency, Leidos-20/0002, August.

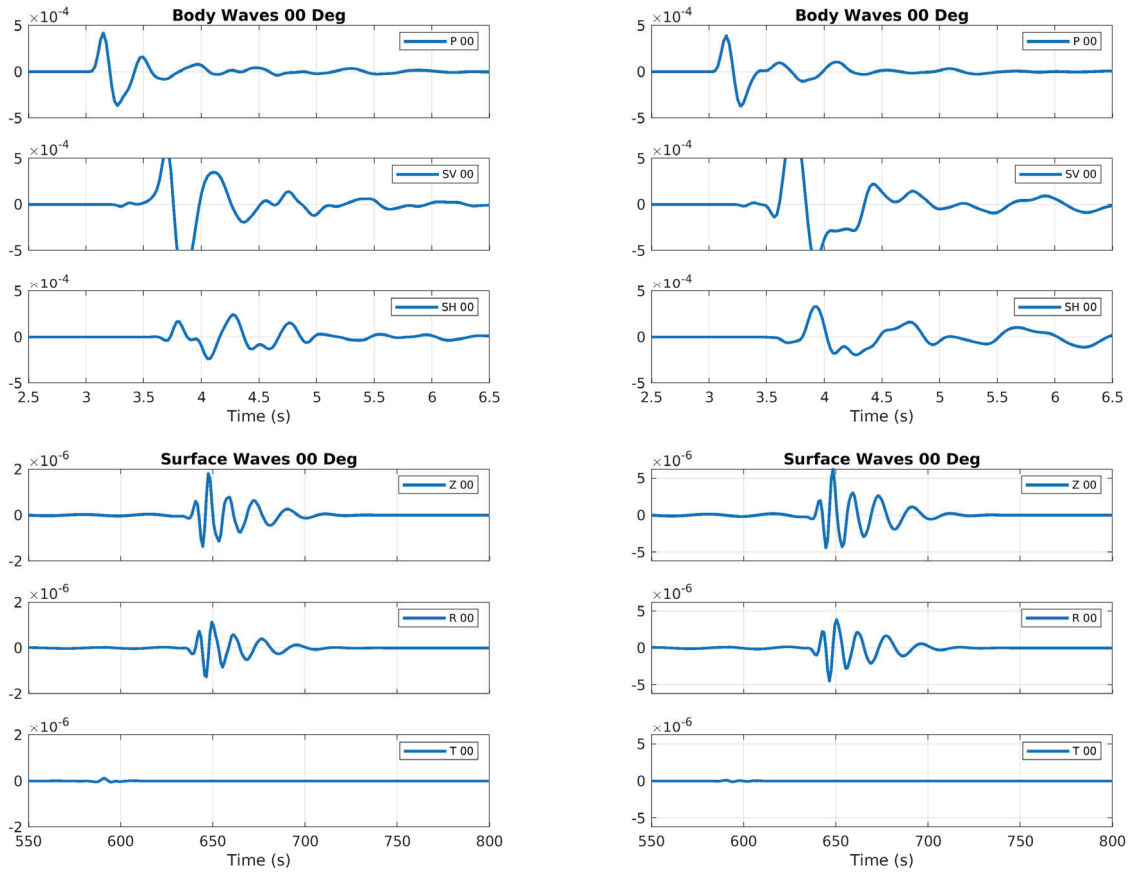

Figure 34. Left: Calculation #8, 78 kt explosion with topography. Right: calculation with microdamage added. Top: P, SV and SH waves at zero degrees (direction of the negative X axis). Bottom: vertical, radial and tangential surface wave components.

In the report referenced above, we also found that calculated surface waves were larger than observed with the topographic model, but that compressive tectonic release, which is expected to be present at Degelen, reduced the surface waves to close to the observed levels. We ran an additional calculation with tectonic release included. The body and surface waves at zero degrees from the calculation are shown in Figure 35. Body waves are affected more than by either effect alone. The amplitude of the P-wave remains about the same, but the shape is changed. Surprisingly, SV is reduced compared to either of the other cases. There is again a clear amplification of the long period surface waves, counteracting the effect of the tectonic stresses and bringing the surface wave amplitude back up to a level comparable to the calculation with topography but without tectonic stresses.

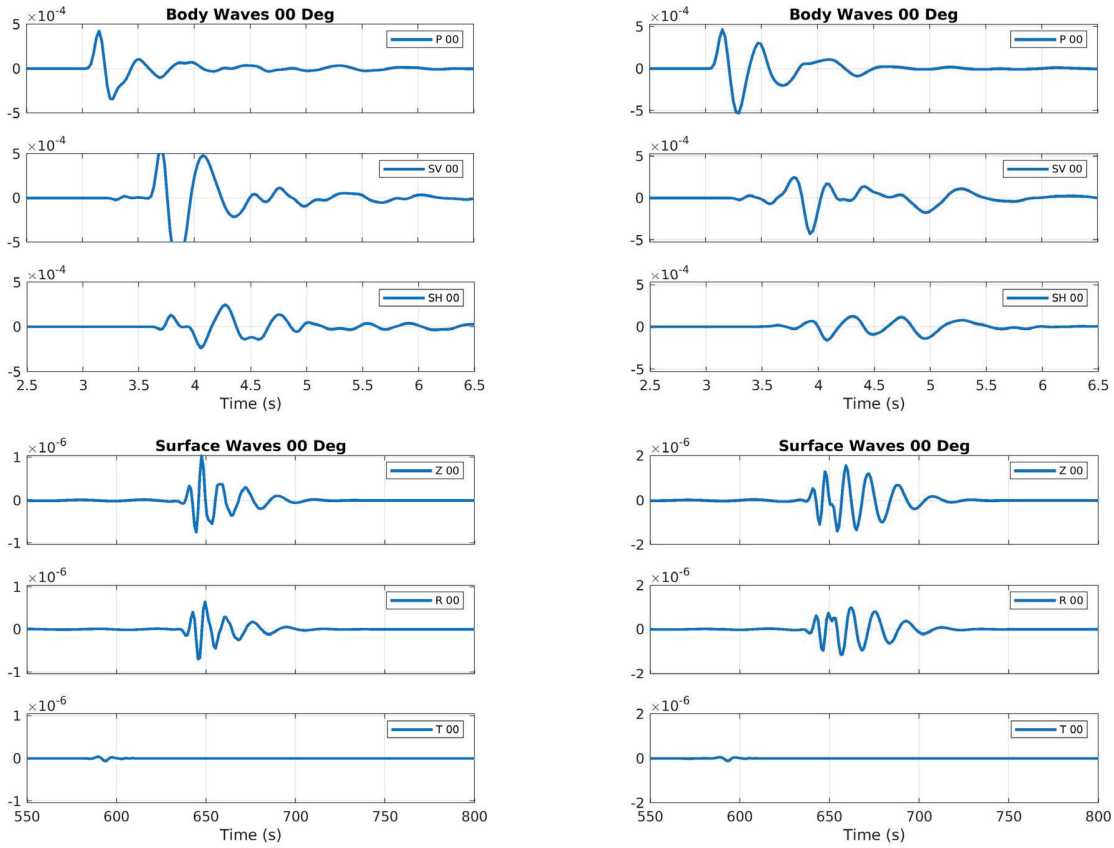

Figure 35. Left: Calculation #8, 78 kt explosion with topography and tectonic stresses. Right: calculation with tectonic stresses and with microdamage added. Top: P, SV and SH waves at zero degrees (direction of the negative X axis). Bottom: vertical, radial and tangential surface wave components.

There are also differences in spectral shape between the calculations as shown in Figure 36. The right hand figures include the micromechanical damage model; the bottom figures include tectonic stresses. The amplification caused by the micromechanical damage model and the reduction due to tectonic stresses is apparent. With both effects included there is a spectral dip near 0.12 Hz, but the frequencies below that are clearly enhanced.

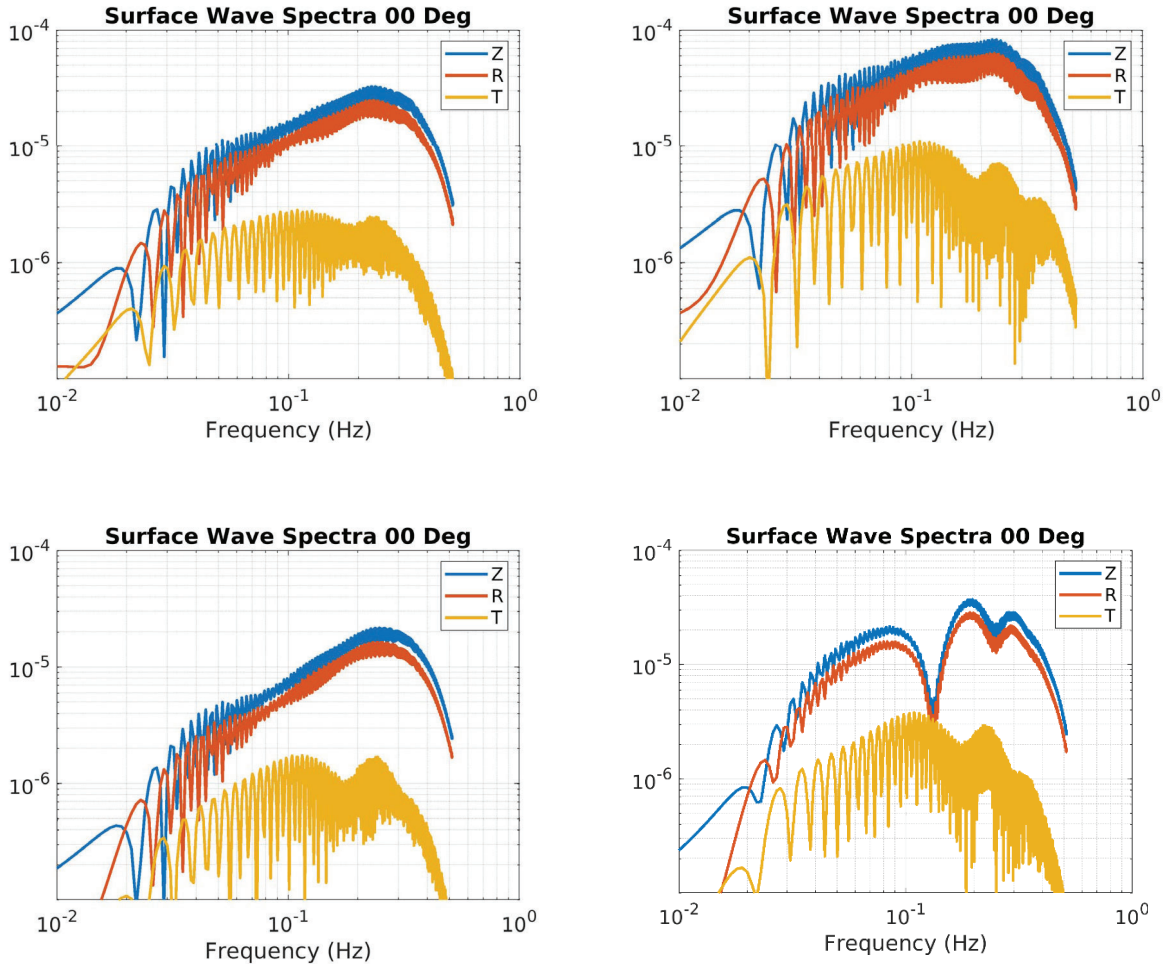

Figure 36. Surface wave spectral amplitudes at zero degrees. Top: topography, no tectonic stresses. Bottom, with compressive tectonic stresses. Left: without micromechanical damage model; Right:with micromechanical damage model.

5.4.3 Body and Surface Waves from the Slope Calculations

Under a previous project[2] we performed calculations for an explosion at two depths below a sloping surface, as shown in Figure 37 and listed in Table 10. We have rerun the calculations adding the micromechanical damage model, with all other parameters kept the same as the Shoal calculation. Calculations were run with initial microcrack size of 1mm, 1cm, 10cm, and 1m.

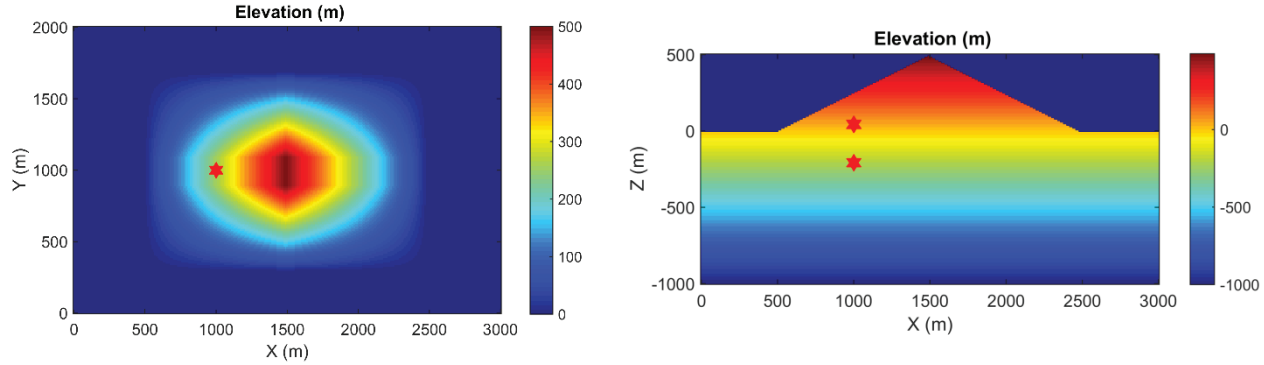

Figure 37. Elevation in map view and cross section for the slope calculation. Mark shows the location of the explosion sources in the Slope calculations.

Table 10. Slope and Shoal calculations.

Name	Surface	Depth Below Surface Vertical/Closest (m)	Explosion Yield (kt)	Scaled Depth m/kt$^{1/3}$	Comments
Shoal	Flat	367 / 367	12.5	158	Baseline case
Slope 1	Sloped	458 / 410	12.5	197 / 177	2:1 slope
Slope 2	Sloped	207 / 185	12.5	89 / 80	2:1 slope

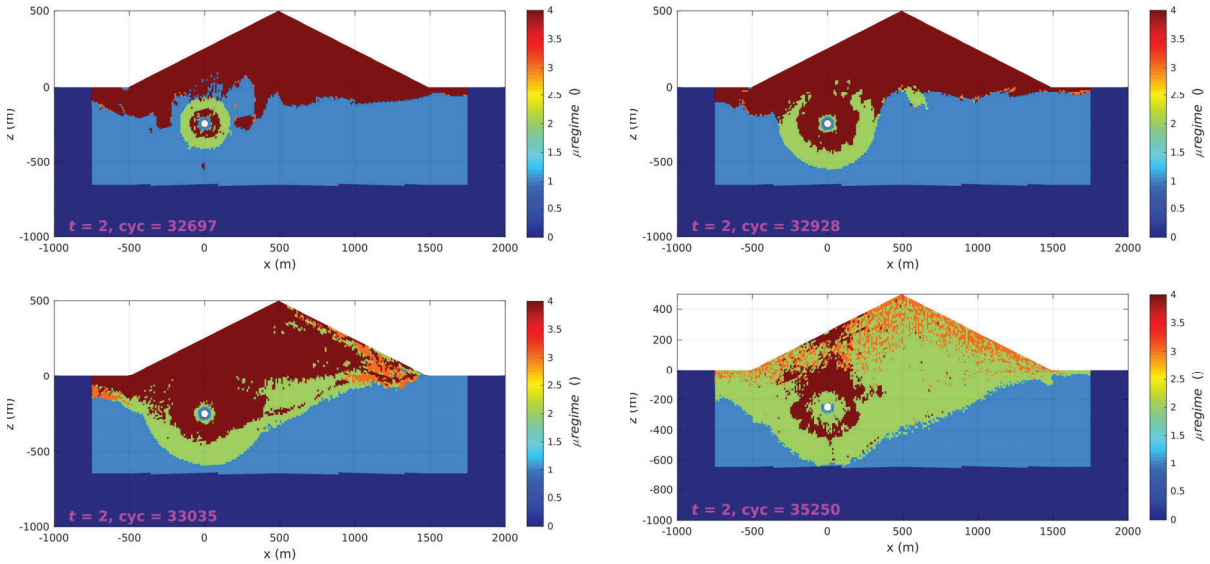

Figure 38. Damaged regions for the Slope1 calculations. Colors show damage regime: light blue is undamaged, green is regime 2, partial damage in compression, orange is regime 3, partial damage in tension, dark red is regime 4, failed. Microdamage is not allowed in dark blue regions. Top left: 1 mm, Top right: 1 cm, lower left: 10 cm; lower right: 1 m, lower left: 10 cm.

[2] Stevens, J. L., M. O'Brien and T. W. Thompson (2017), "Decomposition of the Seismic Source Using Numerical Simulations and Observations of Nuclear Explosions," Leidos final technical report Leidos-17/3002 to Air Force Research Laboratory, May.

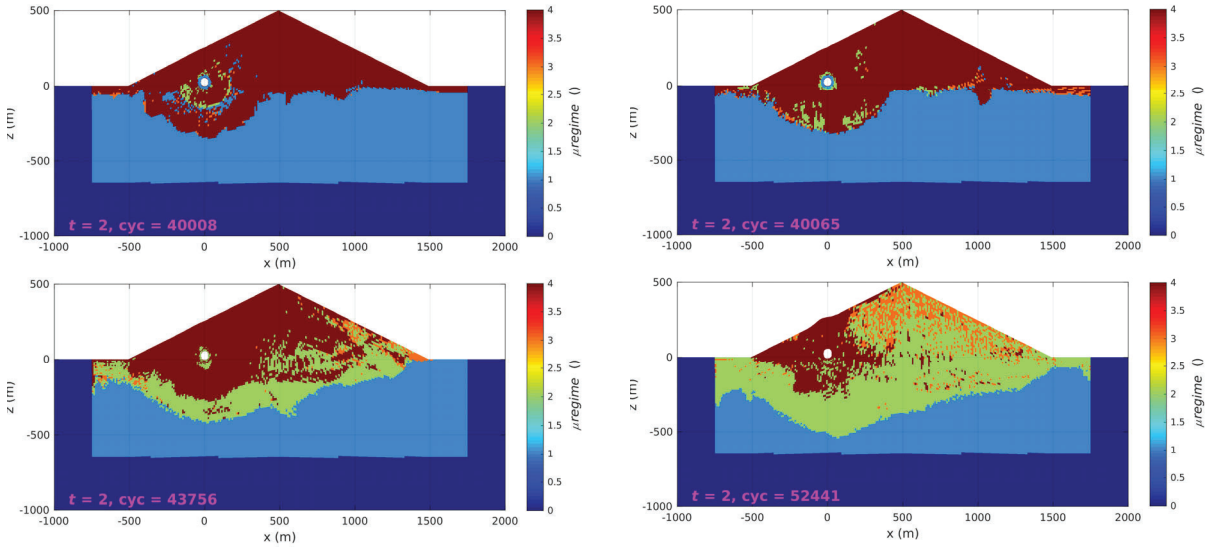

Figure 39. Damaged regions for the Slope2 calculations. Colors show damage regime: light blue is undamaged, green is regime 2, partial damage in compression, orange is regime 3, partial damage in tension, dark red is regime 4, failed. Microdamage is not allowed in dark blue regions. Top left: 1 mm, Top right: 1 cm, lower left: 10 cm; lower right: 1 m, lower left: 10 cm.

Figure 38 and Figure 39 show the damaged regions for Slope 1 and Slope2, respectively. The most obvious difference is that for the larger crack lengths more of the volume is left in a damaged, but not yet failed state. That is because the longer crack lengths take more time to grow with the limitations on crack growth speed discussed earlier.

The regions of plastic yielding and tensile cracking also differ in the calculations as can be seen in Figure 40 and Figure 41.

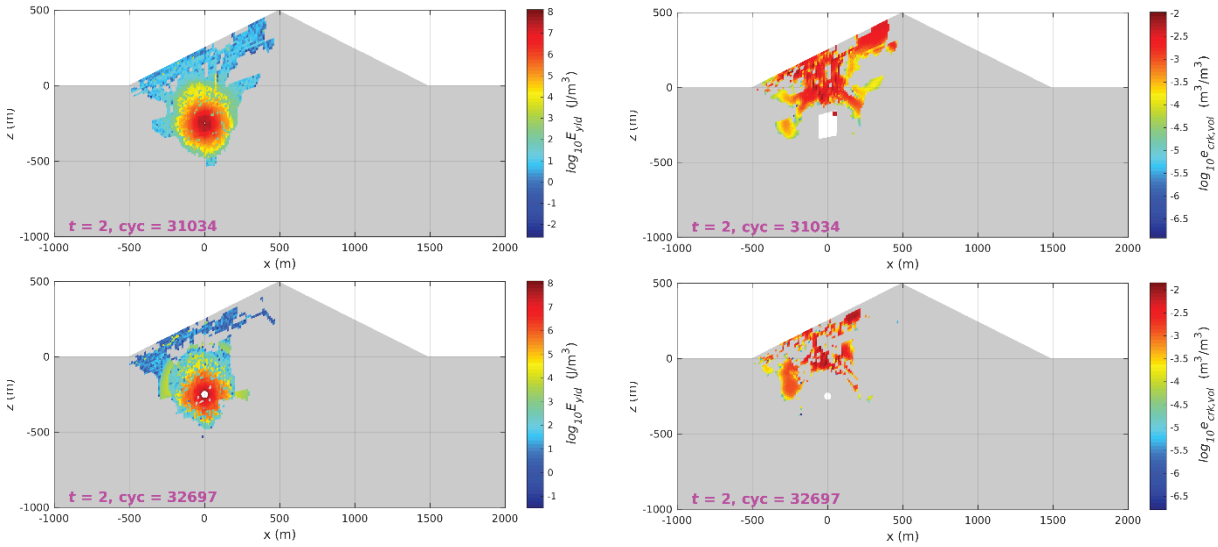

Figure 40. Plastic work (left) and tensile crack strains (right) for the Slope1 calculations. Top: no microdamage; Second: 1 mm, Third: 1 cm, Fourth: 10 cm; lower right: 1 m, Bottom: 10 cm.

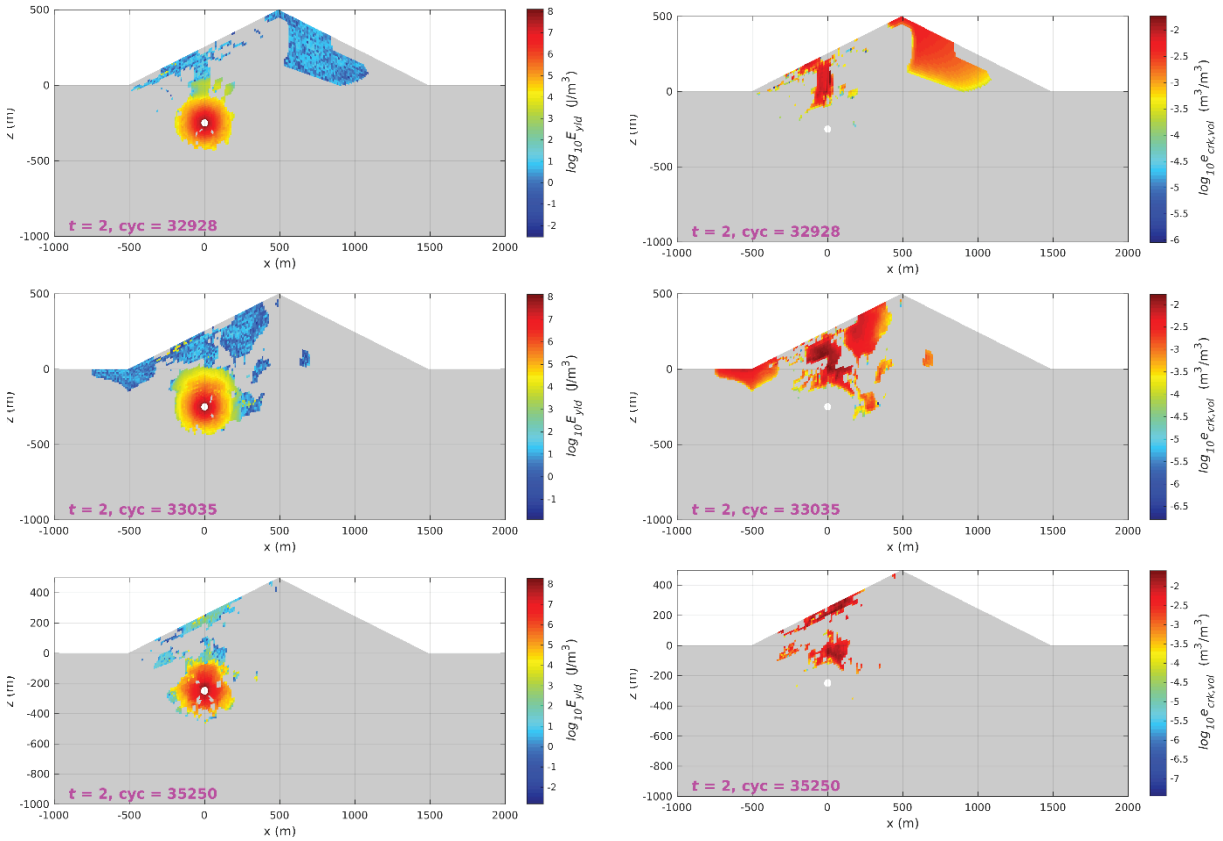

Figure 40 (continued). Plastic work (left) and tensile crack strains (right) for the Slope1 calculations. Top: no microdamage; Second: 1 mm, Third: 1 cm, Fourth: 10 cm; lower right: 1 m, Bottom: 10 cm.

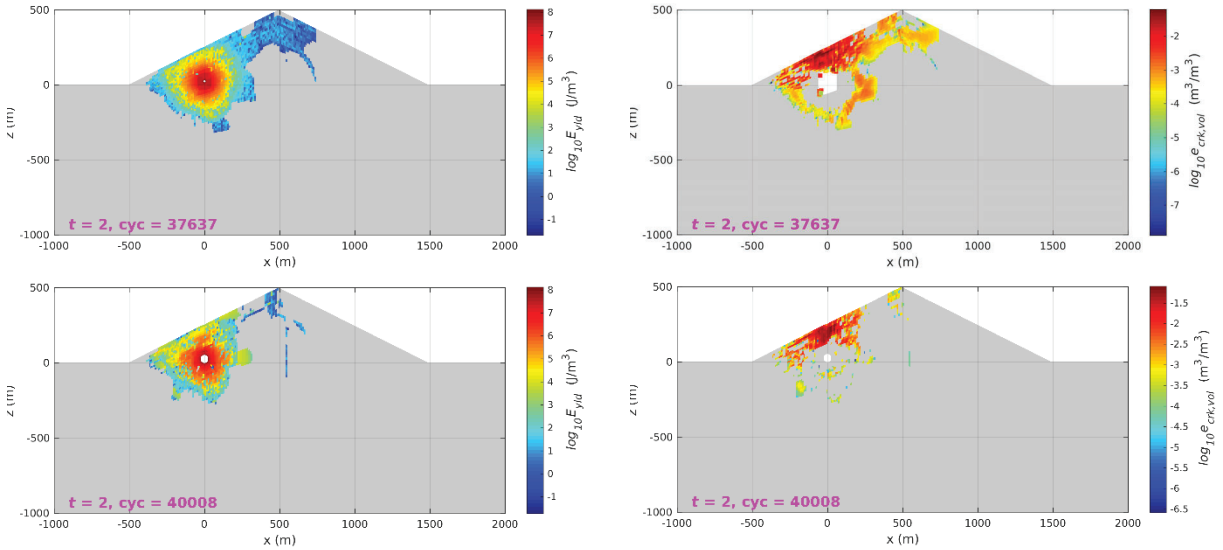

Figure 41. Plastic work (left) and tensile crack strains (right) for the Slope2 calculations. Top: no microdamage; Second: 1 mm, Third: 1 cm, Fourth: 10 cm; lower right: 1 m, Bottom: 10 cm.

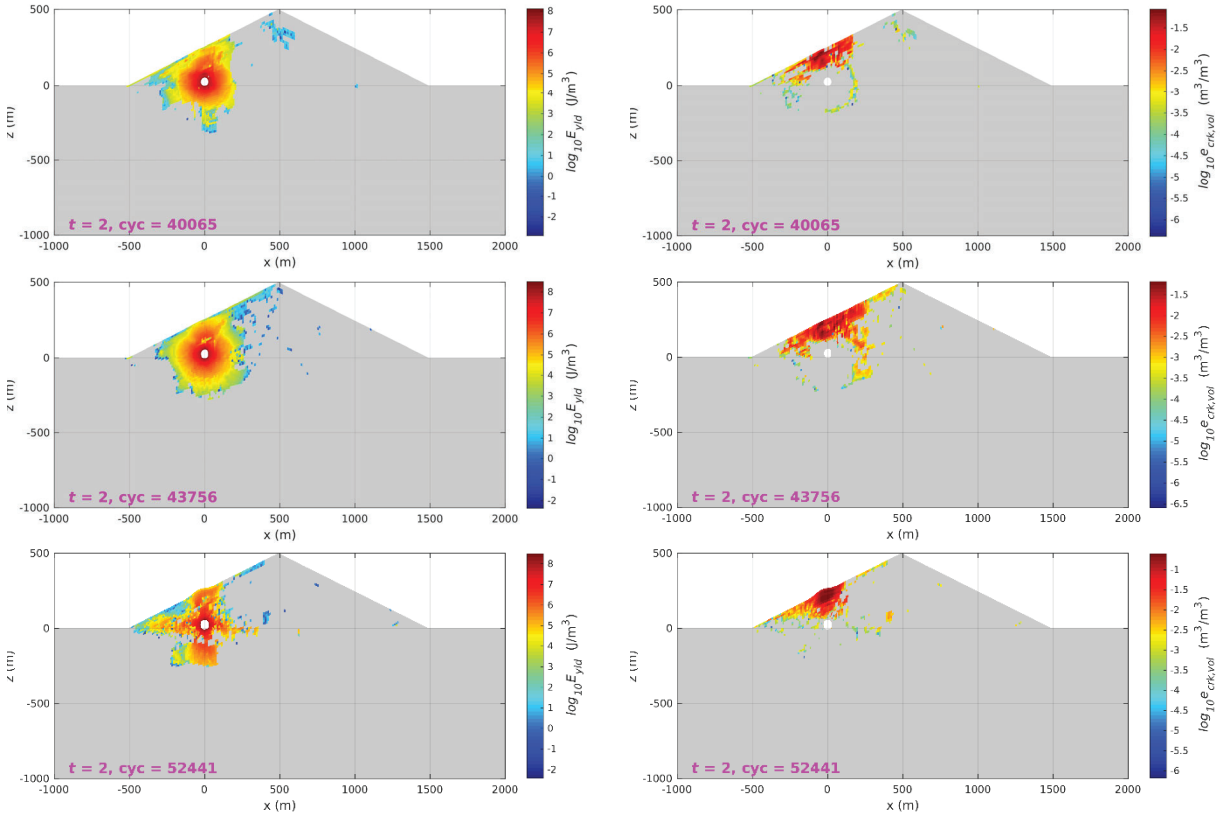

Figure 41 (continued). Plastic work (left) and tensile crack strains (right) for the Slope2 calculations. Top: no microdamage; Second: 1 mm, Third: 1 cm, Fourth: 10 cm; lower right: 1 m, Bottom: 10 cm.

We calculated body and surface waves from all of the calculations. As shown in Figure 42 and Figure 43 there are striking differences with azimuth, particularly for the SV and SH waves. There are smaller differences in the P-waves.

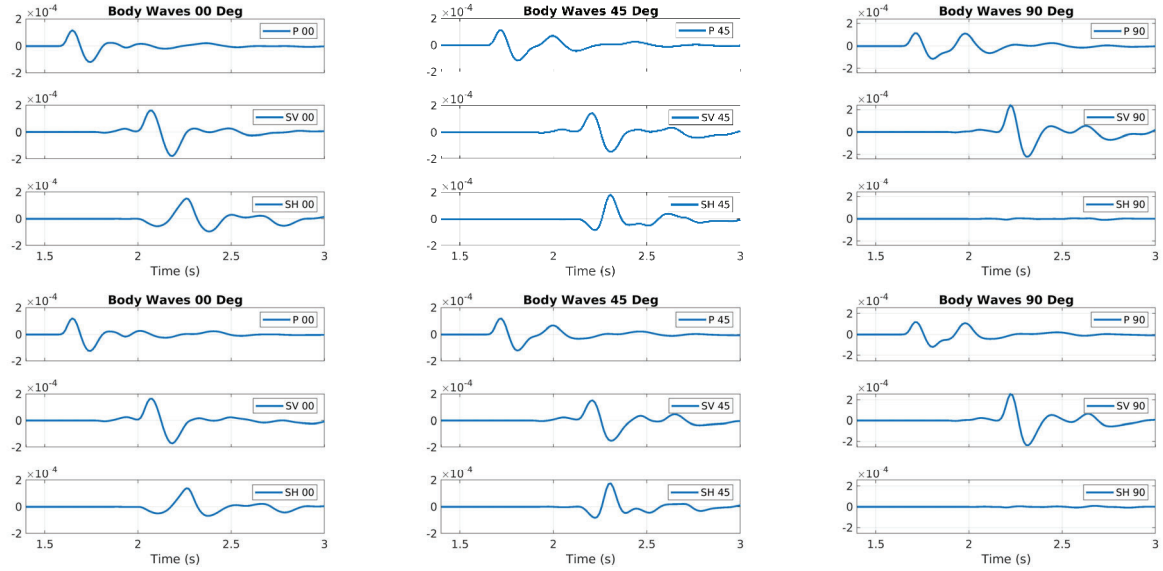

Figure 42. Body waves at three different azimuths for the Slope1 calculations. Top: no microdamage; Second: 1 mm, Third: 1 cm, Fourth: 10 cm; lower right: 1 m, Bottom: 10 cm.

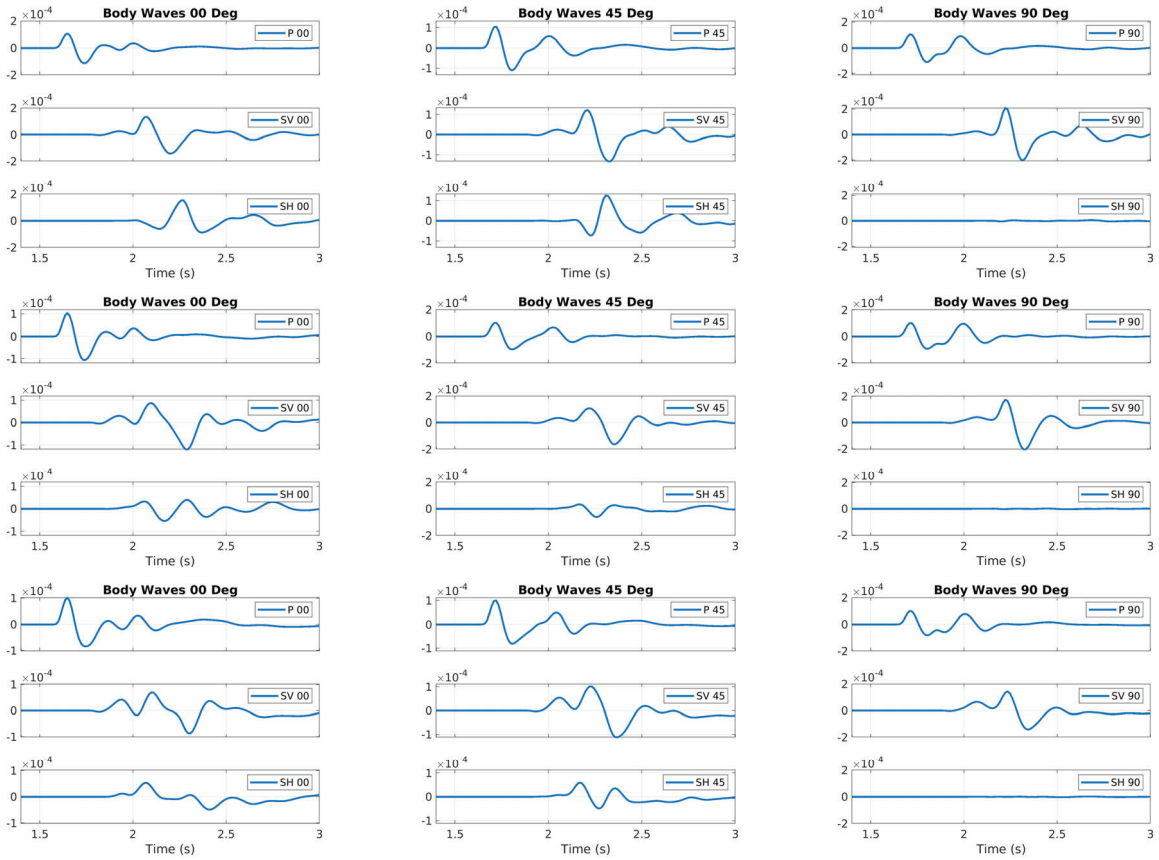

Figure 42 (continued). Body waves at three different azimuths for the Slope1 calculations. Top: no microdamage; Second: 1 mm, Third: 1 cm, Fourth: 10 cm; lower right: 1 m, Bottom: 10 cm.

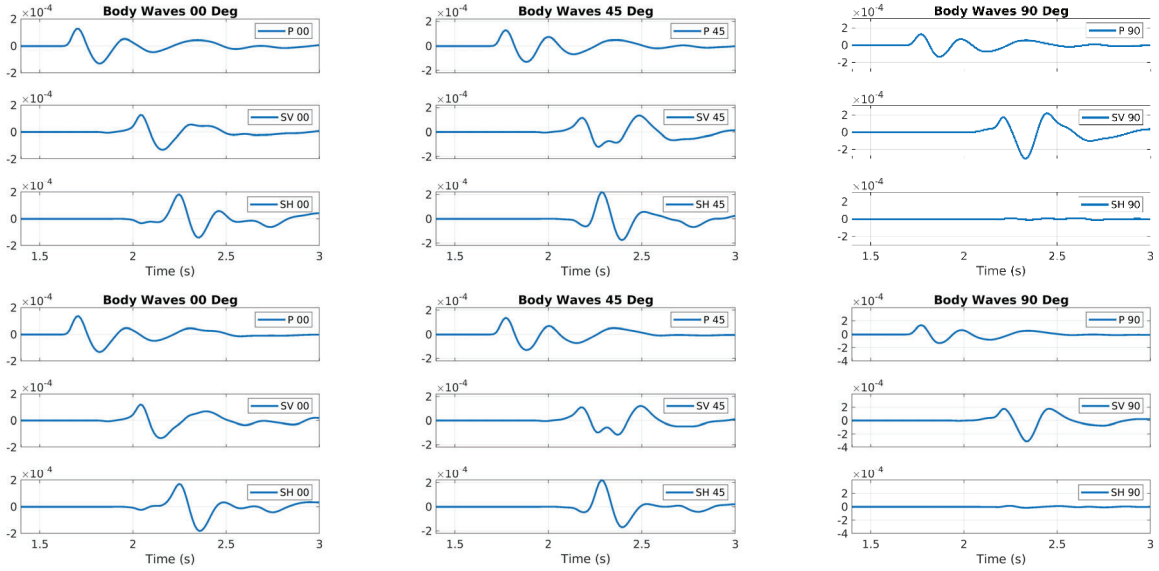

Figure 43. Body waves at three different azimuths for the Slope2 calculations. Top: no microdamage; Second: 1 mm, Third: 1 cm, Fourth: 10 cm; lower right: 1 m, Bottom: 10 cm.

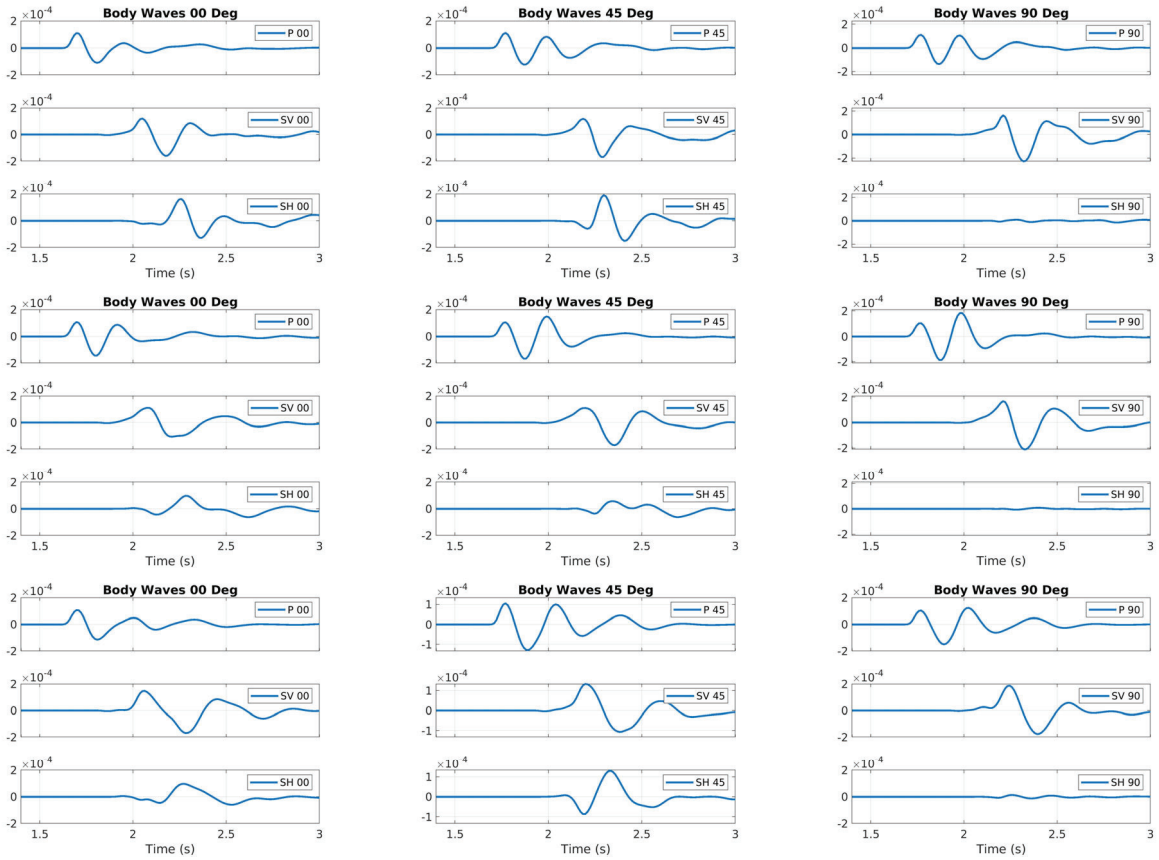

Figure 43 (continued). Body waves at three different azimuths for the Slope2 calculations. Top: no microdamage; Second: 1 mm, Third: 1 cm, Fourth: 10 cm; lower right: 1 m, Bottom: 10 cm.

For surface waves the differences are considerably larger as shown in Figure 44 and Figure 45.

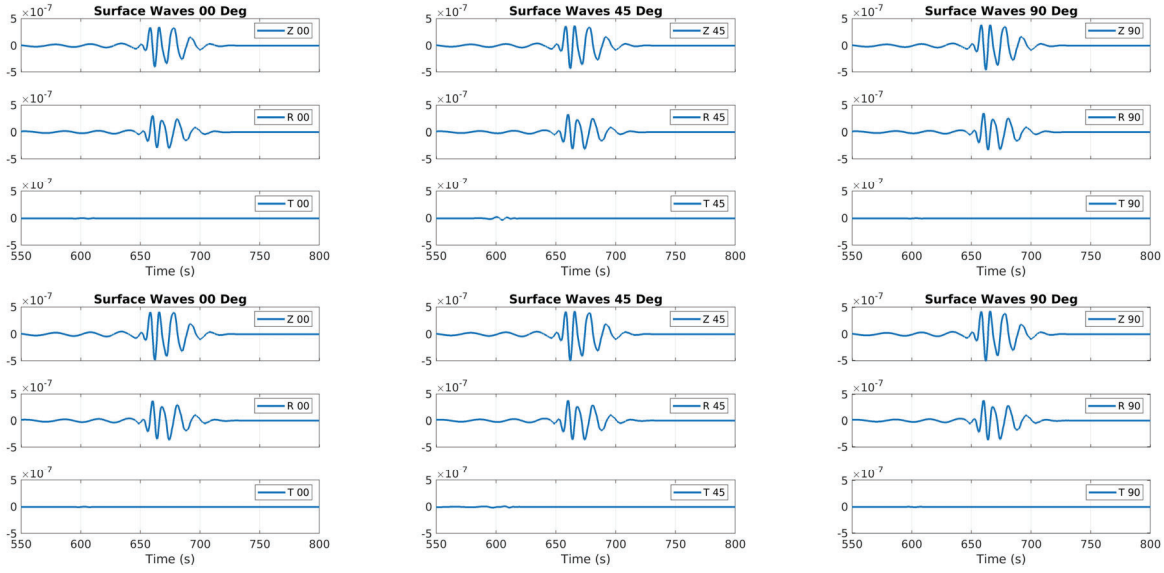

Figure 44. Surface waves at 2000 km distance for three different azimuths for the Slope1 calculations. Top: no microdamage; Second: 1 mm, Third: 1 cm, Fourth: 10 cm; lower right: 1 m, Bottom: 10 cm.

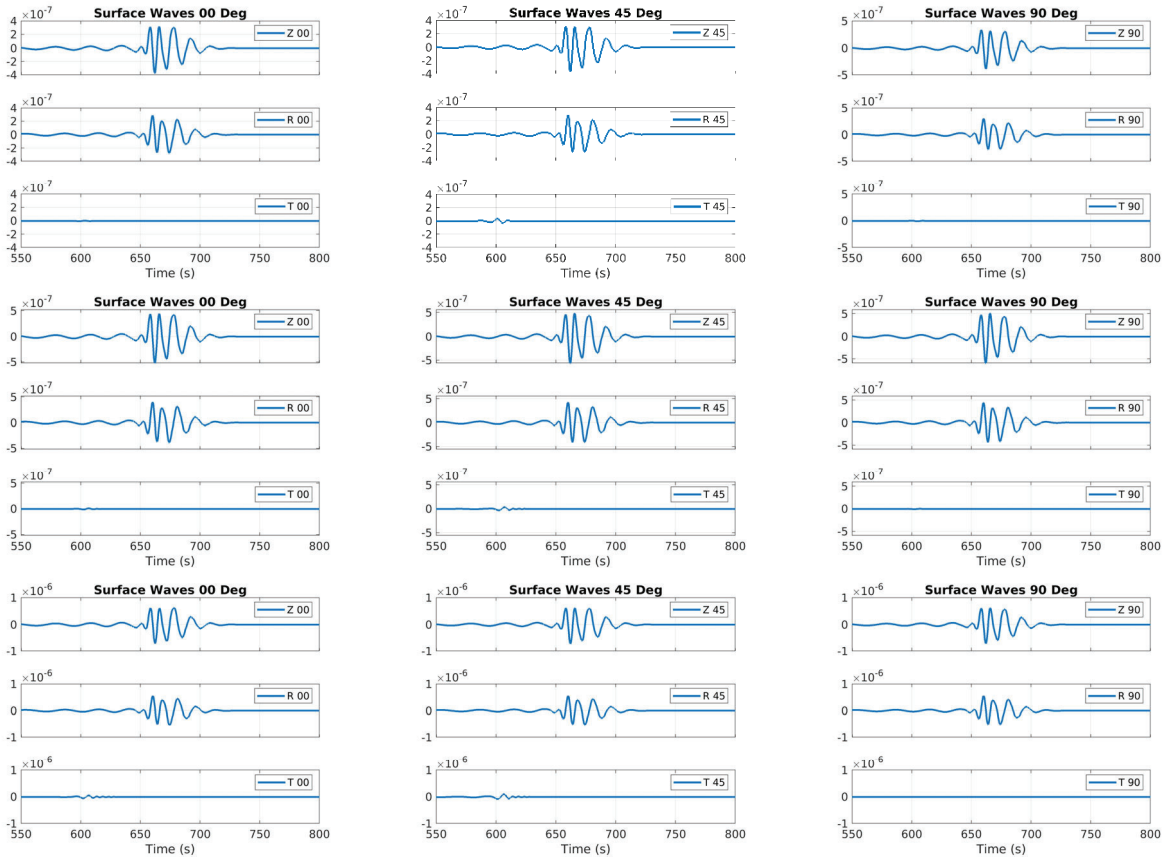

Figure 44 (continued). Surface waves at 2000 km distance for three different azimuths for the Slope1 calculations. Top: no microdamage; Second: 1 mm, Third: 1 cm, Fourth: 10 cm; lower right: 1 m, Bottom: 10 cm.

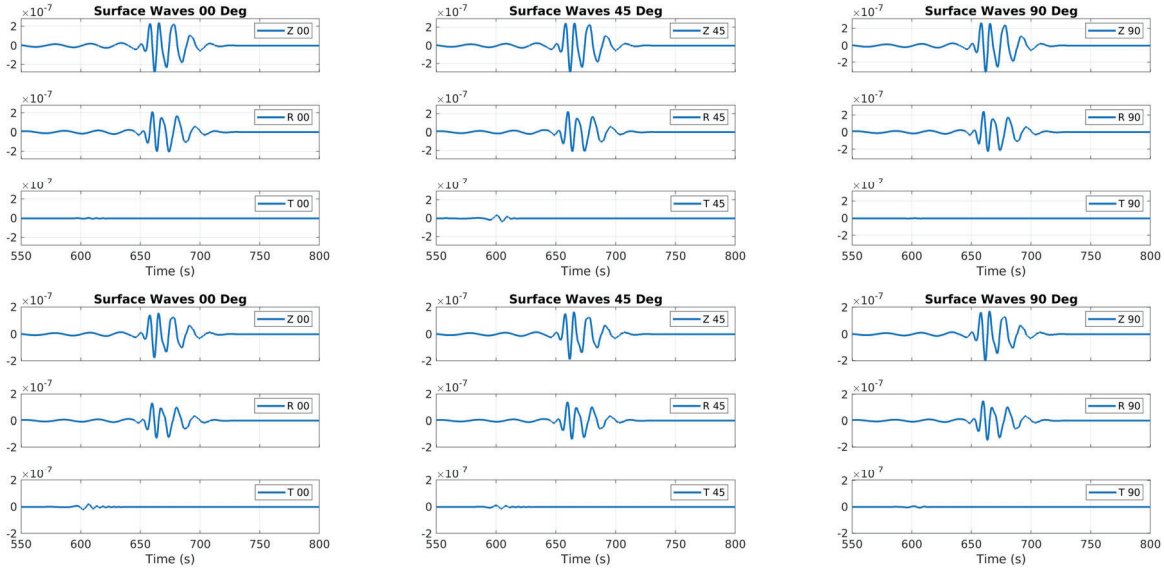

Figure 45. Surface waves at 2000 km distance for three different azimuths for the Slope2 calculations. Top: no microdamage; Second: 1 mm, Third: 1 cm, Fourth: 10 cm; lower right: 1 m, Bottom: 10 cm.

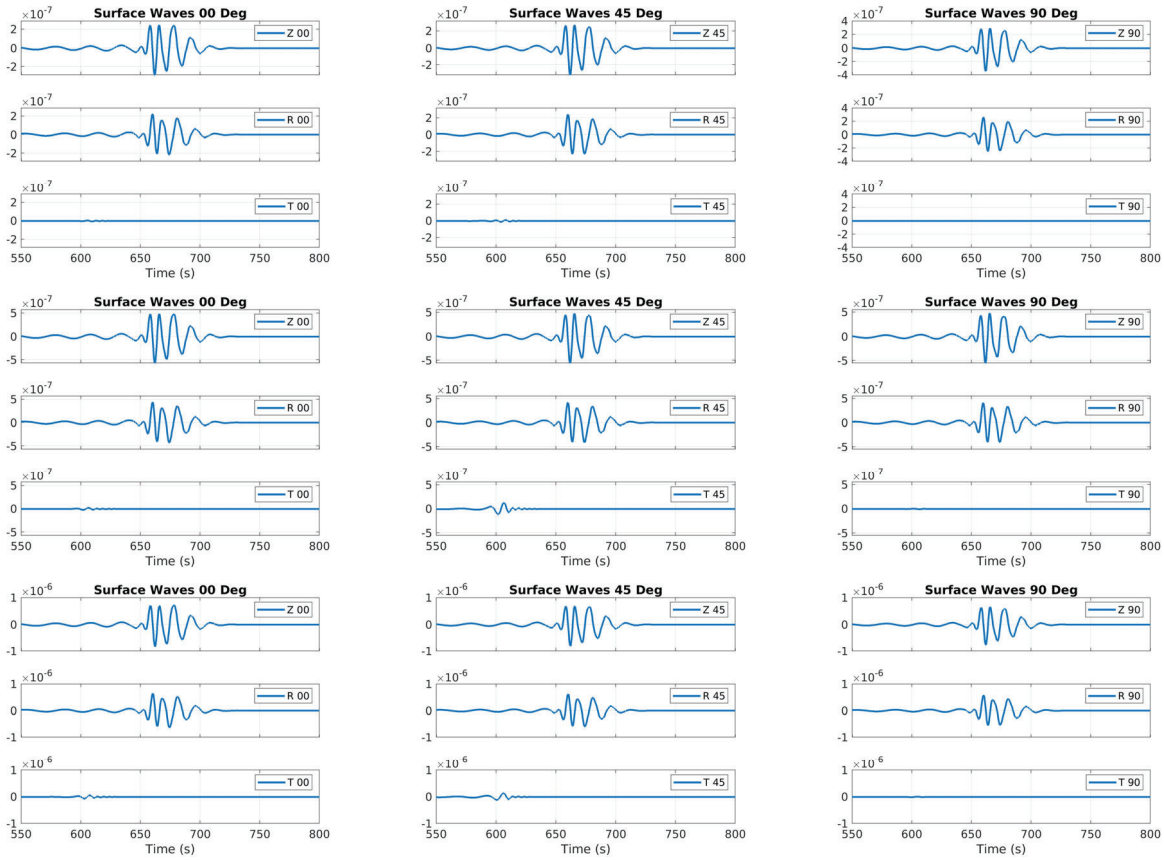

Figure 45 (continued) Surface waves at 2000 km distance for three different azimuths for the Slope2 calculations. Top: no microdamage; Second: 1 mm, Third: 1 cm, Fourth: 10 cm; lower right: 1 m, Bottom: 10 cm.

Figure 46 summarizes the surface wave results. For Slope1, with the explosion below the mountain, Ms is weakly dependent on crack size and is higher that Shoal in all cases. This is consistent with previous results from the Slope and North Korea calculations showing an amplification for explosions near or slightly below the base of a mountain. For Slope 2, increasing crack size causes increasing Ms. This is because the cracks cause increased static horizontal displacement below the mountain.

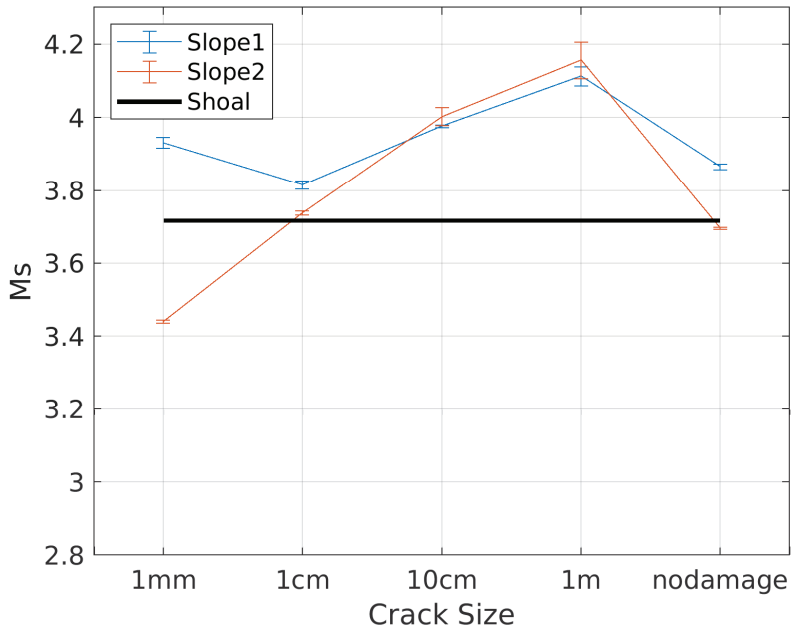

Figure 46. Surface wave amplitudes for Slope1, Slope2 and Shoal as a function of initial crack size. For Slope1, Ms is weakly dependent on crack size and is higher that Shoal in all cases. For Slope 2, increasing crack size causes increasing Ms.

5.5 The effect of micromechanical damage on body and surface waves

The effect of micromechanical damage on body and surface waves is complex, particularly because it interacts with other effect that influence the seismic wave amplitudes. The initial P wave is affected little by micromechanical damage because this is the downgoing wave and most of the damage occurs above the source. The later part of the P-wave can change substantially as can SV and SH waves.

Surface waves are particularly complex. In the Shoal calculations, micromechanical damage reduces Ms because it amplifies the near surface nonlinear effects that causes an inward motion and reduces the static horizontal displacement (Figure 30, Figure 31). The Slope calculations shows that this effect is reduced for an explosion near the base of the mountain. This is because as we have seen before with the Slope calculation and North Korea, the surface effects are reduced when they occur inside a mountain and well above ground level. For the explosion in the mountain, with no microdamage the surface waves are reduced because the explosion deforms the side of the mountain instead of increasing the subsurface horizontal displacement. However, when microdamage is included the subsurface displacement is increased and surface waves are increased in amplitude, particularly for larger initial crack sizes. The Degelen calculations correspond to a more complex topography in which the explosion is within a broader mountain. In this case, the calculations show that surface wave amplitudes are increased. In all cases, compressive tectonic stresses reduce the surface waves and in some cases causes phase reversals, particularly for the flat structure.

REFERENCES

Ashby, M. F. and C. G. Sammis (1990), "The Damage Mechanics of Brittle Solids in Compression," Pure Appl. Geophys., 133(3), pp. 489-521.

Beers, R. F. (1964), "Project Shoal: Analysis of Shoal Data on Ground Motion and Containment," Technical Report to the Advanced Research Projects Agency of the Department of Defense and the U.S. Atomic Energy Commission, December.

Bhat, H. S., A. J. Rosakis, and C. G. Sammis (2012), "A micromechanics based constitutivemodel for brittle failure at high strain rates," J. Appl. Mech., 79(3), 031016, doi:10.1115/1.4005897.

Deshpande, V. S. and Evans, A. G. (2008), "Inelastic Deformation and Energy Dissipation in Ceramics: A Mechanism-Based Constitutive Model," J. Mech. Phys. Solids, 56(10), pp. 3077-3100.

Maenchen, G. and S. Sack (1964), "The TENSOR code," in Methods in Computational Physics 3, Academic Press, New York, NY.

Peyton, S. (1983), "A new representation for the failure surface of granular materials," S-Cubed Technical Report SSS-R-83-6051 submitted to DNA SPSS, March.

Rimer, N., J. L. Stevens, and S. M. Day (1987), "Effects of pore pressure, fractures, and dilatancy on ground motion in granite," S-CUBED final report submitted to Air Force Geophysics Laboratory, AFGL-TR-87-0136, SSS-R-87-8670, April.

Rimer, N., K. Lie, J. L. Stevens, J. R. Murphy, and G. G. Kocharyan (1998), "A micro-mechanical damage model for estimating seismic source characteristics of underground explosions in hardrock," Maxwell Technologies Technical Report submitted to Defense Special Weapons Agency, MFD-DTR-98-15985, January.

Rimer, N., J. L. Stevens, J. R. Murphy, and G. G. Kocharyan (1999), "Estimating Seismic Source Characteristics of Explosions in Hardrock Using a Micro-Mechanical Damage Model," Maxwell Technologies Final Report MTSD-DTR-99-16423, July.

Stevens, J. L., N. Rimer, and S. M. Day (1986), "Constraints on modeling of underground explosions in granite," S-CUBED annual report no. 1 to Air Force Geophysics Laboratory, AFGL-TR-86-0264, SSS-R-87-8312, October.

Stevens, J. L., N. Rimer, H. Xu, G. G. Kocharyan, B. Ivanov, and S. M. Day (2001), "Near Field and Regional Modeling of Explosions at the Degelen Test Site," SAIC Annual Report No. 1 submitted to the Defense Threat Reduction Agency, SAIC-01/1039, June.

Stevens, J. L., N. Rimer, H. Xu, G. E. Baker, G. G. Kocharyan, B. Ivanov, and S. M. Day (2002), "Near Field and Regional Modeling of Explosions at the Degelen Test Site," SAIC Annual Report No. 2 submitted to the Defense Threat Reduction Agency, SAIC-02/2019, June.

Stevens, J. L., N. Rimer, H. Xu, G. E. Baker, and S. M. Day (2003), "Near field and regional modeling of explosions at the Degelen Test Site," SAIC final report to DTRA, DTRA-TR-03-3, SAIC-02/2050, January.

Stevens, J. L. and T. W. Thompson (2015), "3D Numerical Modeling of Tectonic Strain Release from Explosions," Bull. Seism. Soc. Am., 105, doi: 10.1785/0120140125.

Stevens, J. L., M. O'Brien, and T. W. Thompson (2017), "Decomposition of the Seismic Source Using Numerical Simulations and Observations of Nuclear Explosions," AFRL-RV-PS-TR-2017-0120, Leidos, 10260 Campus Point Drive, San Diego, CA, 31 May 2017.

Stevens, J. L., M. O'Brien, and J. A. Hanson (2020), "Explosion Depth and Yield Estimation in Mountainous Topography," Leidos Final Report to the Defense Threat Reduction Agency, Leidos, 20/0002, August.

Thomas, M. Y., H. S. Bhat, and Y. Klinger (2017), "Effect of Brittle Off-Fault Damage on Earthquake Rupture Dynamics," in Fault Zone Dynamic Processes: Evolution of Fault Properties During Seismic Rupture, Geophysical Monograph 227, American Geophysical Union, Published 2017 by John Wiley & Sons, Inc.

APPENDIX A. MICROMECHANICAL CONSTITUTIVE EQUATIONS

Bhat et al. (2012) extended the Deshpande and Evans (2008) formulation to incorporate an experimentally motivated new crack growth (damage evolution) law that is valid over a wide range of loading rates. This law is sensitive to both the crack tip stress field and its time derivative. Incorporating this feature produces strain-rate sensitivity in the constitutive response. Bhat et al. (2012) expressed the failure condition in terms of stress invariants, however because stress invariants are isotropic, we have reformulated the equations to allow the inherent anisotropy of the cracks to remain.

We follow Deshpande and Evans (2008) but use the Ashby and Sammis (1999) expression for K_I. When the cracks are shut and have no influence on the elastic response of the solid, the strain energy density W is that for an uncracked solid:

$$W = W_0 = \frac{1}{2E}(\sigma_{11}^2 + \sigma_{22}^2 + \sigma_{33}^2) - \frac{\nu}{E}(\sigma_{11}\sigma_{22} + \sigma_{22}\sigma_{33} + \sigma_{33}\sigma_{11}) + \frac{1}{2G}(\sigma_{11}^2 + \sigma_{23}^2 + \sigma_{31}^2) \quad \text{(A-1)}$$

Where the elastic moduli are those of the uncracked solid.

When the wing cracks are activated the energy density can be found by a two-step process. First, seal the cracks (N_V per unit volume) and apply the external loads. The strain energy density is given by W_0 as above. Then, without changing the loads, release the cracks. This results in a change ΔW in the strain energy per crack, whereupon the strain energy becomes

$$W = W_0 + N_V \Delta W \quad \text{(A-2)}$$

The energy for a fixed value of ℓ/a is

$$\Delta W = \frac{1}{E}\int_0^a K_I^2\, 2\pi a da \quad \text{(A-3)}$$

We wish to put the Ashby and Sammis expression for the stress intensity factor in the form

$$K_I = \sqrt{\pi a}(A\sigma_1 + B\sigma_3) \quad \text{(A-4)}$$

so that we can use it in the energy equation and stress-strain relations we have already found following the methodology in Bhat et al. and Thomas et al. Ashby and Sammis wrote the stress intensity factor at the tips of the wing cracks as

$$K_I = \frac{F_3}{(\pi(l+\beta a))^{3/2}} + \frac{2}{\sqrt{\pi}}\left(\sigma_3 + \sigma_3^i\right)\sqrt{l} \quad \text{(A-5)}$$

where the wedging force is

$$F_3 = -(A_1\sigma_1 - A_3\sigma_3)a^2 \quad \text{(A-6)}$$

The internal stress in (5) is

$$\sigma_3^i = \frac{F_3}{A_{crack} - \pi(l+\alpha a)^2} \quad \text{(A-7)}$$

and the average area per crack in (7) is

$$A_{crack} = \pi^{1/3}\left(\frac{3}{4N_V}\right)^{2/3} = \frac{\pi(\alpha a)^2}{D_0^{2/3}} \quad \text{(A-8)}$$

The constants are

$$A_1 = \frac{\pi\sqrt{\beta}}{\sqrt{3}}\left((1+f^2)^{1/2} - f\right) \tag{A-9}$$

$$A_3 = A_1\left\{\frac{\left(1+f^2\right)^{1/2}+f}{(1+f^2)^{1/2}-f}\right\} \tag{A-10}$$

In the 1D model β was set to β= 0.1 to fit the numerical simulations. In the 3D model we treat β as an adjustable parameter. Based on the fits to a wide variety of rock data in Ashby and Sammis (1999) we take β = 0.45.

Ashby and Sammis [eqn. (A-26)] give the following equation for the stress intensity factor

$$K_I = \frac{-A_1\sigma_1\sqrt{\pi a}}{\pi^2\alpha^{3/2}\left((D/D_0)^{1/3}-1+\beta/\alpha\right)^{3/2}}\left\{\left(1-\frac{A_3}{A_1}\lambda\right)\left[1+2\left((D/D_0)^{1/3}-1\right)^2\left(\frac{D_0^{2/3}}{1-D^{2/3}}\right)\right]-\frac{2\lambda}{A_1}\alpha^2\pi^2\left((D/D_0)^{1/3}-1\right)^2\right\} \tag{A-11}$$

where

$$\lambda = \frac{\sigma_3}{\sigma_1} \tag{A-12}$$

Writing K_I explicitly in terms of σ_1 and σ_3

$$K_I = \frac{-A_1\sigma_1\sqrt{\pi a}}{\pi^2\alpha^{3/2}((D/D_0)^{1/3}-1+\beta/\alpha)^{3/2}}\left\{\left(1-\frac{A_3}{A_1}\frac{\sigma_3}{\sigma_1}\right)\left[1+2\left((D/D_0)^{1/3}-1\right)^2\left(\frac{D_0^{2/3}}{1-D^{2/3}}\right)\right]-\frac{2}{A_1}\frac{\sigma_3}{\sigma_1}\alpha^2\pi^2\left((D/D_0)^{1/3}-1\right)^2\right\} \tag{A-13}$$

Define

$$c_1 = \frac{1}{\pi^2\alpha^{3/2}\left((D/D_0)^{1/3}-1+\beta/\alpha\right)^{3/2}} \tag{A-14}$$

$$c_2 = 1+2\left((D/D_0)^{1/3}-1\right)^2\left(\frac{D_0^{2/3}}{1-D^{2/3}}\right) \tag{A-15}$$

$$c_3 = 2\alpha^2\pi^2\left((D/D_0)^{1/3}-1\right)^2 \tag{A-16}$$

as in Deshpande and Evans (eqn. A-9). Then

$$K_I = -A_1c_1\sigma_1\sqrt{\pi a}\left\{c_2\left(1-\frac{A_3}{A_1}\frac{\sigma_3}{\sigma_1}\right)-c_3\frac{1}{A_1}\frac{\sigma_3}{\sigma_1}\right\} \tag{A-17}$$

which can be written

$$K_I = -A_1c_1\sigma_1\sqrt{\pi a}\left\{c_2 - c_2\frac{A_3}{A_1}\frac{\sigma_3}{\sigma_1}-c_3\frac{1}{A_1}\frac{\sigma_3}{\sigma_1}\right\} \tag{A-18}$$

or

$$K_I = -c_1c_2A_1\sigma_1\sqrt{\pi a}+c_1c_2A_3\sigma_3\sqrt{\pi a}+c_1c_3\sigma_3\sqrt{\pi a} \tag{A-19}$$

This is in the required form

$$K_I = \sqrt{\pi a}(A\sigma_1 + B\sigma_3) \tag{A-20}$$

$$A = -c_1 c_2 A_1 \tag{A-21}$$

$$B = c_1 c_2 A_3 + c_1 c_3 \tag{A-22}$$

Now set $K_I = K_{Ic}$ to get an equation for σ_1 as a function of σ_3 and D. This is the equation we need to solve at each time step for crack growth. We can continue to calculate the effective moduli for the cracked solid.

$$\Delta W = \frac{1}{E}\int_0^a K_I^2\, 2\pi a da = \frac{1}{E}\int_0^a \pi a(A\sigma_1 + B\sigma_3)^2\, 2\pi a da = \frac{2\pi^2 a^3}{3E}(A\sigma_1 + B\sigma_3)^2 \tag{A-23}$$

Using $E = 2(1+\nu)G$ and $D_0 = \frac{4}{3}\pi N_V(\alpha a)^3$

$$N_V \Delta W = \frac{\pi D_0}{4\alpha^3 G(1+\nu)}(A\sigma_1 + B\sigma_3)^2 \tag{A-24}$$

The stress-strain expression is found by differentiation W

$$\varepsilon_{ij} = \frac{\partial W}{\partial \sigma_{ij}} \tag{A-26}$$

In the principal coordinate system

$$\varepsilon_1 = \frac{\partial W}{\partial \sigma_1} = \frac{\partial W_0}{\partial \sigma_1} + \frac{\pi D_0}{4\alpha^3 G(1+\upsilon)} 2A(A\sigma_1 + B\sigma_3) \tag{A-27}$$

$$\varepsilon_2 = \frac{\partial W}{\partial \sigma_2} = \frac{\partial W_0}{\partial \sigma_2} \tag{A-28}$$

$$\varepsilon_3 = \frac{\partial W}{\partial \sigma_3} = \frac{\partial W_0}{\partial \sigma_3} + \frac{\pi D_0}{4\alpha^3 G(1+\upsilon)} 2B(A\sigma_1 + B\sigma_3) \tag{A-29}$$

For the elastic components we use the isotropic compliance matrix

$$\varepsilon_{11} = \frac{1}{2(1+\nu)G}[\sigma_{11} - \nu(\sigma_{22} + \sigma_{33})] \tag{A-30}$$

$$\varepsilon_{22} = \frac{1}{2(1+\nu)G}[\sigma_{22} - \nu(\sigma_{11} + \sigma_{33})] \tag{A-31}$$

$$\varepsilon_{33} = \frac{1}{2(1+\nu)G}[\sigma_{33} - \nu(\sigma_{11} + \sigma_{22})] \tag{A-32}$$

$$\varepsilon_{23} = \frac{\sigma_{23}}{2G} \qquad \varepsilon_{13} = \frac{\sigma_{13}}{2G} \qquad \varepsilon_{12} = \frac{\sigma_{12}}{2G} \tag{A-33}$$

Combining the elastic and damage contributions

$$\varepsilon_1 = \frac{1}{2G(1+\upsilon)}\left\{[\sigma_1 - \upsilon(\sigma_2 + \sigma_3)] + \frac{\pi D_0}{\alpha^3} A(A\sigma_1 + B\sigma_3)\right\} \tag{A-34}$$

$$\varepsilon_2 = \frac{1}{2G(1+\upsilon)}[\sigma_2 - \upsilon(\sigma_1 + \sigma_3)] \tag{A-35}$$

$$\varepsilon_3 = \frac{1}{2G(1+\upsilon)}\left\{[\sigma_3 - \upsilon(\sigma_1 + \sigma_2)] + \frac{\pi D_0}{\alpha^3} B(A\sigma_1 + B\sigma_3)\right\} \tag{A-36}$$

In matrix form

$$\begin{bmatrix}\varepsilon_1\\ \varepsilon_2\\ \varepsilon_3\end{bmatrix} = \frac{1}{2G(1+\upsilon)}\begin{bmatrix}M_{11} & M_{12} & M_{13}\\ M_{21} & M_{22} & M_{23}\\ M_{31} & M_{32} & M_{33}\end{bmatrix}\begin{bmatrix}\sigma_1\\ \sigma_2\\ \sigma_3\end{bmatrix} \tag{A-37}$$

where

$$M_{11} = \left(1 + \frac{\pi D_0}{\alpha^3} A^2\right) \tag{A-38}$$

$$M_{12} = -\upsilon \tag{A-38}$$

$$M_{13} = \left(-\nu + \frac{\pi D_0}{\alpha^3} AB\right) \tag{A-39}$$

$$M_{21} = -\upsilon \qquad M_{22} = 1 \qquad M_{23} = -\upsilon \tag{A-40}$$

$$M_{31} = \left(-\nu + \frac{\pi D_0}{\alpha^3} AB\right) \qquad M_{32} = -\nu \qquad M_{33} = \left(1 + \frac{\pi D_0}{\alpha^3} B^2\right) \tag{A-41}$$

In matrix form

$$\begin{bmatrix}\varepsilon_1\\ \varepsilon_2\\ \varepsilon_3\end{bmatrix} = \left(\frac{1}{2G(1+\upsilon)}\right)\begin{bmatrix}\left(1 + \frac{\pi D_0}{\alpha^3} A^2\right) & -\upsilon & \left(-\nu + \frac{\pi D_0}{\alpha^3} AB\right)\\ -\upsilon & 1 & -\upsilon\\ \left(-\nu + \frac{\pi D_0}{\alpha^3} AB\right) & -\upsilon & \left(1 + \frac{\pi D_0}{\alpha^3} B^2\right)\end{bmatrix}\begin{bmatrix}\sigma_1\\ \sigma_2\\ \sigma_3\end{bmatrix} \tag{A-42}$$

It remains to invert *M* to find expressions for σ_1, σ_2, and σ_3 that can be used to update the stress state.

Let

$$\bar{A}_1 = \left(1 + \frac{\pi D_0}{\alpha^3} A^2\right) \quad \bar{A}_2 = \left(-\nu + \frac{\pi D_0}{\alpha^3} AB\right) \quad \bar{A}_3 = \left(1 + \frac{\pi D_0}{\alpha^3} B^2\right) \tag{A-43}$$

$$\bar{G}_1 = \left(\frac{1}{2G(1+\upsilon)}\right) \tag{A-44}$$

Then

$$M = \bar{G}_1 \begin{bmatrix} \bar{A}_1 & -\upsilon & \bar{A}_2 \\ -\upsilon & 1 & -\upsilon \\ \bar{A}_2 & -\upsilon & \bar{A}_3 \end{bmatrix} \tag{A-46}$$

and

$$\det(M) = \bar{G}_1^3[\bar{A}_1\bar{A}_3 - \bar{A}_2^2 + \upsilon^2(-\bar{A}_1 + 2\bar{A}_2 - \bar{A}_3)] \tag{A-47}$$

$$M^{-1} = \frac{1}{\bar{G}_1} \frac{\begin{bmatrix} (\bar{A}_3 - \upsilon^2) & -(-\upsilon\bar{A}_3 + \upsilon\bar{A}_2) & (\upsilon^2 - \bar{A}_2) \\ -(-\upsilon\bar{A}_3 + \upsilon\bar{A}_2) & (\bar{A}_1\bar{A}_3 - \bar{A}_2^2) & -(-\upsilon\bar{A}_1 + \upsilon\bar{A}_2) \\ (\upsilon^2 - \bar{A}_2) & -(-\upsilon\bar{A}_1 + \upsilon\bar{A}_2) & (\bar{A}_1 - \upsilon^2) \end{bmatrix}}{[\bar{A}_1\bar{A}_3 - \bar{A}_2^2 + \upsilon^2(-\bar{A}_1 + 2\bar{A}_2 - \bar{A}_3)]} \tag{A-48}$$

Note that these are all written in terms of the principal stresses and strains, so we need to rotate to the directions of the principal stresses in order to use the equations. For spherically symmetric problems, we always have σ_1 in the radial direction and $\sigma_2=\sigma_3$. We assume that cracks are randomly oriented around the radial direction. We can then use an axisymmetric form for the equations above:

$$\begin{bmatrix} \varepsilon_1 \\ \varepsilon_2 \\ \varepsilon_3 \end{bmatrix} = \left(\frac{1}{2G(1+\upsilon)}\right) \begin{bmatrix} \left(1 + 2\frac{\pi D_0}{\alpha^3}A^2\right) & \left(-\nu + \frac{\pi D_0}{\alpha^3}AB\right) & \left(-\nu + \frac{\pi D_0}{\alpha^3}AB\right) \\ \left(-\nu + \frac{\pi D_0}{\alpha^3}AB\right) & \left(1 + \frac{\pi D_0}{\alpha^3}B^2\right) & -\upsilon \\ \left(-\nu + \frac{\pi D_0}{\alpha^3}AB\right) & -\upsilon & \left(1 + \frac{\pi D_0}{\alpha^3}B^2\right) \end{bmatrix} \begin{bmatrix} \sigma_1 \\ \sigma_2 \\ \sigma_3 \end{bmatrix}$$

And its inverse, defining $A_{1s} = 1 + 2\frac{\pi D_0}{\alpha^3}A^2$

(A-49)

$$M^{-1} = \frac{1}{\bar{G}_1} \frac{\begin{bmatrix} (\bar{A}_3^2 - \upsilon^2) & -(\bar{A}_2\bar{A}_3 + \upsilon\bar{A}_2) & -(\bar{A}_2\bar{A}_3 + \upsilon\bar{A}_2) \\ -(\bar{A}_2\bar{A}_3 + \upsilon\bar{A}_2) & (A_{1s}\bar{A}_3 - \bar{A}_2^2) & (\upsilon A_{1s} + \bar{A}_2^2) \\ -(\bar{A}_2\bar{A}_3 + \upsilon\bar{A}_2) & (\upsilon A_{1s} + \bar{A}_2^2) & (A_{1s}\bar{A}_3 - \bar{A}_2^2) \end{bmatrix}}{\left[A_{1s}\bar{A}_3{}^2 - 2\upsilon\bar{A}_2^2 - 2\bar{A}_3\bar{A}_2^2 - \upsilon^2 A_{1s}\right]}$$

APPENDIX B

DIAGNOSTIC DATA FROM THE 1D SHOAL CALCULATIONS

List of Figures

Figure **Page**

Figure B-1. K1R. Units are MPa-sqrt(m). K1R must exceed 1.0 MPa-$m^{1/2}$ for crack growth to occur..... 67

Figure B-2. d(K1R)/dt*2.e-5/K1C..... 68

Figure B-3. Dependence of crack velocity on dK1R..... 68

Figure B-4. Crack growth speed at 99 m calculated by solving equation 10, section 3.1.3. 69

Figure B-5. Crack growth speed at 99 m.. 70

Figure B-6. Damage as a function of time at 99m. 71

Figure B-7. Strain in the first 0.1 s..... 72

Figure B-8. Stress in the first 0.1 s..... 73

Figure B-9. Stress vs. time at a distance of 99m in the first 1.0 s. Top row: a=1mm, a=1cm; bottom row a=10cm, a=1m. 0-1s..... 74

Figure B-10. Radial displacement and velocity. 75

Figure B-11. RVP and RDP..... 76

Figure B-12. Damage at 0.02 seconds. Top: 1mm (l), 1cm (r). Bottom: 10cm (l). 1m (r). 77

Figure B-13. Damage at 0.1s. Top: 1mm (l), 1cm (r). Bottom: 10cm (l). 1m (r). 78

Figure B-14. Damage vs. Time for Case 9, a=1mm..... 79

Figure B-15. Case 9, a=1cm 80

Figure B-16. Case 9, a=10 cm 81

Figure B-17. Case 9, a=1m..... 82

Figure B-18. Calculated quantities for Sammis micromechanical damage model for four values of the initial crack size acrack..... 83

APPENDIX B. DIAGNOSTIC DATA FROM THE 1D SHOAL CALCULATIONS

To aid in understanding the calculations and the differences in results due to different parameters, we collected an extensive amount of diagnostic data and generated many plots. A sampling of these are shown here.

B.1 Comparison of K1R, crack growth, damage and stress/strain at 99m for Case9 with a=1mm to 1m.

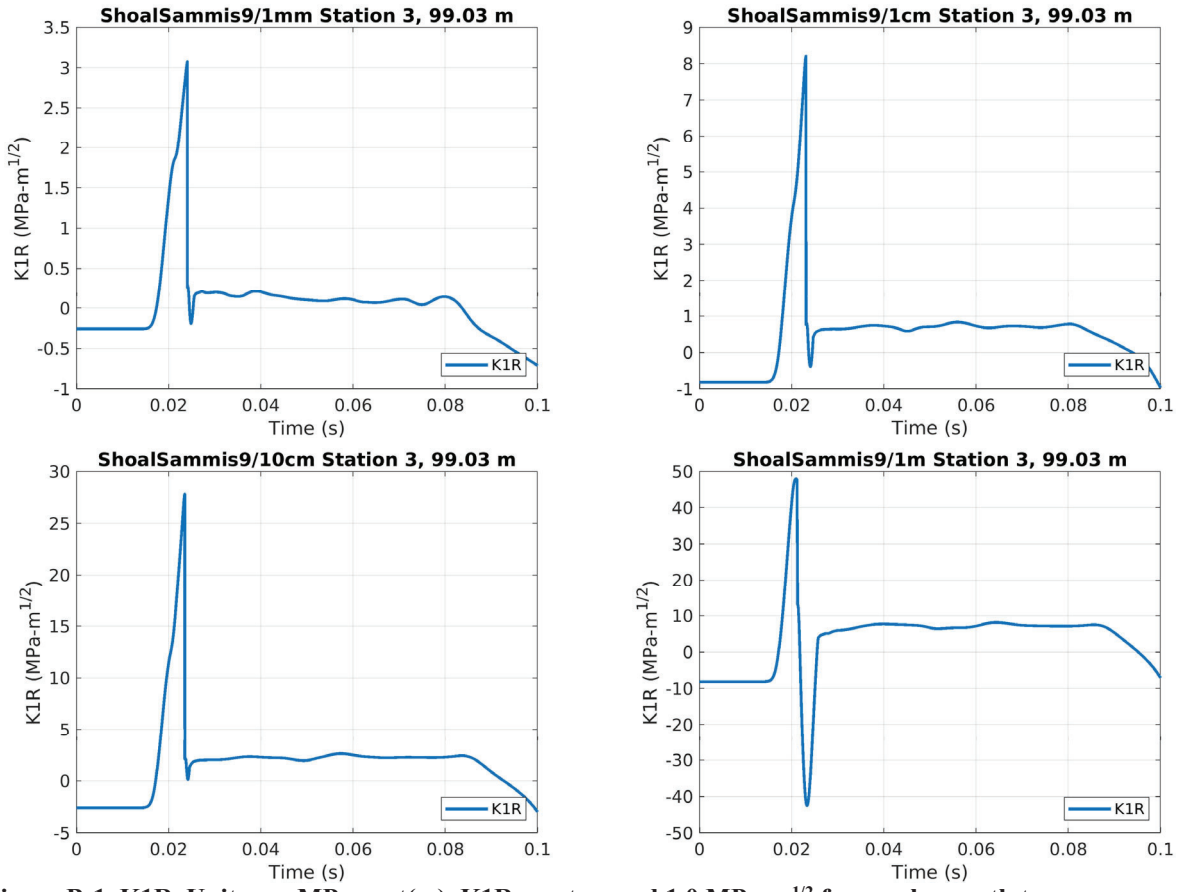

Figure B-1. K1R. Units are MPa-sqrt(m). K1R must exceed 1.0 MPa-m$^{1/2}$ for crack growth to occur.

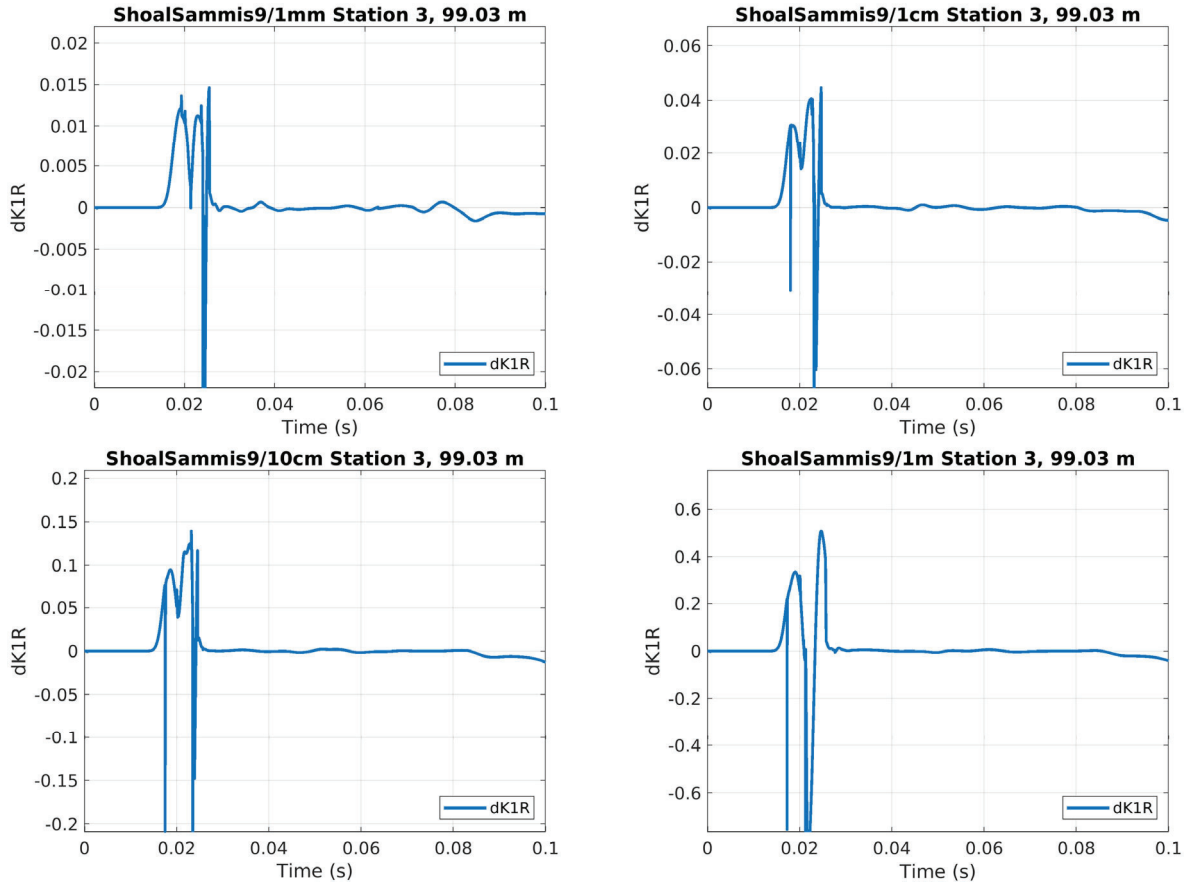

Figure B-2. d(K1R)/dt*2.e-5/K1C. This is the factor that controls crack growth speed. Negative spikes happen when a tensile crack opens.

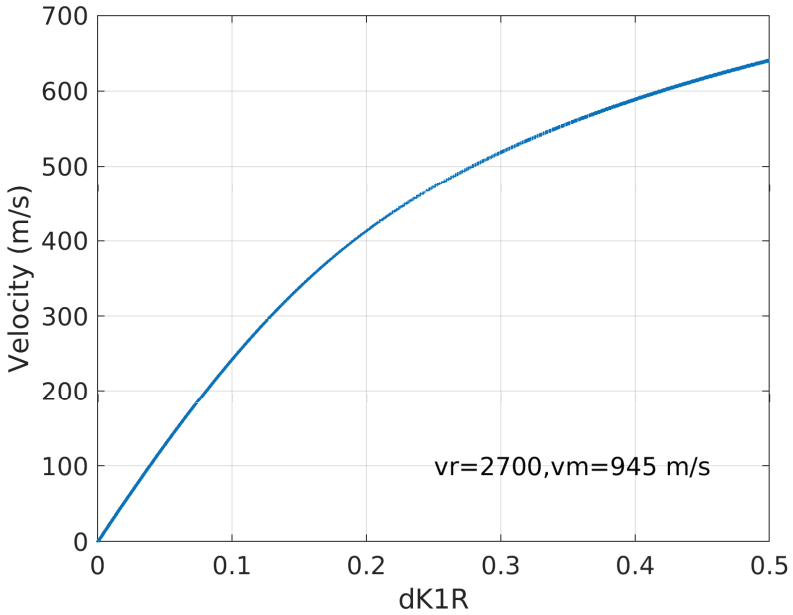

Figure B-3. Dependence of crack velocity on dK1R.

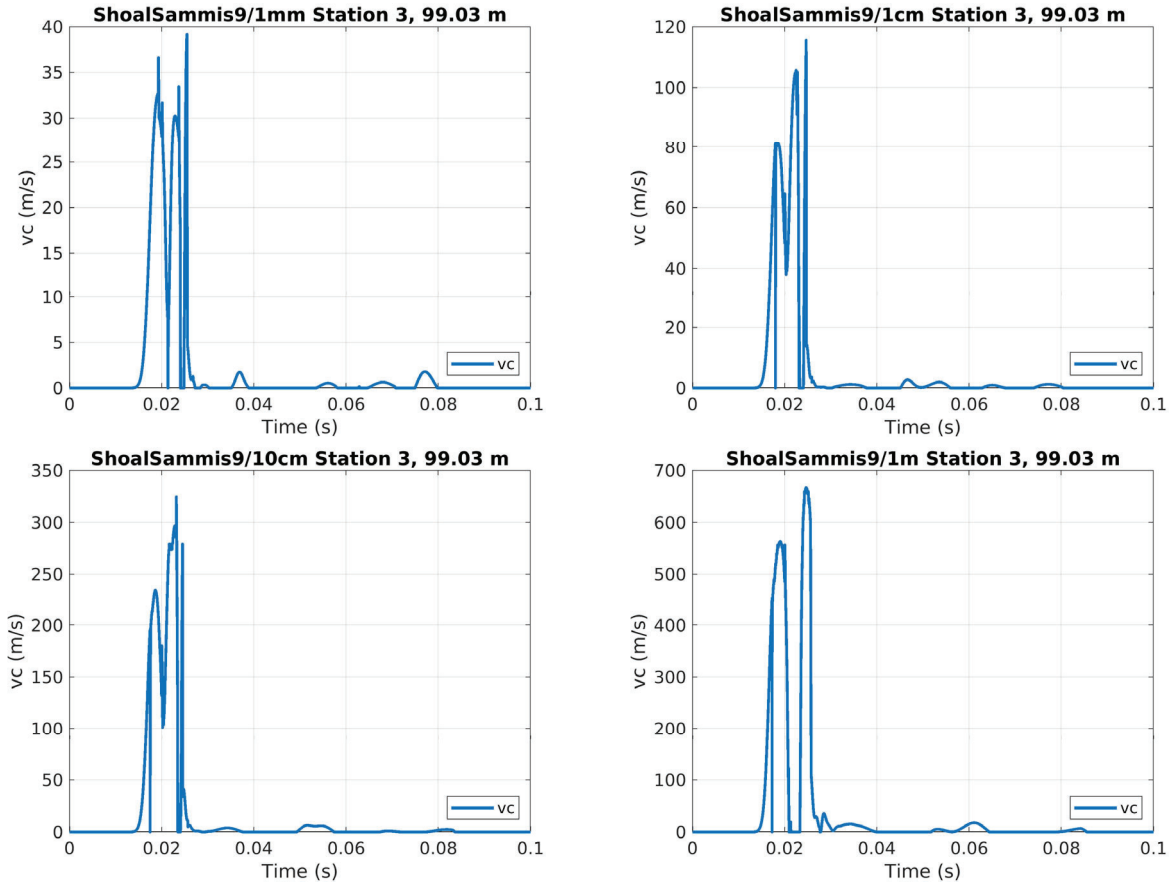

Figure B-4. Crack growth speed at 99 m calculated by solving equation 10, section 3.1.3.

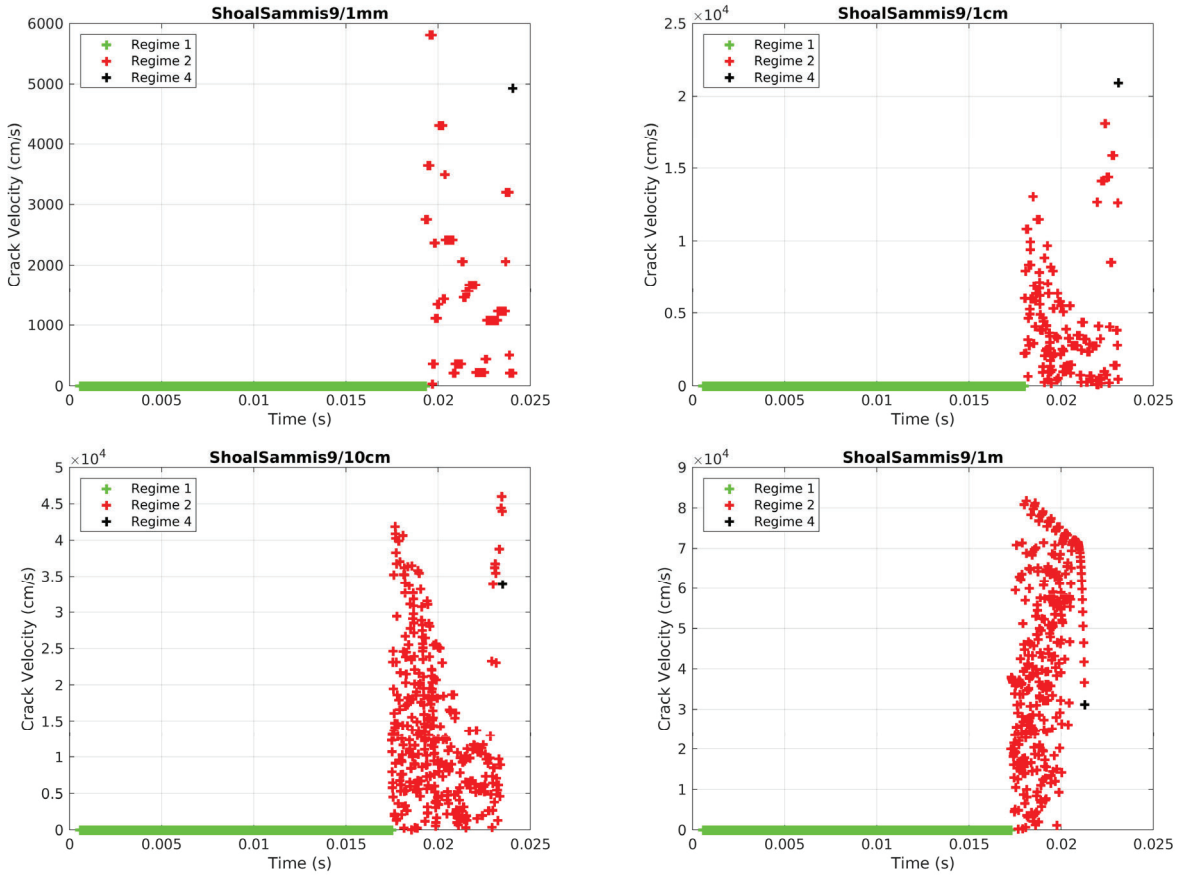

Figure B-5. Crack growth speed at 99 m. Each point corresponds to the speed of a crack extension at a time point in the calculation. Failure is reached at the last (black) point.

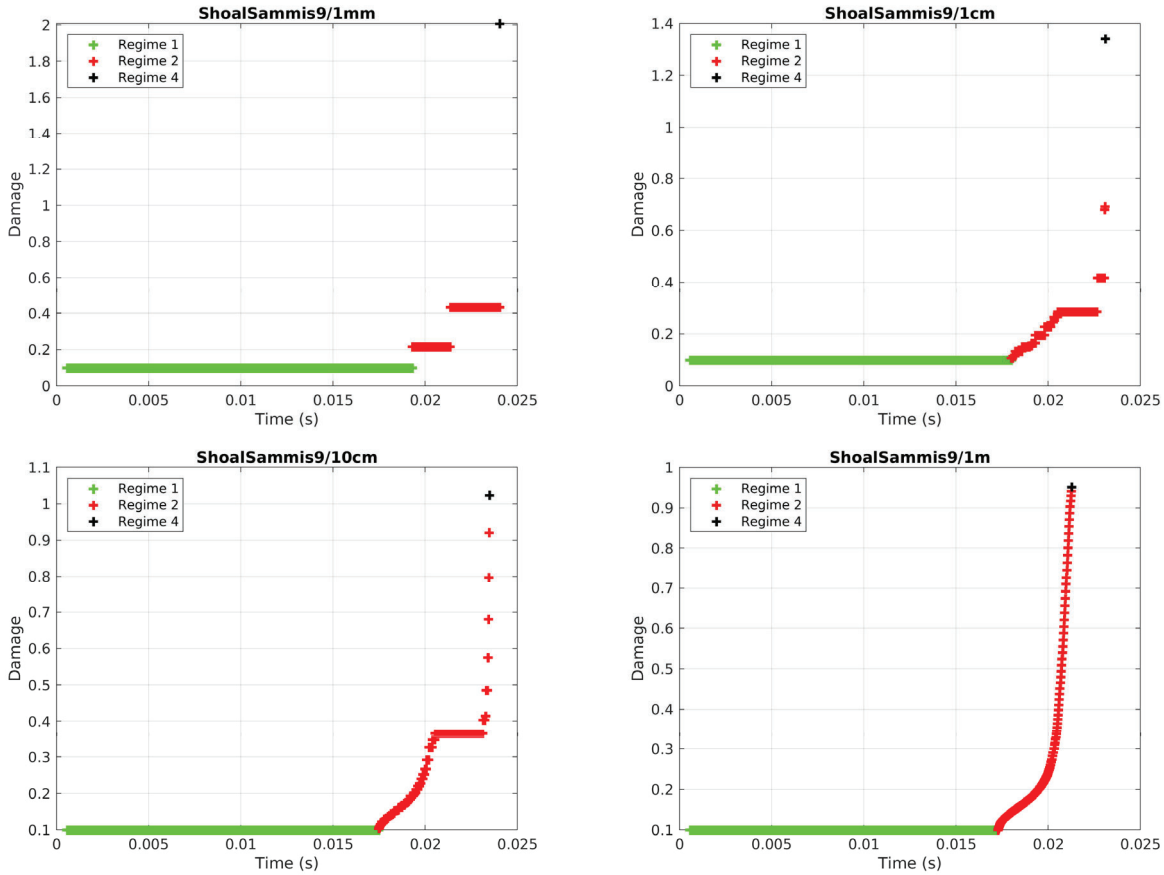

Figure B-6. Damage as a function of time at 99m. Failure is reached at the last (black) point, which is the first point where damage exceeds 0.95.

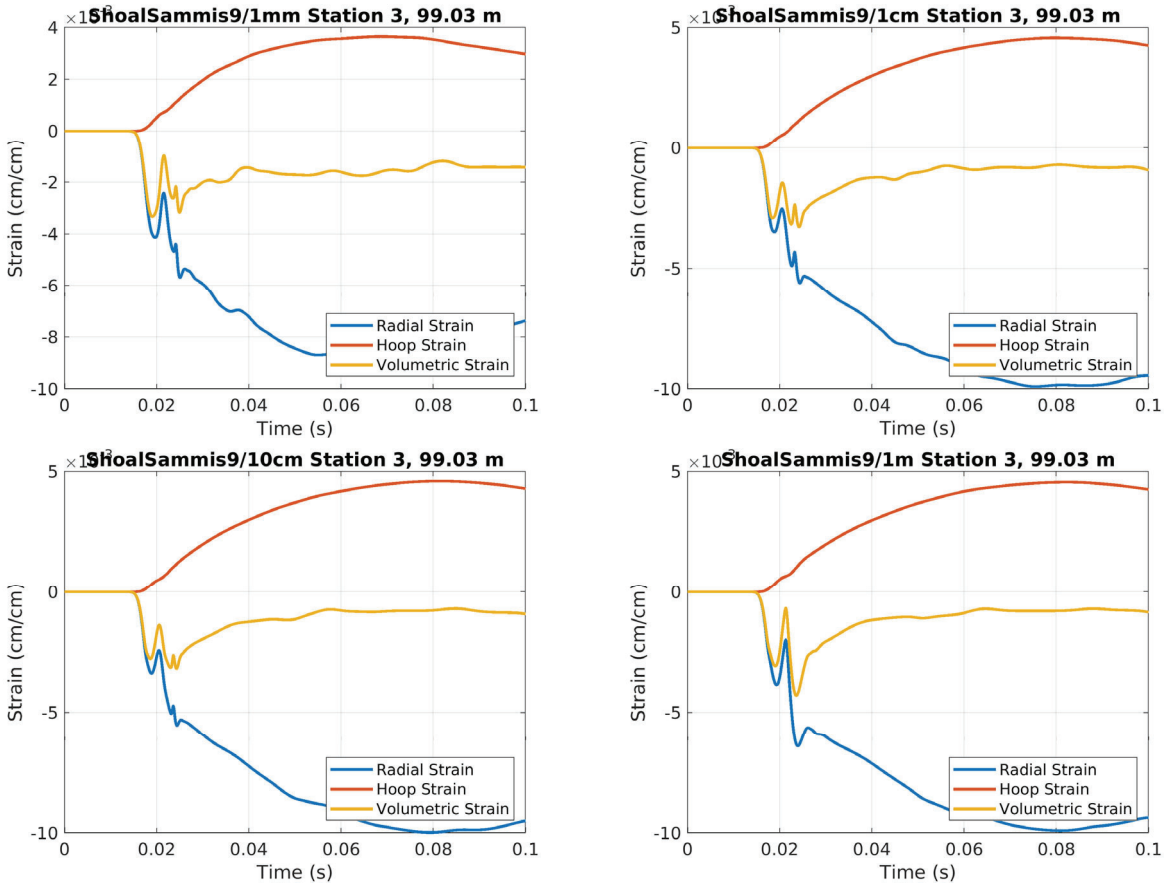

Figure B-7. Strain in the first 0.1 s.

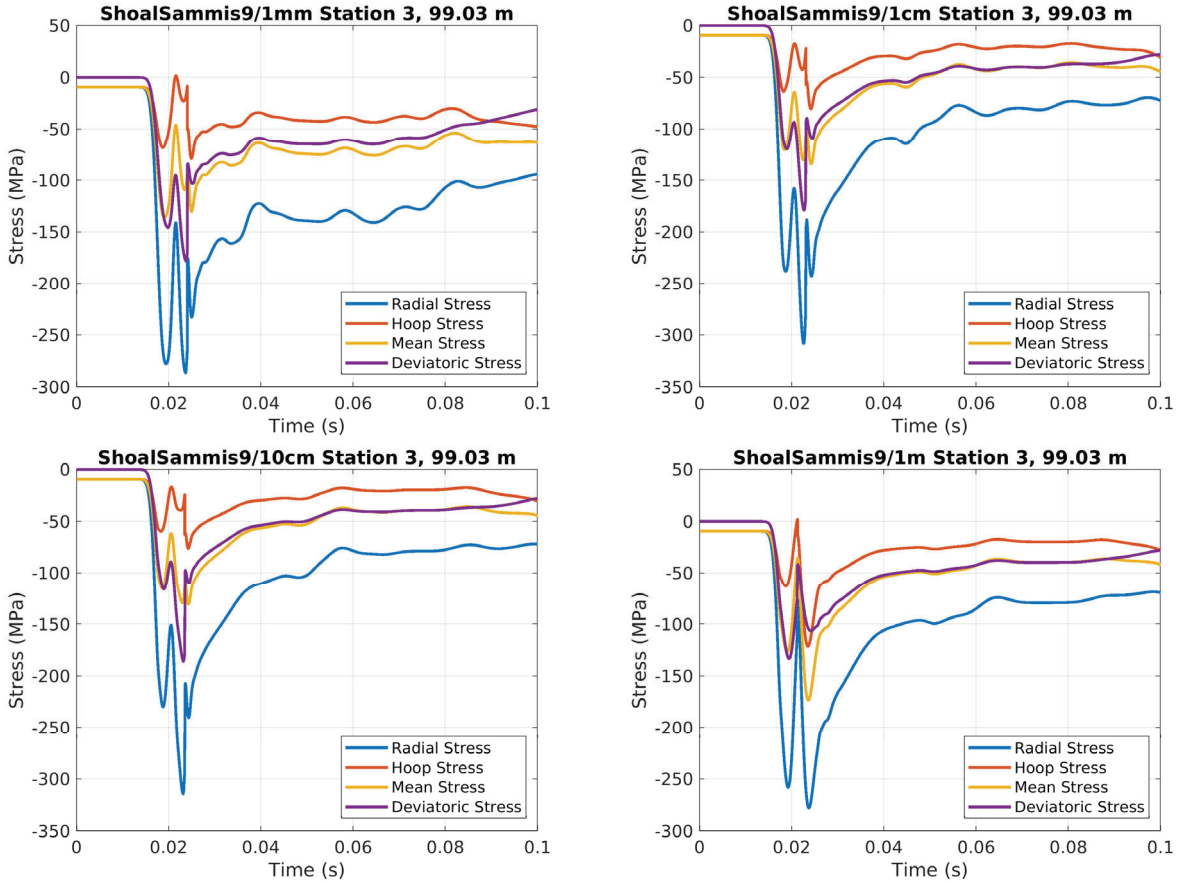

Figure B-8. Stress in the first 0.1 s.

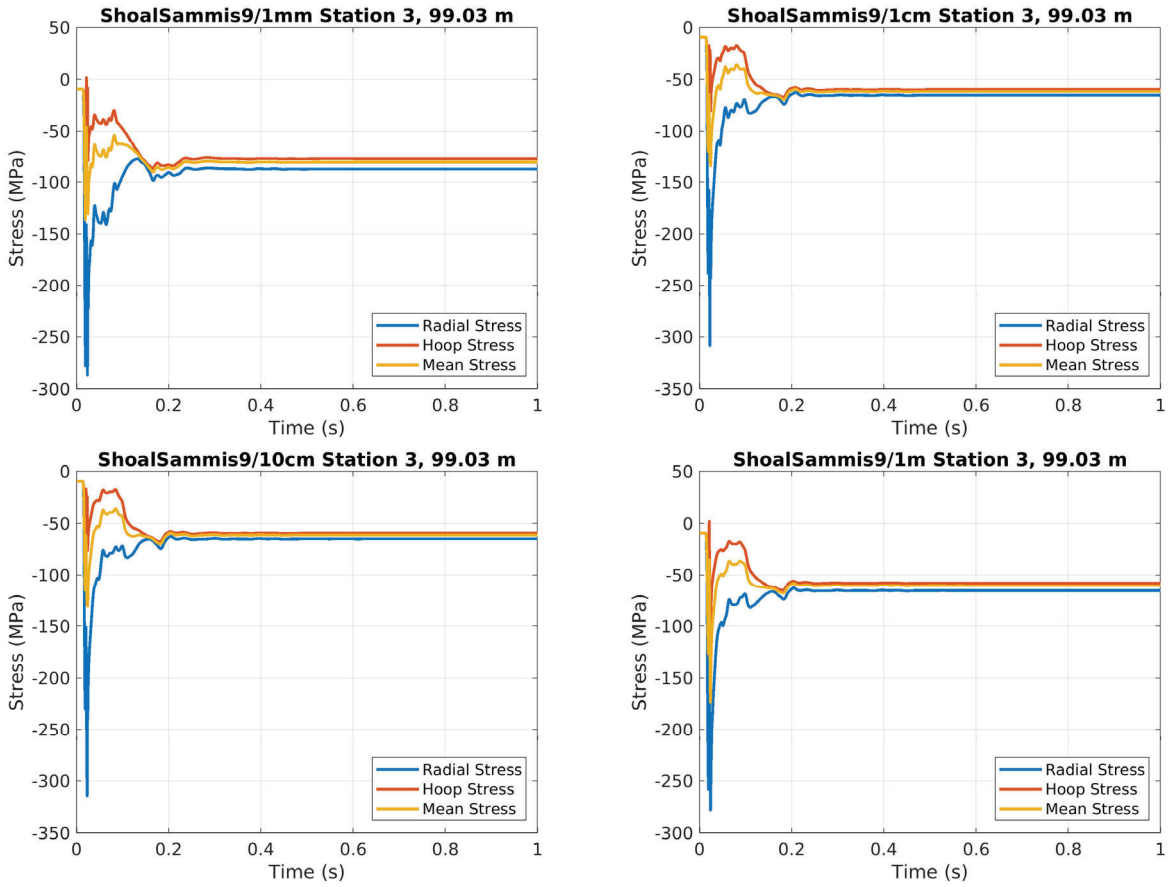

Figure B-9. Stress vs. time at a distance of 99m in the first 1.0 s. Top row: a=1mm, a=1cm; bottom row a=10cm, a=1m. 0-1s.

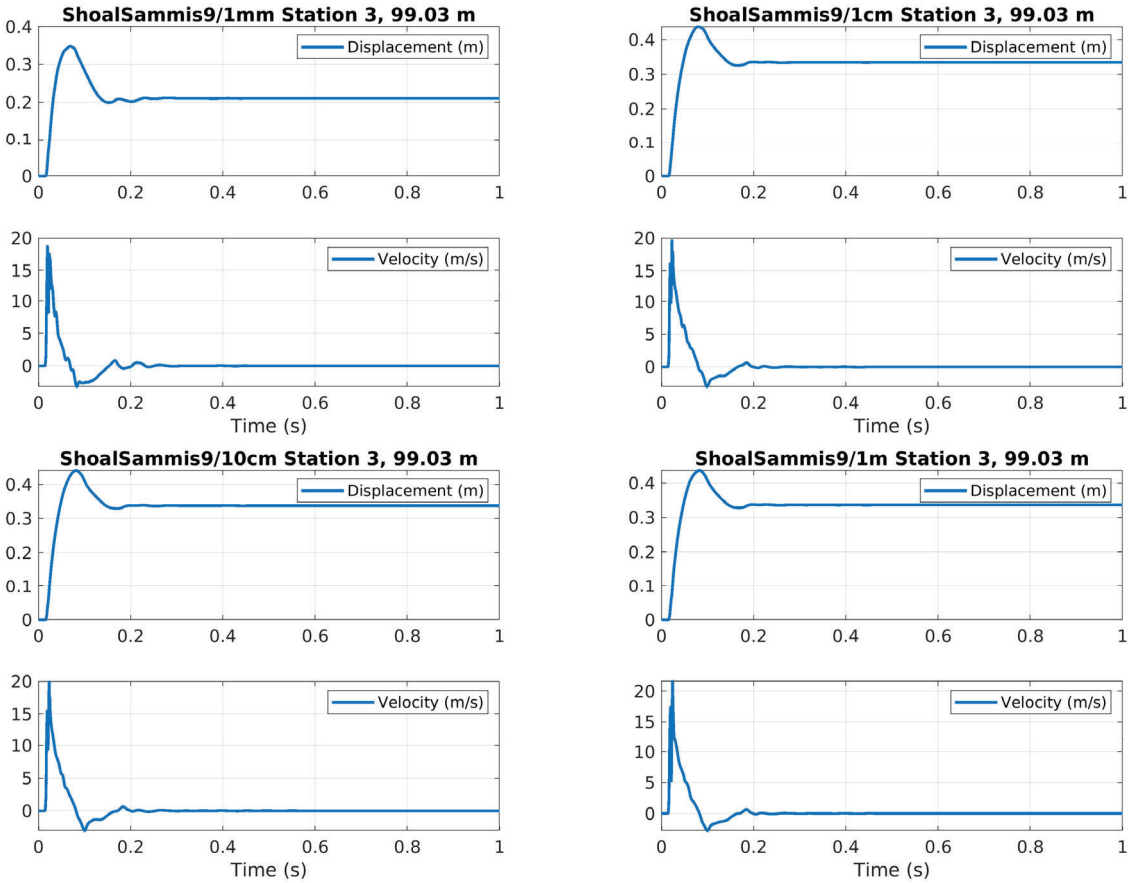

Figure B-10. Radial displacement and velocity.

B.2 RDP and RVP for Case 9

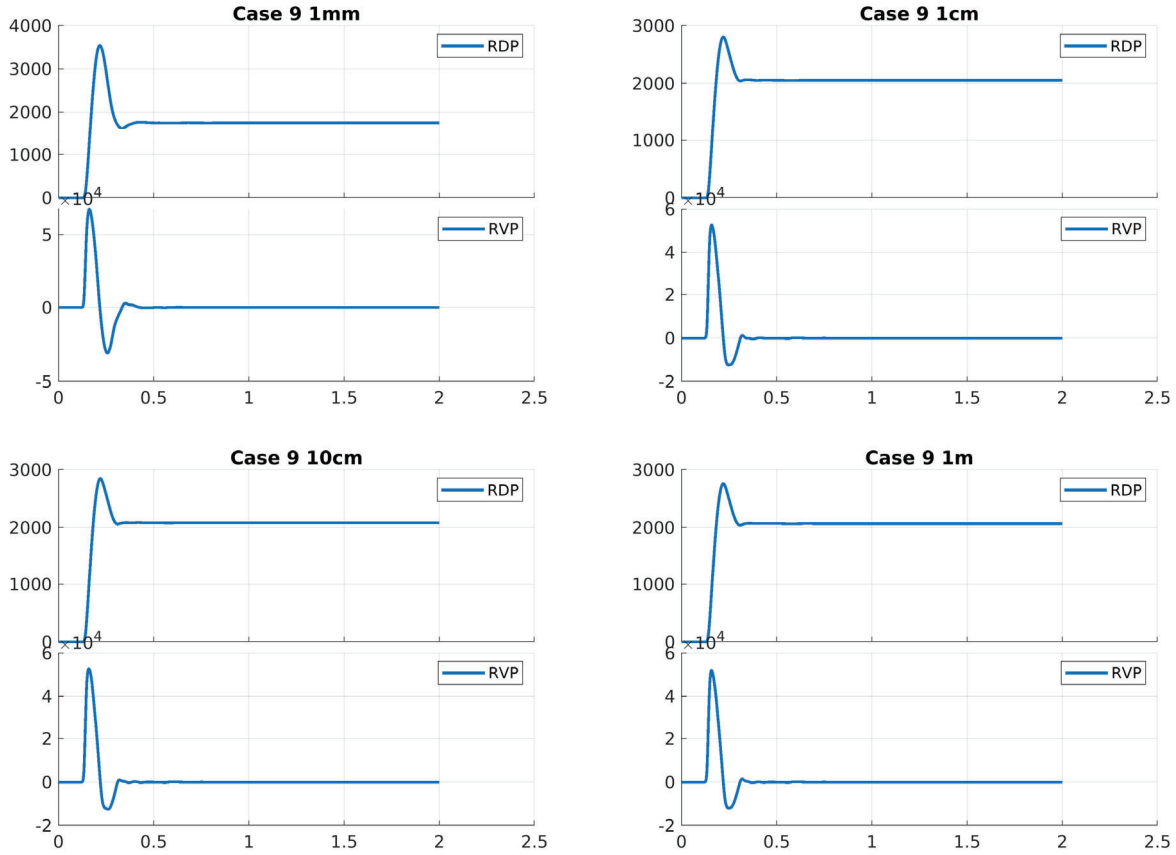

Figure B-11. RVP and RDP

B.3 Damage vs. Location and Time for Case 9

Figure B-12 and Figure B-13 show damage as a function of location for case 9 with four values of *a* at 0.02 and 0.1 seconds.

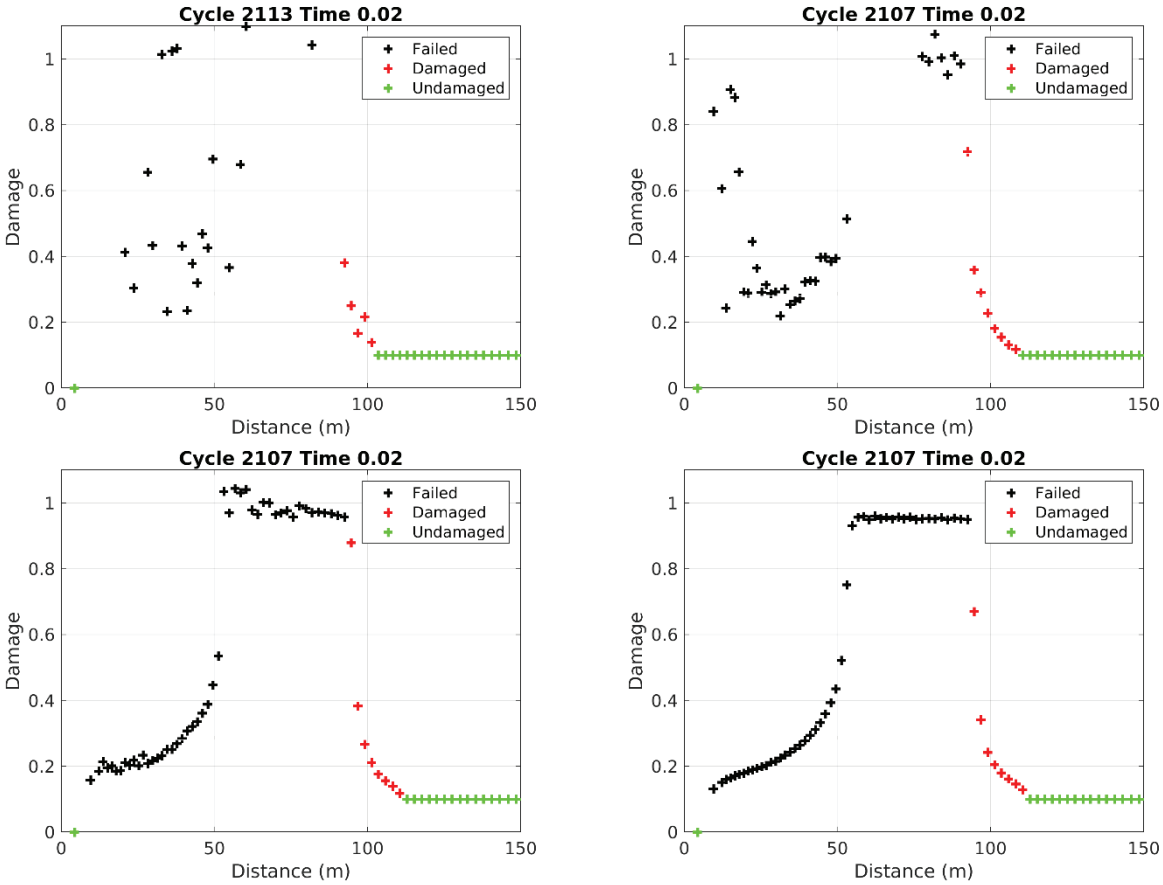

Figure B-12. Damage at 0.02 seconds. Top: 1mm (l), 1cm (r). Bottom: 10cm (l). 1m (r).

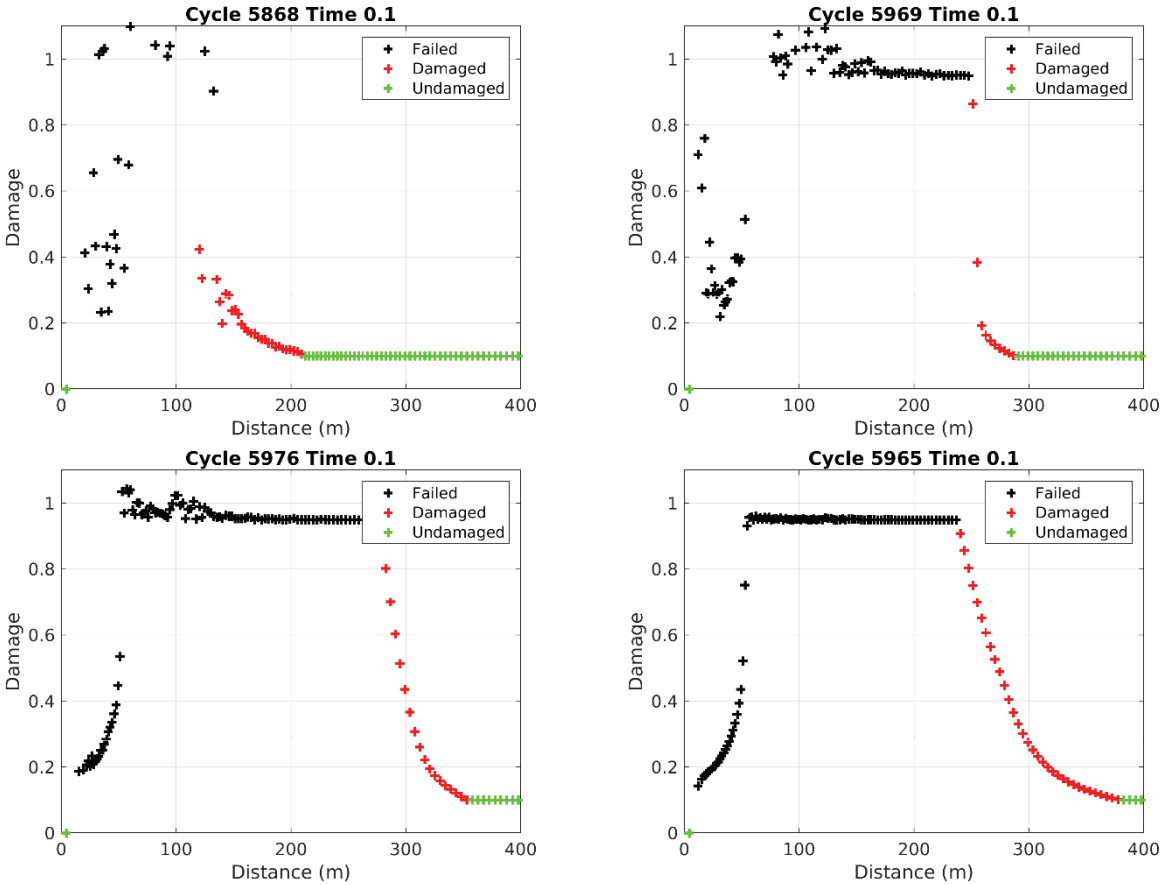

Figure B-13. Damage at 0.1s. Top: 1mm (l), 1cm (r). Bottom: 10cm (l). 1m (r).

Figure B-14 to Figure B-17 show damage vs. time for Case#9 with a increasing from 1 mm to 1 m.

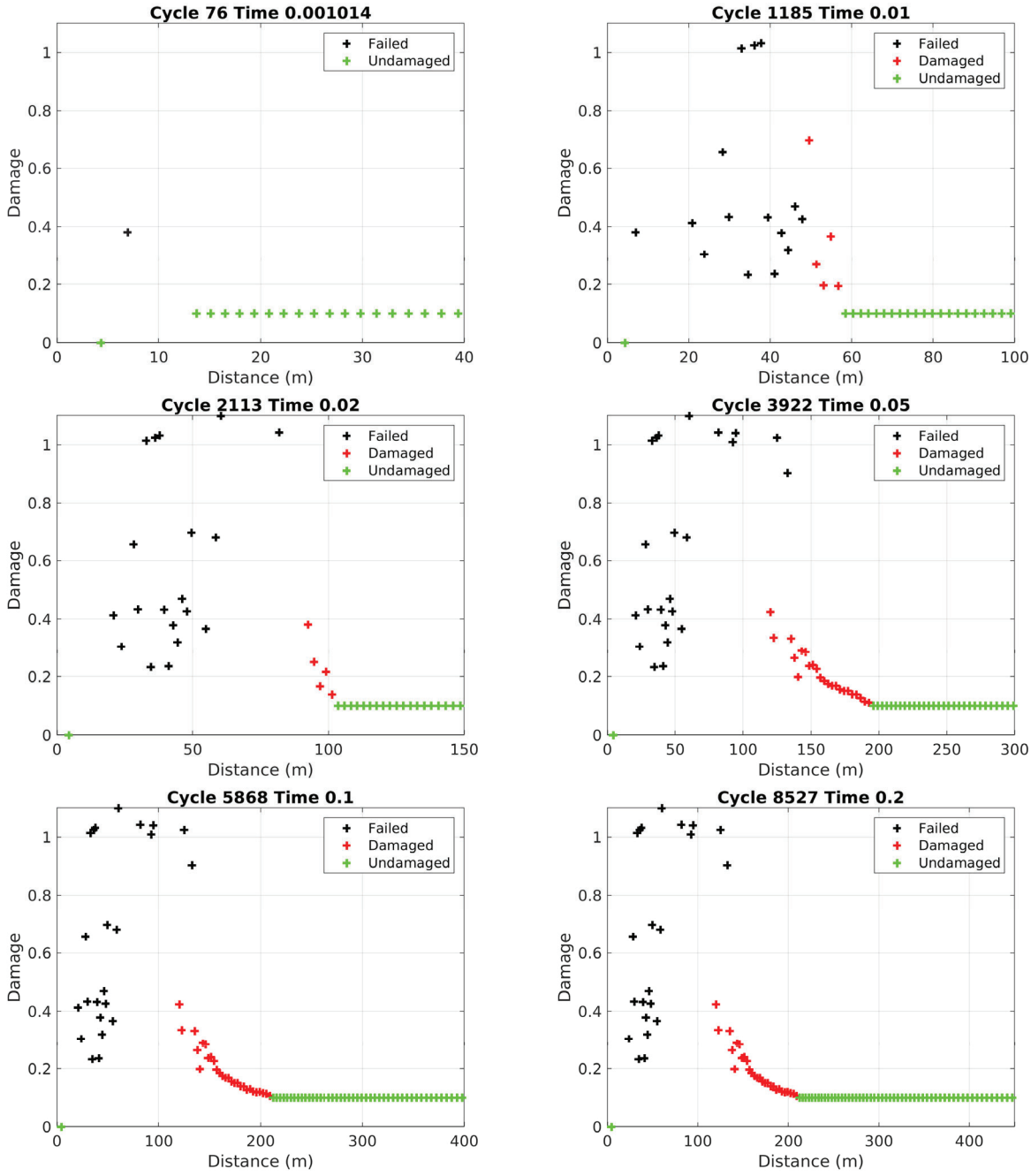

Figure B-14. Damage vs. Time for Case 9, a=1mm

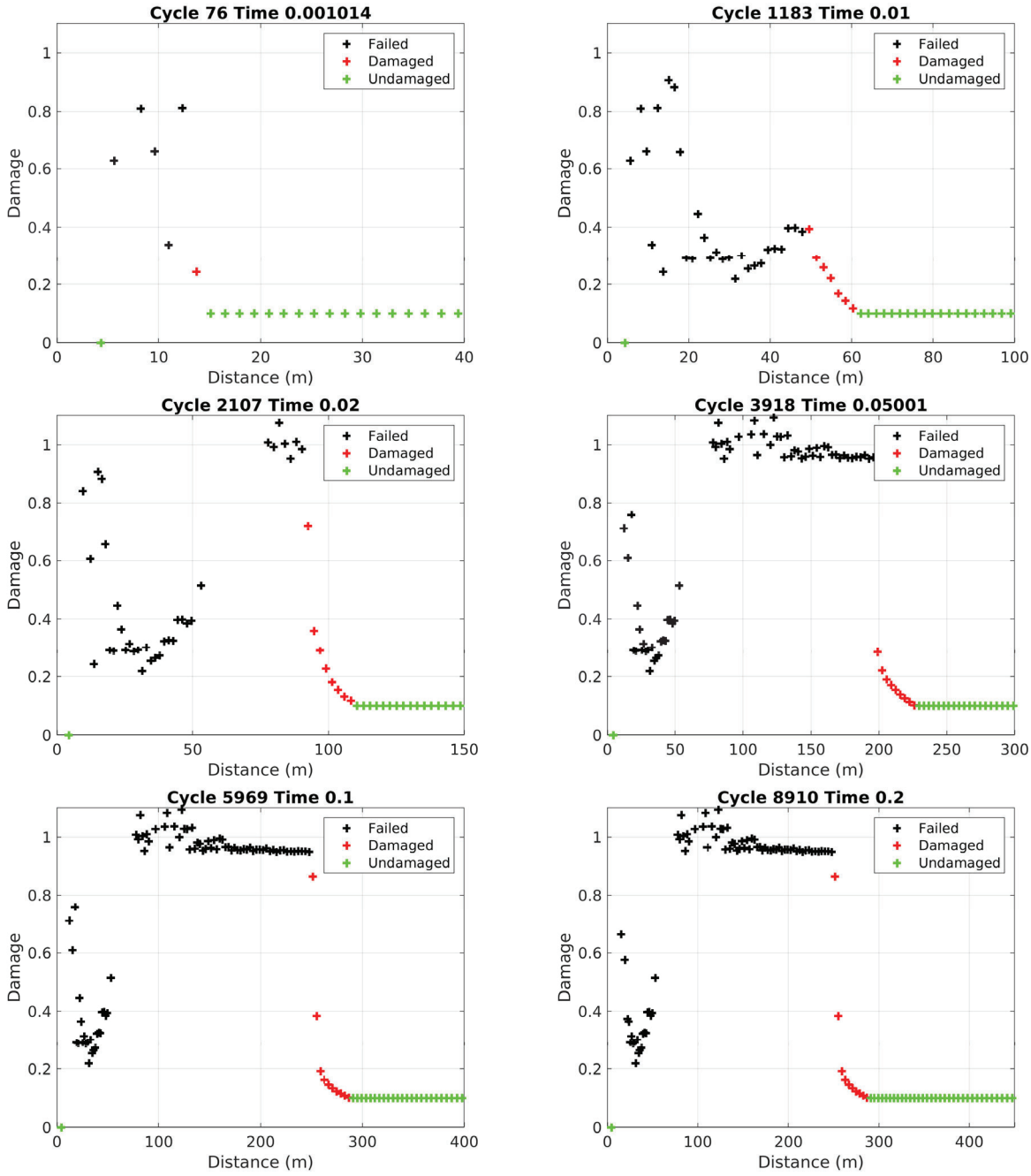

Figure B-15 Case 9, a=1cm

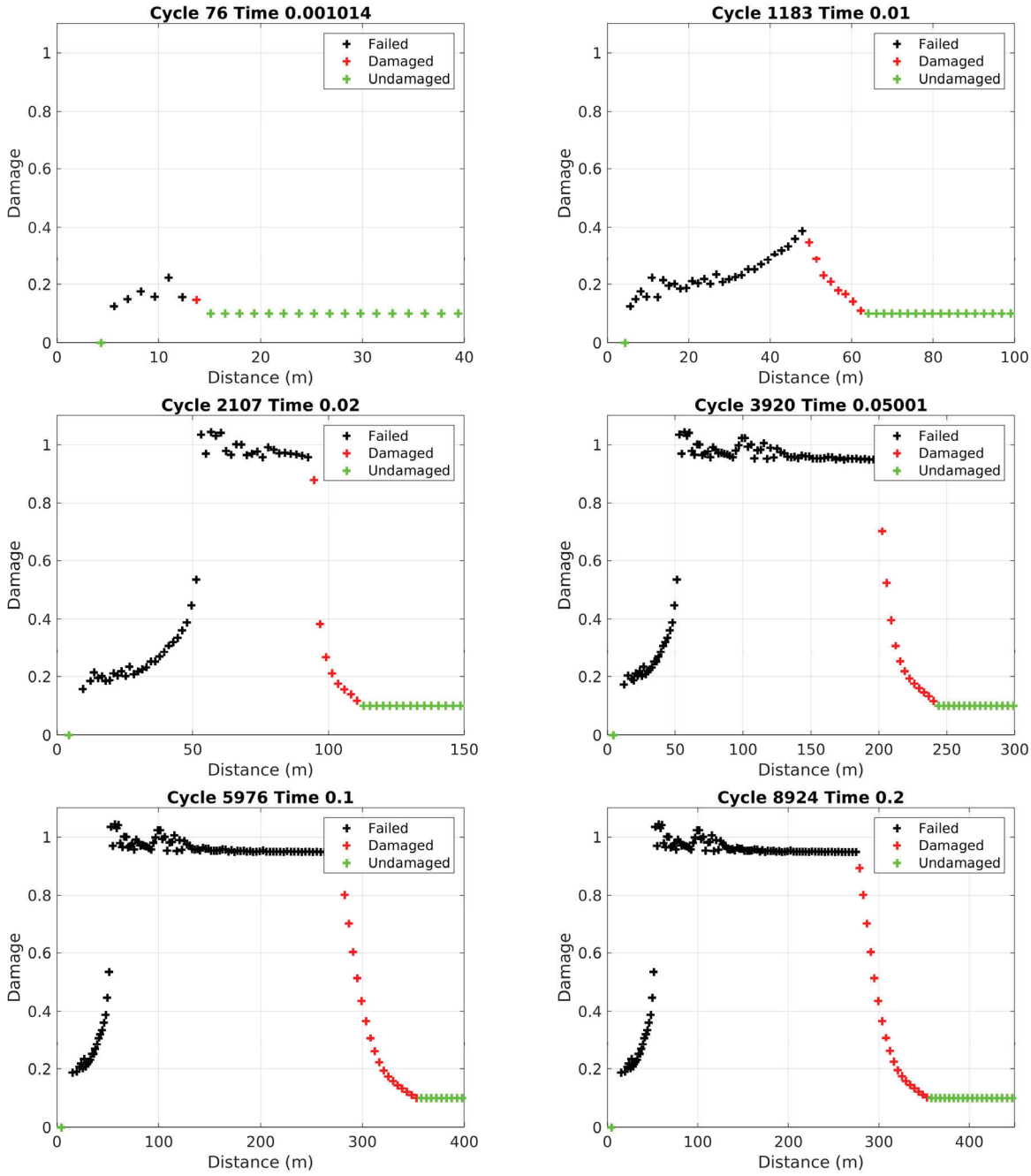

Figure B-16. Case 9, a=10 cm

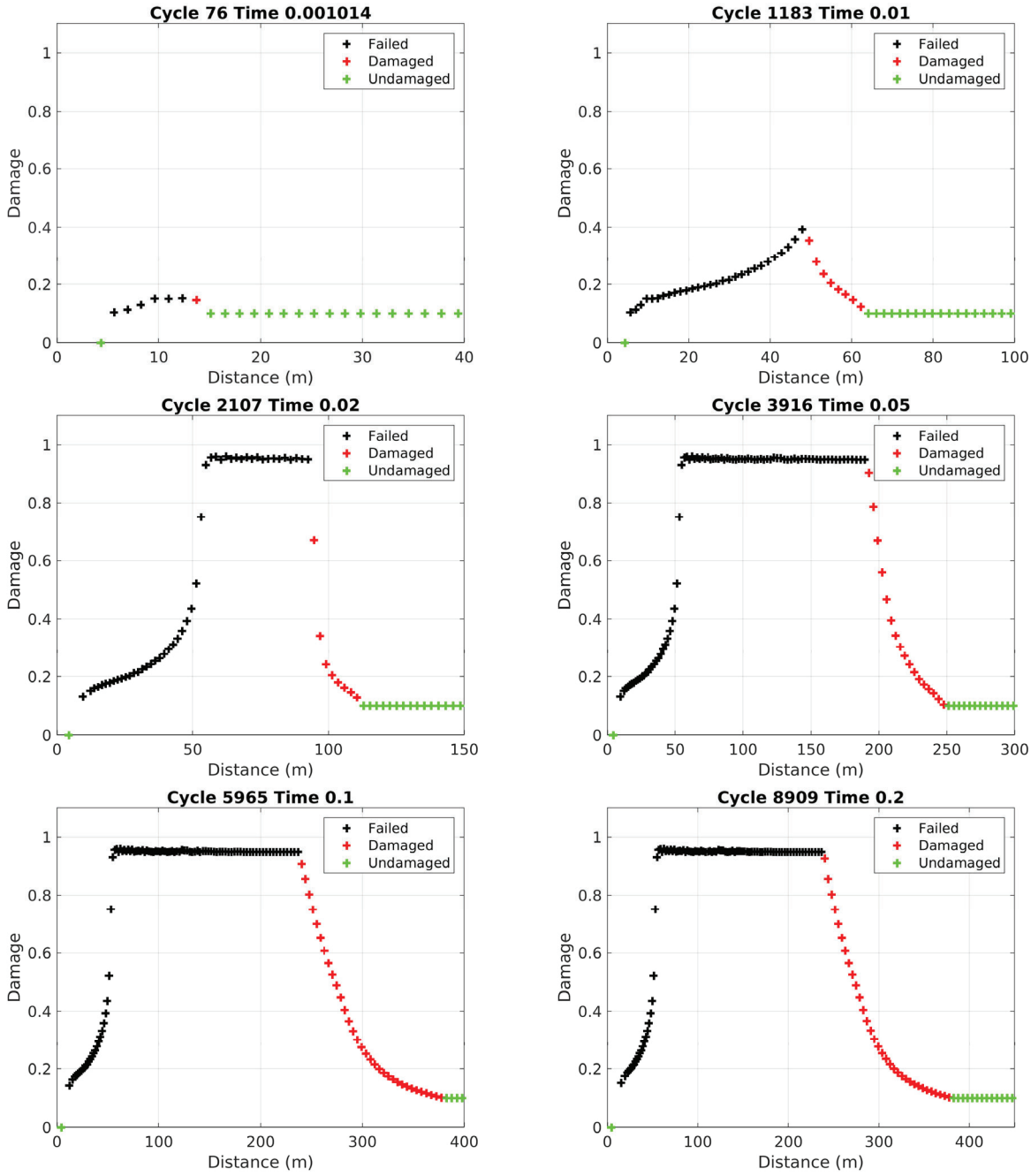

Figure B-17. Case 9, a=1m

B.4 Calculated Material Properties

```
Matprops:
 nsammis_matprop=    1
         K= 3.790E+11
         G= 2.380E+11
       rho= 2.600E+00
         E= 5.904E+11
      pois= 2.404E-01
    lambda= 2.203E+11
        vp= 5.175E+05
        vs= 3.026E+05
        vr= 2.723E+05
        vm= 1.000E+05
       K1C= 1.000E+08
    acrack= 1.000E-01
      fric= 6.000E-01
        D0= 1.000E-01
       phi= 5.152E-01
     alpha= 8.702E-01
        Nv= 3.623E+01
      beta= 4.500E-01
  shapefac= 2.000E+00 (Not used)
 End Matprops
 Damage Dependent Quantities
         D= 1.000E-01
        c1= 3.356E-01
        c2= 1.000E+00
        c3= 0.000E+00
        A1= 6.889E-01
        A3= 2.149E+00
  A_Sammis=-2.312E-01
  B_Sammis= 7.213E-01
  E_Sammis= 1.053E+00
       A1S= 1.051E+00
    A1Ssym= 0.000E+00
       A2S=-3.199E-01
       A3S= 1.248E+00
       A4S= 2.088E-01
    ASmat(3,3)=  6.963E+11  2.205E+11
2.209E+11  2.205E+11  6.889E+11  1.892E+11
2.209E+11  1.892E+11  5.661E+11
    MSmat(3,3)=  1.737E-12 -4.071E-13 -5.418E-
13 -4.071E-13  1.694E-12 -4.071E-13 -5.418E-13
-4.071E-13  2.114E-12
   ASmatT(3,3)=  6.826E+11  2.066E+11
1.768E+11  2.066E+11  6.826E+11  1.768E+11
1.768E+11  1.768E+11  5.587E+11
   MSmatT(3,3)=  1.694E-12 -4.071E-13 -4.071E-
13 -4.071E-13  1.694E-12 -4.071E-13 -4.071E-13
-4.071E-13  2.047E-12
 ASmatSym(3,3)=  6.963E+11  2.210E+11
2.210E+11  2.210E+11  5.615E+11  1.648E+11
2.210E+11  1.648E+11  5.615E+11
 MSmatSym(3,3)=  1.780E-12 -5.418E-13 -5.418E-
13 -5.418E-13  2.114E-12 -4.071E-13 -5.418E-13
-4.071E-13  2.114E-12
End Damage Dependent Quantities
```

1 mm (cgs units)

```
Matprops:
 nsammis_matprop=    1
         K= 3.790E+11
         G= 2.380E+11
       rho= 2.600E+00
         E= 5.904E+11
      pois= 2.404E-01
    lambda= 2.203E+11
        vp= 5.175E+05
        vs= 3.026E+05
        vr= 2.723E+05
        vm= 1.000E+05
       K1C= 1.000E+08
    acrack= 1.000E+00
      fric= 6.000E-01
        D0= 1.000E-01
       phi= 5.152E-01
     alpha= 8.702E-01
        Nv= 3.623E-02
      beta= 4.500E-01
  shapefac= 2.000E+00 (Not used)
 End Matprops
 Damage Dependent Quantities
         D= 1.000E-01
        c1= 3.356E-01
        c2= 1.000E+00
        c3= 0.000E+00
        A1= 6.889E-01
        A3= 2.149E+00
  A_Sammis=-2.312E-01
  B_Sammis= 7.213E-01
  E_Sammis= 1.053E+00
       A1S= 1.051E+00
    A1Ssym= 0.000E+00
       A2S=-3.199E-01
       A3S= 1.248E+00
       A4S= 2.088E+00
    ASmat(3,3)=  6.963E+11  2.205E+11
2.209E+11  2.205E+11  6.889E+11  1.892E+11
2.209E+11  1.892E+11  5.661E+11
    MSmat(3,3)=  1.737E-12 -4.071E-13 -5.418E-
13 -4.071E-13  1.694E-12 -4.071E-13 -5.418E-13
-4.071E-13  2.114E-12
   ASmatT(3,3)=  6.468E+11  1.708E+11
6.363E+10  1.708E+11  6.468E+11  6.363E+10
6.363E+10  6.363E+10  2.011E+11
   MSmatT(3,3)=  1.694E-12 -4.071E-13 -4.071E-
13 -4.071E-13  1.694E-12 -4.071E-13 -4.071E-13
-4.071E-13  5.230E-12
 ASmatSym(3,3)=  6.963E+11  2.210E+11
2.210E+11  2.210E+11  5.615E+11  1.648E+11
2.210E+11  1.648E+11  5.615E+11
 MSmatSym(3,3)=  1.780E-12 -5.418E-13 -5.418E-
13 -5.418E-13  2.114E-12 -4.071E-13 -5.418E-13
-4.071E-13  2.114E-12
End Damage Dependent Quantities
```

1 cm (cgs units)

Figure B-18. Calculated quantities for Sammis micromechanical damage model for four values of the initial crack size acrack.

Matprops: nsammis_matprop= 1 K= 3.790E+11 G= 2.380E+11 rho= 2.600E+00 E= 5.904E+11 pois= 2.404E-01 lambda= 2.203E+11 vp= 5.175E+05 vs= 3.026E+05 vr= 2.723E+05 vm= 1.000E+05 K1C= 1.000E+08 acrack= 1.000E+01 fric= 6.000E-01 D0= 1.000E-01 phi= 5.152E-01 alpha= 8.702E-01 Nv= 3.623E-05 beta= 4.500E-01 shapefac= 2.000E+00 (Not used) End Matprops Damage Dependent Quantities D= 1.000E-01 c1= 3.356E-01 c2= 1.000E+00 c3= 0.000E+00 A1= 6.889E-01 A3= 2.149E+00 A_Sammis=-2.312E-01 B_Sammis= 7.213E-01 E_Sammis= 1.053E+00 A1S= 1.051E+00 A1Ssym= 0.000E+00 A2S=-3.199E-01 A3S= 1.248E+00 A4S= 2.088E+01 ASmat(3,3)= 6.963E+11 2.205E+11 2.209E+11 2.205E+11 6.889E+11 1.892E+11 2.209E+11 1.892E+11 5.661E+11 MSmat(3,3)= 1.737E-12 -4.071E-13 -5.418E-13 -4.071E-13 1.694E-12 -4.071E-13 -5.418E-13 -4.071E-13 2.114E-12 ASmatT(3,3)= 6.293E+11 1.533E+11 8.598E+09 1.533E+11 6.293E+11 8.598E+09 8.598E+09 8.598E+09 2.717E+10 MSmatT(3,3)= 1.694E-12 -4.071E-13 -4.071E-13 -4.071E-13 1.694E-12 -4.071E-13 -4.071E-13 -4.071E-13 3.706E-11 ASmatSym(3,3)= 6.963E+11 2.210E+11 2.210E+11 2.210E+11 5.615E+11 1.648E+11 2.210E+11 1.648E+11 5.615E+11 MSmatSym(3,3)= 1.780E-12 -5.418E-13 -5.418E-13 -5.418E-13 2.114E-12 -4.071E-13 -5.418E-13 -4.071E-13 2.114E-12 End Damage Dependent Quantities	Matprops: nsammis_matprop= 1 K= 3.790E+11 G= 2.380E+11 rho= 2.600E+00 E= 5.904E+11 pois= 2.404E-01 lambda= 2.203E+11 vp= 5.175E+05 vs= 3.026E+05 vr= 2.723E+05 vm= 1.000E+05 K1C= 1.000E+08 acrack= 1.000E+02 fric= 6.000E-01 D0= 1.000E-01 phi= 5.152E-01 alpha= 8.702E-01 Nv= 3.623E-08 beta= 4.500E-01 shapefac= 2.000E+00 (Not used) End Matprops Damage Dependent Quantities D= 1.000E-01 c1= 3.356E-01 c2= 1.000E+00 c3= 0.000E+00 A1= 6.889E-01 A3= 2.149E+00 A_Sammis=-2.312E-01 B_Sammis= 7.213E-01 E_Sammis= 1.053E+00 A1S= 1.051E+00 A1Ssym= 0.000E+00 A2S=-3.199E-01 A3S= 1.248E+00 A4S= 2.088E+02 ASmat(3,3)= 6.963E+11 2.205E+11 2.209E+11 2.205E+11 6.889E+11 1.892E+11 2.209E+11 1.892E+11 5.661E+11 MSmat(3,3)= 1.737E-12 -4.071E-13 -5.418E-13 -4.071E-13 1.694E-12 -4.071E-13 -5.418E-13 -4.071E-13 2.114E-12 ASmatT(3,3)= 6.269E+11 1.509E+11 8.911E+08 1.509E+11 6.269E+11 8.911E+08 8.911E+08 8.911E+08 2.816E+09 MSmatT(3,3)= 1.694E-12 -4.071E-13 -4.071E-13 -4.071E-13 1.694E-12 -4.071E-13 -4.071E-13 -4.071E-13 3.553E-10 ASmatSym(3,3)= 6.963E+11 2.210E+11 2.210E+11 2.210E+11 5.615E+11 1.648E+11 2.210E+11 1.648E+11 5.615E+11 MSmatSym(3,3)= 1.780E-12 -5.418E-13 -5.418E-13 -5.418E-13 2.114E-12 -4.071E-13 -5.418E-13 -4.071E-13 2.114E-12 End Damage Dependent Quantities
10 cm (cgs units)	1 m (cgs units)

Figure B-18 (continued). Calculated quantities for Sammis micromechanical damage model for four values of the initial crack size acrack.

LIST OF SYMBOLS, ABBREVIATIONS, AND ACRONYMS

AFRL	Air Force Research Laboratory
NTS	Nevada Test Site
USC	University of Southern California

DISTRIBUTION LIST

DTIC/OCP
8725 John J. Kingman Rd, Suite 0944
Ft Belvoir, VA 22060-6218 1 cy

AFRL/RVIL
Kirtland AFB, NM 87117-5776 1 cy

Official Record Copy
AFRL/RVB/2d Lt Simone M. Smith 1 cy